Atomic layer deposited tin oxide as an electron transport layer for perovskite solar cells

van Gils, Roderick J.

Award date:
2017

Atomic Layer Deposited Tin Oxide as an Electron Transport Layer for Perovskite Solar Cells

Master of Science Thesis

Roderick van Gils

November 2017

Eindhoven University of Technology

Atomic Layer Deposited Tin Oxide as an Electron Transport Layer for Perovskite Solar Cells

Master of Science Thesis

R.J. van Gils, BSc

06 November 2017

PMP 17-19

Supervisors:

Dr. Y. Kuang
Dr. M. Creatore

Graduation committee:

Dr.ir. J. Beckers
Prof.dr.ir. P.P.A.M. van der Schoot
Dr.ir. A.M. de Jong
Dr. M. Creatore

Eindhoven University of Technology
Department of Applied Physics
Plasma & Materials Processing Group

Abstract

Over the past eight years, perovskite solar cells (PSCs) have emerged as an impressive photovoltaic technology, due to their astonishing efficiency development from 3.8% to 22.1%. Nonetheless, their environmental instability against air and humidity has remained a key concern. Recently, this concern has been addressed by adopting metal oxides as protective barrier layers, which can also serve as an electron transport layer (ETL). Hitherto, titanium dioxide has been frequently applied as such an ETL, although it could deteriorate under UV-light exposure and it may have an unfavorable energy band alignment with the perovskite. Consequently, tin oxide (SnO_2) has been proposed in literature as an alternative ETL material. However, a systematic research on SnO_2 applied in PSCs still lacks. Therefore, the correlation between SnO_2 material properties, SnO_2/perovskite interfacial properties, and the PSC performance has been investigated in this work.

To deliver high quality SnO_2 layers, plasma enhanced atomic layer deposition (PE-ALD) has been applied. An ALD recipe has been developed, whereby deposition temperatures have been varied between 50°C and 200°C in order to induce diverse material properties. Next, these material properties have been thoroughly characterized. At 50°C, amorphous SnO_2 layers with a relatively low mass density (4.10 g/cm^3) have been deposited, containing significant carbon and nitrogen impurities and hydroxyl groups. Additionally, these layers exhibited a large electrical resistivity and a wide optical band gap (4.25 eV). For an increasing deposition temperature, the material retained its amorphous phase with reduced impurity fractions and an increased mass density. Concurrently, the electrical resistivity and the optical band gap decreased. At a deposition temperature of 200°C, SnO_2 layers of high purity have been synthesized, containing nano-crystallites in an amorphous matrix with a high mass density (6.10 g/cm^3). These SnO_2 layers showed to be degenerate with a low electrical resistivity ($(1.8 - 2.1) \cdot 10^{-3}$ Ω·cm), and an optical band gap of 3.25 eV.

Then, SnO_2 layers have been applied as an ETL in planar PSCs, and their performances have been characterized. High efficiencies of 17.5% and 17.8% have been achieved for PSCs containing SnO_2 deposited at 50°C and 200°C, respectively, though both with a considerable J-V hysteresis. The PSCs with SnO_2 deposited at 200°C have demonstrated a higher fill factor and a higher short-circuit current, presumably due to a relatively better electron extraction given the higher SnO_2 electrical conductivity. Moreover, the PSCs containing SnO_2 deposited at 200°C have largely maintained their high initial efficiencies even after 16 hours of continuous AM1.5G illumination, with a bias voltage holding at the maximum power point.

Contents

List of Abbreviations **vii**

1 Introduction **1**
1.1 Perovskite Solar Cells 1
1.2 Tin Oxide as an Electron Transport Layer 3
1.3 Research Questions 3
1.4 Thesis Outline 4

2 Perovskite Solar Cells: Principles, Challenges, and Potential Solutions **5**
2.1 The Introduction of Perovskite Solar Cells 5
2.1.1 First Application of Perovskite in Solar Cells 5
2.1.2 Challenges for Perovskite Solar Cells 7
2.2 Solutions to Address Perovskite Solar Cell Challenges 8
2.2.1 Planar Instead of Mesoscopic Cell Configuration 8
2.2.2 Substitution of Perovskite Constituents 8
2.2.3 Inorganic Charge Transport Layers 9
2.3 Inorganic Electron Transport Layers for Perovskite Solar Cells 10
2.3.1 Electron Transport Layers: Requirements and Examples 10
2.3.2 Atomic Layer Deposited SnO_2 as an Electron Transport Layer . . . 12
2.4 Summary 12

3 Experimental Details on Characterization Methods and Fabrication of Perovskite Solar Cells **13**
3.1 Compositional Characterization Techniques 13
3.1.1 X-ray Photoelectron Spectroscopy 13
3.1.2 Rutherford Backscattering Spectrometry & Elastic Recoil Detection 14
3.2 Structural and Morphological Characterization Techniques 16
3.2.1 X-ray Diffraction 16
3.2.2 Transmission Electron Microscopy 17
3.2.3 Scanning Electron Microscopy 17
3.3 Electrical Characterization Techniques 18
3.3.1 Hall Effect 18
3.4 Optical and Energy Level Characterization Techniques 19
3.4.1 Spectroscopic Ellipsometry 19
3.4.2 Ultraviolet-Visible-Near Infrared Spectroscopy 20
3.4.3 Ultraviolet Photoelectron Spectroscopy 20
3.5 Electrochemical Impedance Spectroscopy 20
3.5.1 Theoretical Background 21
3.5.2 Electrochemical Impedance Spectroscopy Measurement 23

3.5.3 Electrochemical Impedance Spectroscopy Data Processing 25
3.5.4 Summary 28
3.6 Fabrication and Characterization of Perovskite Solar Cells 28
3.6.1 Fabrication of Perovskite Solar Cells 28
3.6.2 Characterization of Perovskite Solar Cells 30

4 Atomic Layer Deposition of Tin Oxide 33
4.1 Set-up, Proceedings and Materials 33
4.1.1 ALD Reactor and General Procedure 33
4.1.2 Choice of Precursor and Co-reactant 34
4.2 Development of ALD Recipe 35
4.3 Growth of SnO_2 at Different Temperatures 38
4.4 Summary 38

5 Material Characterizations of Atomic Layer Deposited Tin Oxide 39
5.1 Chemical Composition Characterization 39
5.2 Structural and Morphological Characterization 42
5.3 Electrical Characterization 44
5.4 Optical and Energy Level Characterization 44
5.4.1 Optical Characterization 44
5.4.2 Energy Level Characterization 45
5.5 Electrochemical Impedance Spectroscopy Characterizations 47
5.5.1 Results & Discussion on SnO_2 Deposited at 200°C 47
5.5.2 Results & Discussion on SnO_2 Deposited at 50°C 49
5.6 Summary 55

6 Optoelectronic Performance and Interface Characterizations of Perovskite Solar Cells 57
6.1 Fabrication and Performance Characterization of Perovskite Solar Cells . . 57
6.2 Bulk and Interface Characterizations on Perovskite Solar Cells 60
6.2.1 Energy Level Structure via Ultraviolet Photoelectron Spectroscopy . 61
6.2.2 Electron Extraction Properties via Photoluminescence Spectroscopy 62
6.3 Literature Comparison on Perovskite Solar Cell Performances 64
6.4 Summary 65

7 Conclusions and Recommendations 67
7.1 Conclusions 67
7.2 Recommendations 68

Acknowledgements 71

Appendix A Basics of Atomic Layer Deposition 73
A.1 Introduction 73
A.2 Working Principle 73
A.3 Recipe Development 74
A.4 Application of Plasma 74

Appendix B Additional Figures Material Characterizations of Atomic Layer Deposited Tin Oxide 77

Appendix C Validation of Electrochemical Impedance Spectroscopy Measurements **79**

Appendix D Practical Issue of Manufacturing Perovskite Solar Cells **81**

Appendix E Additional Figures Optoelectronic Performance and Interface Characterizations of Perovskite Solar Cells **83**

References **83**

List of Abbreviations

ALD	atomic layer deposition
AM1.5G	*see footnote 9 at page 30*
CB	conduction band
CPE	constant phase element
c-Si	crystalline silicon
CTL	charge transport layer
DSSC	dye-sensitized solar cell
EIS	electrochemical impedance spectroscopy
ERD	elastic recoil detection
ETL	electron transport layer
FA	formamidinium
FF	fill factor
FTO	fluorine doped tin oxide
GI-XRD	grazing incidence diffraction
GPC	growth per cycle
HAADF-STEM	high angle angular dark field scanning transmission electron microscopy
HTL	hole transport layer
IP	ionization potential
ITO	tin doped indium oxide
J_{SC}	short-circuit current density
J-V	current density - voltage
MA	methylammonium
$MAPbI_3$	methylammonium lead triiodide
MPP	maximum power point
n-i-p	n-type - intrinsic - p-type
PCE	power conversion efficiency
PE-ALD	plasma-enhanced atomic layer deposition
p-i-n	p-type - intrinsic - p-type
PL	photoluminescence spectroscopy
PL-SS	photoluminescence spectroscopy steady-state
PL-TR	photoluminescence spectroscopy time-resolved
PSC	perovskite solar cell
RBS	rutherford backscattering spectrometry
RF	radio frequency
SAM	self-assembled monolayer
SE	spectroscopic ellipsometry
SEM	scanning electron microscopy
SnO_2	tin oxide
TCO	transparent conductive oxide
TEM	transmission electron microscopy
TiO_2	titanium dioxide
UPS	ultraviolet photoelectron spectroscopy
UV-VIS-NIR	ultraviolet-visible-near infrared spectroscopy
VB	valence band
VBM	valence band maximum
V_{OC}	open-circuit voltage
WF	work function
XPS	x-ray photoelectron spectroscopy
XRD	x-ray diffraction

Chapter 1

Introduction

Over the last decades, global energy consumption has been continuously expanding, which has been mainly facilitated by energy generation from burning fossil fuels. Since burning these fossil fuels yields environmentally undesirable reaction products and their sources are exhaustible, the implementation of sustainable energy technologies is indispensable.

Solar cells have created an attractive solution to this demand, because they can be employed relatively conveniently as both stationary and portable electricity sources, and solar energy is abundantly available worldwide. Currently, crystalline silicon (c-Si) is the most applied photo-absorbing semiconductor in solar cells, since it is affordable and scalable, and it provides a reasonable photovoltaic efficiency. However, c-Si solar cells are, for instance, not flexible and less efficient indoors [1]. Therefore, a continuous quest for inexpensive and still more efficient solar cells is valuable, absolutely if they even address such aforementioned inconveniences.

1.1 Perovskite Solar Cells

Perovskite solar cells (PSCs) are impressive competitors in the photovoltaic research field, since they are inexpensive due to their widely available raw materials and simple low-temperature processing [2, 3]. Partly due to the latter, also flexible devices have been successfully fabricated [4, 5]. Moreover, their record efficiency climbed from an initial 3.8% in 2009 [6] to 22.1% in 2017 [7]: a very promising increase compared to other solar cell technologies, as demonstrated in Figure 1.1.

Definitely, these exceptional results originate from diverse improvements in this solar cell's configuration, of which a general schematic is given in Figure 1.2. Incident light enters the cell from the glass side, then passes two highly transparent layers, and finally reaches the photo-absorbing perovskite crystal. Traditionally, this perovskite consists of methylammonium lead triiodide ($CH_3NH_3PbI_3$ or $MAPbI_3$). Over there, photons with high enough energies can excite electrons from the valence to the conduction band, by which electron-hole pairs are generated. These free charge carriers can move towards the adjacent selective transport layers, at which ideally only holes or only electrons are allowed to pass towards the metal contact or the transparent conductive layer, respectively. Consequently, positive and negative charge carriers are successfully separated and collected. Thereby, an electric potential difference is formed between the top and the bottom of the cell, which induces an electric current between them if an external circuit is established. Eventually, the transmitted electrons recombine with holes in the metal contact.

The earlier mentioned exceptional results, such as the high efficiencies, can be obtained, for instance, either by adjusting properties of the applied materials, or by (partially)

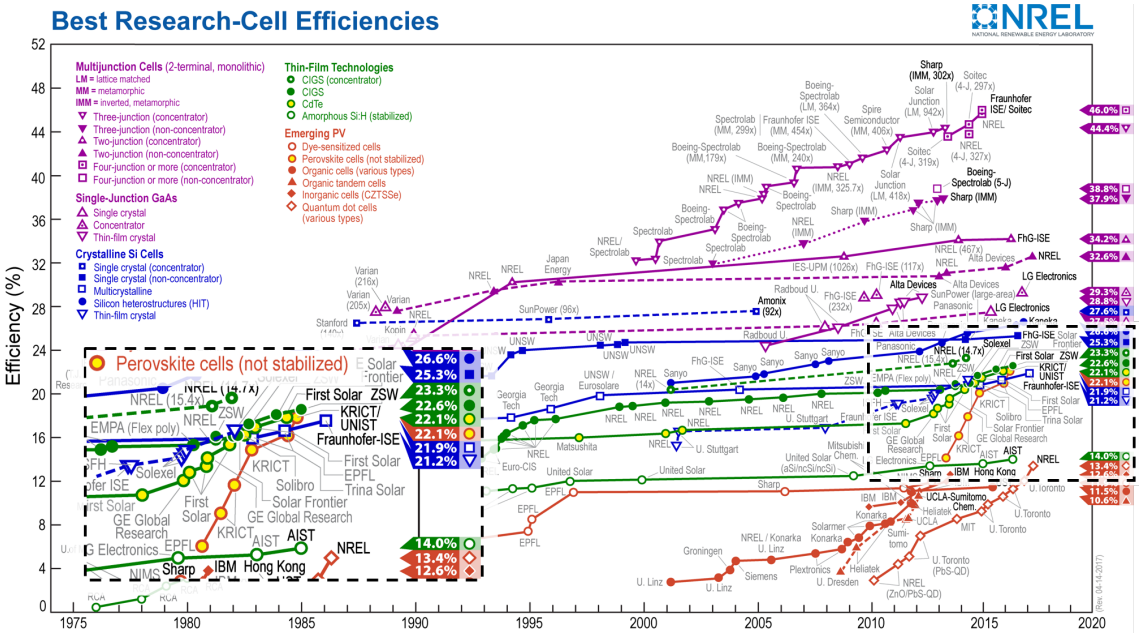

Figure 1.1: *Overview of the highest achieved photovoltaic efficiencies for all solar cell technologies from 1976 until 2017, with a zoomed-in view to emphasize the perovskite solar cell progress. Adapted from [8].*

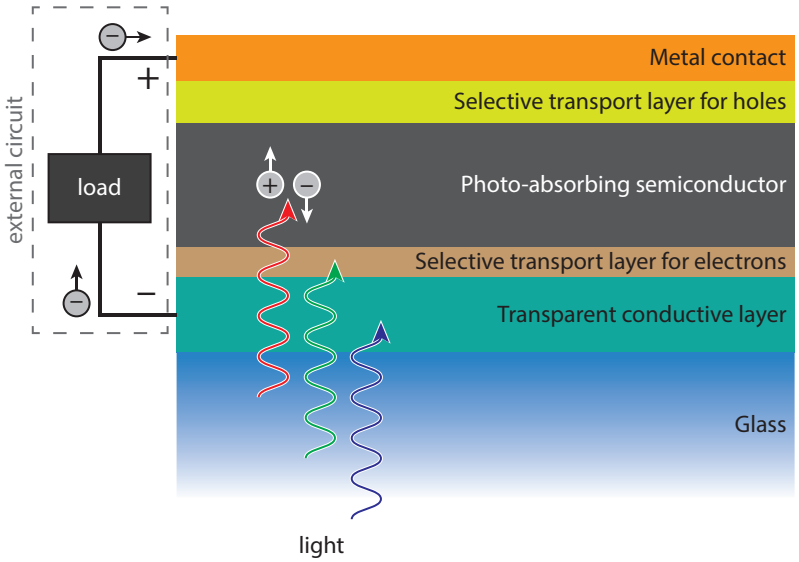

Figure 1.2: *Schematic configuration of a planar perovskite solar cell in an n-i-p configuration. The light absorbing layer is encapsulated between two selective transport layers, and together they are again enclosed between two conductive contacts. These contacts are connected to each other via an external circuit, in order to induce an electric current.*

introducing other materials [9, 10]. However, increasing the efficiency is only one of the topics in PSC research, since the environmental stability of the perovskite itself is a critical concern. For instance, upon exposure to oxygen, humidity, ultraviolet radiation and/or high temperatures, the perovskite $MAPbI_3$ can easily deteriorate within a few minutes until a few days [11–16]. This challenge has been addressed by changing the constituents

of the perovskite crystal itself [10,16–19], and also by incorporating protective barrier layers adjacent to the perovskite. For the latter solution, especially metal oxides have shown to be suitable candidates [16,20,21], since they generally have a high environmental stability themselves [11, 20, 21]. Moreover, given their (tunable) electronical properties, they can simultaneously be applied as either an electron or a hole transport layer [11, 16].

1.2 Tin Oxide as an Electron Transport Layer

Usually, titanium dioxide (TiO_2) is applied as such an inorganic electron transport layer (ETL) in PSCs. Nevertheless, it has been shown that the application of TiO_2 can provide unstabilized efficiencies, possibly due to an unfavorable conduction band edge alignment between the TiO_2 and the perovskite [22]. Hereby, electrons should overcome an energy barrier before they can be extracted, which would induce the accumulation of electrons at the TiO_2/perovskite interface. This could result in undesired capacitive effects, by which the overall PSC performance would be affected [22].

Consequently, Correa Baena *et al.* proposed to apply tin oxide (SnO_2) as an ETL, since its conduction band minimum is generally positioned deeper. This should prevent the energy barrier and thus facilitate a better energy band alignment with the perovskite. Eventually, in their case this led to a stable, higher photovoltaic efficiency [22]. However, other research groups have found that there may be more requirements to achieve high, stabilized performances, via an efficient electron extraction from the perovskite [23–25]. Nevertheless, among these investigations a systematic research into the correlation between the SnO_2 material properties, the SnO_2/perovskite interfacial properties, and the PSC performance still lacks. Therefore, in this research it has been investigated how the properties of the developed SnO_2 layers affect the eventual performances of PSCs. In this regard, various film and interfacial properties have been studied to assemble in-depth understanding of the fundamental mechanisms.

To deposit thin layers of SnO_2, plasma enhanced atomic layer deposition (PE-ALD) has been explored, since compared to other deposition principles (e.g., spin coating, sol-gel, sputtering) it enables the fabrication of ultrathin and uniform films with a high quality [21, 26–29]. In particular, this high quality is exhibited by the minimal occurrence of pinholes, through which a closed layer can be ensured [22, 26, 30, 31]. Moreover, the PMP research group has recently addressed the potential of this deposition technique for PSCs in a perspective paper [21].

1.3 Research Questions

As described before, this research has focused on the material properties of atomic layer deposited SnO_2, and their influence on the performance of PSCs incorporating them as an ETL. Specifically, a variation in SnO_2 material properties has been introduced by varying the deposition temperature of the substrate during the ALD process between 50°C and 200°C. Therefore, the first research question is:

1. *How are the material properties of atomic layer deposited tin oxide layers affected by the deposition temperature?*

Among the analytical tools employed to characterize these SnO_2 layers, this research work has focused on electrochemical impedance spectroscopy (EIS), relatively new to the field of ultrathin (< 100 nm) film deposition. Accordingly, the second research question is:

2. *What insights into atomic layer deposited tin oxide properties can be obtained by means of electrochemical impedance spectroscopy?*

Finally, the ALD SnO_2 layers deposited at different temperatures have been integrated as an ETL in PSCs, and their performances and SnO_2/perovskite interfacial properties have been evaluated. Correspondingly, the third research question is:

3. *How do the material and interfacial properties of tin oxide affect the performance of perovskite solar cells?*

In the next section, it is elaborated how this thesis has been structured in order to fulfill these research questions.

1.4 Thesis Outline

First, Chapter 2 delivers an introduction to the PSC and the challenges that this technology currently faces. Furthermore, it describes which solutions have already been incorporated in our PSCs to address these challenges, and it provides a special focus on the supposed requirements for an ETL. Lastly, it gives a research overview on the application of ALD SnO_2 in PSCs. Next, the material characterization techniques applied on the SnO_2 layers are addressed in Chapter 3, including an extended elaboration on EIS. Furthermore, the fabrication procedure of PSCs is presented, followed by a description of the applied techniques for the PSC characterization. Subsequently in Chapter 4, the ALD process to synthesize our SnO_2 layers is described. For the reader who is not familiar with ALD, a general description about the principles of this deposition technique is provided in Appendix A. Then, the results of the characterizations performed on different SnO_2 layers are discussed in Chapter 5. Having identified these SnO_2 material properties, the performances of PSCs with SnO_2 ETLs are shown in Chapter 6. Additionally, results of interface characterizations are presented and discussed, in order to understand how the ALD SnO_2 layers affect the PSC performances. Eventually, in Chapter 7 the overall conclusions of this research are provided, together with some recommendations for future research.

Chapter 2

Perovskite Solar Cells: Principles, Challenges, and Potential Solutions

Before proceeding to the details and results of this research, first a general overview is given on what perovskite actually is, how it has been applied in solar cells, and what challenges these cells still encounter. Then, a short overview on solutions from the literature to these challenges is given, including the application of inorganic electron transport layers. Eventually, an overview is provided on the requirements for these electron transport layers, together with a current research status on the application of tin oxide as an electron transport layer for perovskite solar cells.

2.1 The Introduction of Perovskite Solar Cells

In 1839, the German Gustav Rose discovered the mineral calcium titanium oxide ($CaTiO_3$) in the Ural Mountains of Russia. The mineral received the alias "perovskite", named after the Russian mineralogist Lev Alekseevich Perovski [32]. However, since its crystal structure is adopted by many more (functional) materials, "perovskite" has become an umbrella term for all these materials, together distributing an extensive variety of special properties, such as piezoelectricity, superconductivity, and semiconductivity [33].

A representative perovskite crystal structure is schematically presented in Figure 2.1, and it can be simply described by the general chemical formula ABX_3. In this formula, A and B are cations of different dimensions and X is an anion. The crystal structure is dependent on the specific composition and the temperature, varying between cubic, tetragonal, and orthorhombic [17].

2.1.1 First Application of Perovskite in Solar Cells

For photovoltaic purposes, organometallic halide perovskites are prevalent, with methylammonium lead triiodide ($MAPbI_3$) as the best known photo-absorber. It possesses $CH_3NH_3^+$ (MA) as larger cation A, Pb^{2+} as smaller cation B, and I^- as anion X. Together these ions adopt a tetragonal crystal structure at room temperature [17]. The excellent optoelectronic properties make this perovskite material very interesting: it shows adequate ambipolar charge transport, partly due to relatively large, balanced electron and hole mobilities and high carrier diffusion lengths [2, 17, 33]. Further on, it possesses a high light absorption coefficient with a steep absorption edge, similar to other well-performing

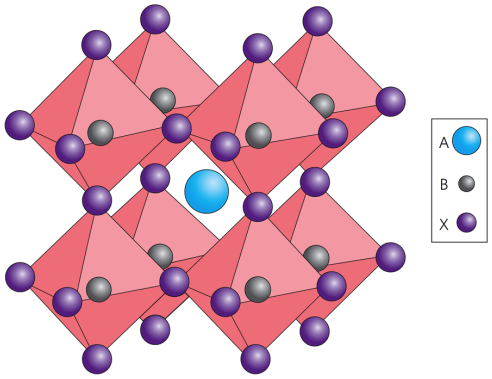

Figure 2.1: *Schematic presentation of the general perovskite crystal structure with A and B as cations and X as anion. For photovoltaic purposes, the best known species for A, B and X are $CH_3NH_3^+$, Pb^{2+} and I^-, respectively. Adapted from [13].*

photovoltaic materials [2, 34]. In addition, it exhibits low exciton binding energies, such that holes and electrons can be easily separated [17]. Consecutively, its fundamental energy losses are low compared to many other light absorbing materials for photovoltaic applications [33].

Kojima *et al.* (2009) were the first to report about the application of this material in solar cells, inspired by the configuration of dye-sensitized solar cells (DSSCs) [6]. In these DSSCs, a so-called "mesoscopically structured" electron transport layer (ETL) is covered by a sparse layer of organic dye (the sensitizer), which functions as the photo-absorbing material. Since this layer is very thin ($\sim 2\mu$m) and organic sensitizers have low absorption coefficients and low absorption bands, the main aim for a sensitizer substitution was to increase the harvesting of light. Inspired by the "unique optical properties, excitonic properties, and electrical conductivity" [6], $MAPbI_3$ was chosen to replace the conventional photo-absorbing organic sensitizers. Consequently, the amount of photo-excitation should increase due to a stronger light absorption over a broader spectrum [33]. See Figure 2.2a for a schematic configuration of the device of Kojima *et al.*, in which the mesoscopically structured ETL is covered by the perovskite (instead of by an organic dye).

Even though the performance of this perovskite solar cell (PSC) obtained in this pioneering work (3.8%) was not too competitive compared with other more established solar cell technologies (see Figure 1.1), it opened a new platform for solar cell design and initiated a search for improvements. For instance, a first approach consisted of replacing the undesirable liquid electrolyte since it caused the perovskite to decompose or dissolve, degrading the solar cell already within a few minutes [33]. A solution was provided by Kim *et al.* (2012) through the application of a solid-state organic hole transport layer (HTL) on top of the perovskite [35]: see Figure 2.2b. With spiro-OMeTAD[1] as a HTL, they improved the solar cell stability extremely: after 500 h storage in air at room temperature (without encapsulation), it still performed well. Moreover, this innovation even raised the power conversion energy (PCE) to 9.7%, which by then already exceeded the highest efficiency value reported for DSSCs [33].

This substitution is only one example out of a huge variety of novelties published in the PSC field since 2009. Namely, many researchers have attempted to discover solutions for the critical challenges PSCs encounter. In the next section, the most important challenges amongst them are presented.

[1]Spiro-OMeTAD: 2,2',7,7'-tetrakis-(N,N-di-p-methoxyphenylamine)-9,9'-spirobifluorene.

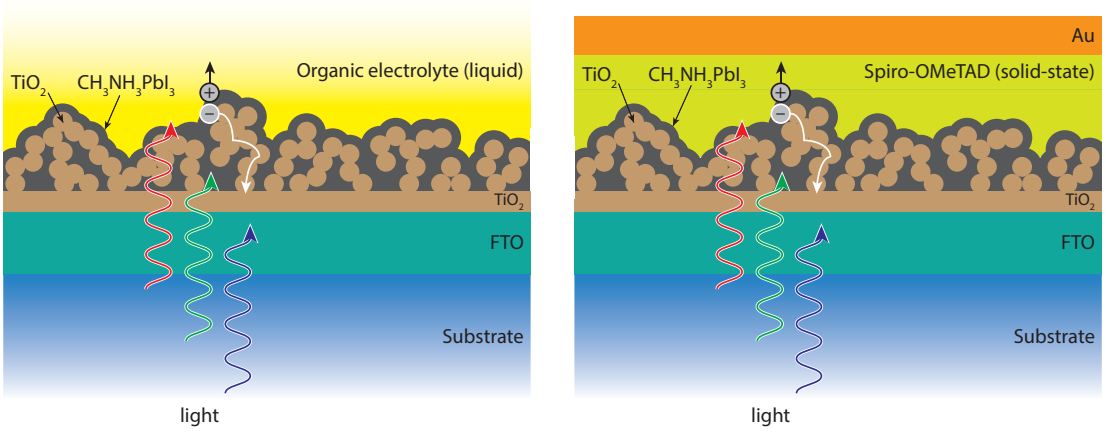

Figure 2.2: *Schematic configurations of perovskite solar cells by (a) Kojima et al. (2009) [6] and by (b) Kim et al. (2012) [35]. Light is converted into free charge carriers in the perovskite. Electrons can diffuse towards and through the mesoscopic titanium dioxide (TiO_2) scaffolds towards the fluorine doped tin oxide (FTO). On the other hand, holes can diffuse (a) towards and through a liquid, organic electrolyte and be collected by an electrode, or (b) towards and through a solid-state hole transport layer and be collected at the gold electrode (Au).*

2.1.2 Challenges for Perovskite Solar Cells

Hitherto, there have been four main challenges for PSCs, of which one - or simultaneously more - can be addressed by every novel change in either PSC design or material choice [21]:

- **Increase environmental stability:** upon exposure to humid air [11, 12], UV-light [13] and high temperatures [14, 15], perovskite can degrade easily within a few minutes until a few days [16]. This instability greatly impedes a realistic implementation of PSCs. On the contrary, currently conventional photovoltaic devices based on crystalline silicon persevere for 20 - 25 years. Therefore, it is probable that a longer PSC lifetime will be required by the photovoltaic market [2, 33].
- **Reduce hysteresis in J-V behavior:** for not yet completely explicable reason(s), the current density-voltage (J-V) behavior of PSCs can be dependent on the scanning rate and direction of the performance related J-V measurement. See Figure 2.3 for an example of hysteresis for different scanning directions. Proposed possible explanations for such hysteresis are, among other things [17, 20, 36]: the filling of interface/surface trap states with charge carriers [12], ionic migration [37–39], imbalanced charge extraction [25], and accumulation of charges at grain boundaries [40]. Regardless, the hysteresis leads to diminished and unreproducible (long-term) PSC performances [13, 25, 41].
- **Increase efficiency and achieve scalability:** PSCs of 0.095 cm^2 with a PCE of above 22% have already been reported [7, 8], but still it is hard to reach such high PCEs for PSCs that deal fairly with the other challenges mentioned above. Furthermore, most of the PSCs reported in literature have areas of only a few mm^2 [21]; devices on the cm^2 scale have been sparsely reported, with generally lower PCEs [4, 7]. In conclusion, the combination of high efficiency, long-term stability, and large-area fabrication will be required for the commercialization of PSCs.

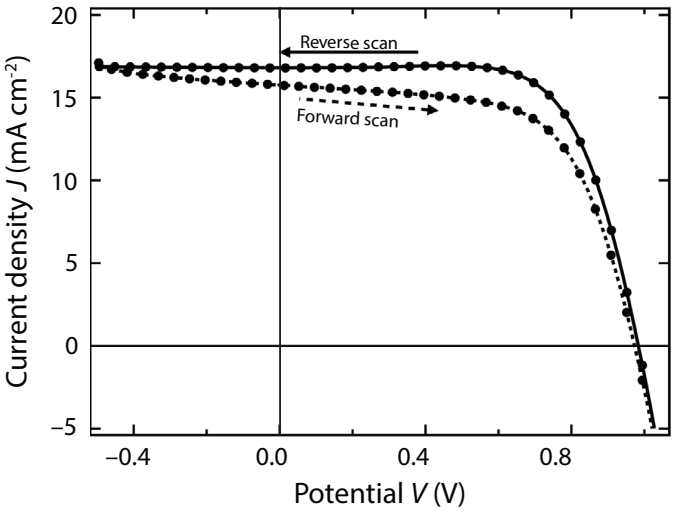

Figure 2.3: *Example of J-V hysteresis for forward and reverse voltage scanning directions. Adapted from [38].*

In the subsequent sections, a few solutions for above-mentioned challenges are discussed. The solutions shown here substantiate the basis of our PSC design and its constituents.

2.2 Solutions to Address Perovskite Solar Cell Challenges

2.2.1 Planar Instead of Mesoscopic Cell Configuration

As one could have noticed already, the configurations displayed in Figure 2.2b and 1.2 are different from each other. The structure displayed in Figure 2.2b originates from the DSSC configuration in which the perovskite solely serves as a photo-absorber, since it directly passes charge carriers to the HTL and TiO_2 scaffolds. However, perovskite can be composed such that it has high diffusion lengths for both holes and electrons [42, 43]. Combined with its good charge carrier mobilities that are comparable with other thin film absorbers [17], this allows the perovskite to be an ambipolar charge transport layer too, rather than only a photo-absorbing layer [33]. Consequently, the TiO_2 scaffold becomes redundant, since the only task left for TiO_2 is to select electrons and block holes. This can be performed by an ETL substrate layer only and therefore, the planar structure as presented in Figure 1.2 can be applied.

Apart from the easier synthesis of the planar configuration compared to the mesoscopic configuration [2, 25], the planar configuration has the benefit that the HTL and the ETL can be definitely separated. In the mesoscopic configuration, performance reducing back charge transfer could still occur via shunts, caused by direct mutual contact between the HTL and the ETL after a non-uniform deposition of perovskite [13]. However, despite the fact that this problem can be avoided, so far the best performing mesoscopic structured PSCs have still obtained slightly higher PCEs than the best performing planar structured PSCs.

2.2.2 Substitution of Perovskite Constituents

As already mentioned in the introduction, the substitution of perovskite constituents can improve the PSC performance in terms of efficiency and stability. For instance, the (partial) substitution of I^- by Br^- can provide a larger band gap and thus a higher open-circuit

voltage (V_{OC}) [2,10,44], resulting in a higher PCE [45,46]. Further on, this (partial) substitution can also enhance the stability against humidity [17]. Beside an anion substitution, cation substitutions have also been implemented: next to methylammonium, cations formamidinium (FA, $CH_3(NH_2)_2^+$) and cesium (Cs^+) can (partially) replace the large cation A. By mixing the FA with MA, longer charge carrier lifetimes have been achieved compared to pure $MAPbI_3$ [10, 18], leading to less chance for charge recombination. Furthermore, the incorporation of cesium in the last-mentioned mixture of FA and MA has provided higher PCEs and a higher stability against humid air [19, 45, 47].

2.2.3 Inorganic Charge Transport Layers

Traditionally, organic charge transport layers (CTLs) have been applied in DSSCs, after which they have been proposed too for PSCs. Examples are spiro-OMeTAD[1] and PEDOT:PSS[2] as HTLs, and PCBM[3] as an ETL. Both types generally contribute to high PCEs and reduce or even eliminate J-V hysteresis [9,37]. However, organic CTLs can be detrimental for the stability of PSCs, since either they themselves can degrade due to the factors mentioned in Section 2.1.2, or they may fail in protecting the sensitive perovskite from them [11]. For instance, spiro-OMeTAD can have pinholes through which water and oxygen may reach the perovskite, and degradation products such as MAI and HI could leave the perovskite [16]. Further on, PEDOT:PSS can damage the adjacent transparent conductive oxide (TCO) and trigger $MAPbI_3$ breakdown [16]. A latter example is given by PCBM, which can absorb oxygen and water, whereby it may degrade itself and the perovskite in contact [16].

In contrast, metal oxides (such as TiO_2 and SnO_2) as inorganic CTLs are generally much more chemically stable against, for instance, water, oxygen and heat [11, 20, 21]. In addition, they can be designed to establish a barrier layer in order to prevent diffusion of species into or out of the perovskite [16, 20, 21], and they themselves seem to keep the perovskite intact [11]. Moreover, these inorganic CTLs are in general inexpensive compared to organic CTLs [11,16]. This makes them interesting for industrial application, definitely given their large variety of easily upscalable deposition principles [21]. However, they also have a noticeable disadvantage: PSCs with inorganic CTLs often suffer from J-V hysteresis, and then need an extra CTL post-treatment or interlayer to avoid this hysteresis [11, 24, 48, 49].

Given the aforementioned advantages, metal oxides as inorganic CTLs have been considered as promising candidates to replace the organic CTLs and enhance the long-term environmental stability of PSCs. Hereby, they have recently triggered an extensive research interest in the PSC field. In this work, we particularly focus on SnO_2 as an inorganic ETL for perovskite solar cell applications.

[2]PEDOT:PSS: poly(3,4-ethylenedioxythiophene) polystyrene sulfonate.
[3]PCBM: [6,6]-phenyl-C_{61}-butyric acid methyl ester.

2.3 Inorganic Electron Transport Layers for Perovskite Solar Cells

2.3.1 Electron Transport Layers: Requirements and Examples

Currently, research into the requirements for inorganic ETLs is still predominantly exploratory and as a consequence, the assumed prerequisites are yet under debate. Though, some factors are generally believed to be significant for the good functioning of an ETL in a PSC [21]:

- **Electrical continuity in the lateral direction:** direct contact between the substrate metal or TCO with the perovskite should be prevented by the ETL. Otherwise, also holes can reach the metal or TCO via shunt channels formed by, for instance, pinholes. Then, charge selectivity is lost and holes can recombine with electrons, thereby diminishing the overall PSC performance.
- **Transparency for a broad light spectrum:** in order to reduce parasitic absorption by the ETL, it should be highly transparent (if applied in an n-i-p configuration). This can be achieved by ensuring that the ETL has a large optical band gap.
- **Alignment of energy levels:** beside the need to physically block holes as described in the first requirement, the ETL should also electronically block holes. This can be achieved via a deep ETL valence band (VB) with respect to the VB of the perovskite: see Figure 2.4. Furthermore, electron extraction can be enhanced as the ETL conduction band (CB) minimum aligns well with the perovskite CB minimum. Such a deep VB and a proper CB minimum alignment can be aimed for by choosing materials according to their energy levels. A small overview of the energy levels of a few commonly used (in)organic ETLs and perovskites has been given in Figure 2.5.

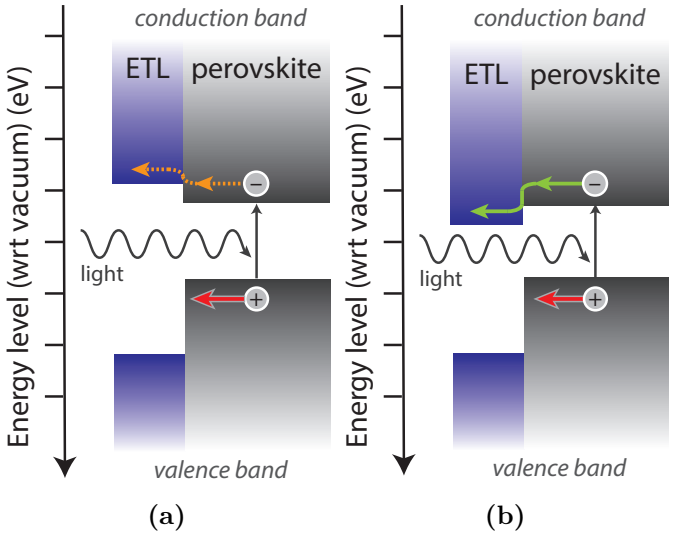

Figure 2.4: *Simplified energy band diagrams of the perovskite with adjacent ETL. In both cases (a, b), passage of holes towards the ETL is blocked by a deep ETL valence band (VB). Further on, (a) shows a more shallow ETL conduction band (CB) with respect to the perovskite CB. Hereby, electron extraction may be reduced due to an energy barrier. (b) presents a deeper ETL CB with respect to the perovskite CB. Thereby, the energy band alignment provides an unhindered electron extraction.*

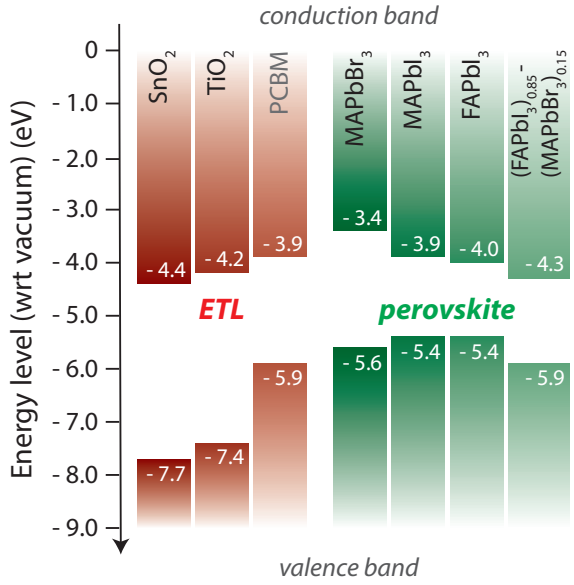

Figure 2.5: *Schematic presentation of typical CB and VB energy levels of mentioned (in)organic ETLs, in comparison with the energy levels of the most used perovskite compositions. Values are all with respect to vacuum, and have been taken from [21, 22].*

Conventionally, TiO_2 has been applied as an ETL in PSCs as it was transferred from the DSSC architecture [6]. As already shown in Figure 2.5, TiO_2 has a wide band gap and is thus transparent for visible light. Furthermore, it possesses a deep enough VB to block holes, and dependent on the perovskite mixture it can have a good CB minimum alignment. Though, generally its electron mobility is quite low, which can increase the PSC series resistance and the possibility of recombination, since charges reside longer inside the PSC [50–52]. Both can lead to reduced PSC performances. Furthermore, the quality of TiO_2 may deteriorate under UV-light exposure due to photocatalytic activity, which makes long-term functioning uncertain [16, 49, 53].

An alternative inorganic ETL is SnO_2. It has advantages similar to those mentioned for TiO_2, and additionally it usually also has a higher electron mobility [51, 52, 54, 55]. This can be beneficial for a lower PSC series resistance. Furthermore, due to its different energy levels it could be a more suitable ETL in terms of band alignment with certain perovskite compositions [54].

Until here, only the lateral continuity requirement has been untreated. Generally, it can be addressed by adopting an appropriate deposition principle. Various principles are currently available, such as spin coating [54, 56], sol-gel [50, 57], spray pyrolysis [58, 59], and atomic layer deposition (ALD). Amongst them, ALD has shown to deliver ultrathin and dense metal oxide films with an unequalled uniformity and excellent conformality [21, 27–29]. These qualities can ensure a closed ETL, which can prevent ingress and/or egress of species into or from the perovskite layer [12, 15, 31, 59, 60]. Furthermore, often only a few nanometers of material are required for the functioning of an ETL [5, 21, 29, 61], which can be accurately achieved with ALD since the layer thickness can be controlled at the Ångström level [27, 28]. Hereby, the ETL minimally contributes to the total PSC series resistance [61].

2.3.2 Atomic Layer Deposited SnO_2 as an Electron Transport Layer

Hitherto, ALD SnO_2 layers have been applied in PSCs by a few research groups, which obtained fair *PCE*s between 15.3% and 20.3% [22–25]. Correa Baena *et al.* (2015) presented nearly J-V hysteresis-free PSCs with an efficiency over 18%, and attributed these performances to a good CB edge alignment between the SnO_2 and the perovskite ($(FAPbI_3)_{0.85}(MAPbBr_3)_{0.15}$). Hereby, they declared that capacitive effects due to charge accumulation at an interfacial energy barrier would have been prevented, enabling an efficient electron extraction [22]. Hu *et al.* (2017), however, did encounter electron extraction problems, which they ascribed to the spontaneous establishment of a PbI_2 layer at the SnO_2/perovskite interface. This would form an energy barrier either at the perovskite/PbI_2 or at the PbI_2/SnO_2 interface [23]. Furthermore, Wang *et al.* (2016) claimed that the addition of an intervening "C_{60}-SAM[4] interlayer" would be necessary to stimulate charge extraction at the SnO_2/perovskite interface, in order to deliver less J-V hysteresis [24]. In a later publication, Wang *et al.* (2017) demonstrated what physical principle would be behind this necessity: they proposed there was indeed an imbalanced charge transport between the electron transport at the SnO_2/perovskite and the hole transport at the spiro-OMeTAD/perovskite interfaces. They attributed this to the low conductivity of ALD SnO_2 deposited at 100°C, by which electron extraction at the SnO_2/perovskite interface would be inefficient [25].

In general, these investigations have focused on improving the initially insufficient electron extraction, in order to reduce J-V hysteresis and improve the overall PSC performance. However, among them there is no systematic study into PSCs with ALD SnO_2 layers that cover a large variety of material properties. For instance, the correlation between the PSC performance and the application of an amorphous or crystalline SnO_2 film, or a porous or dense SnO_2 film remains unexplored. Therefore, this research addresses this deficiency, in order to obtain further understanding of correlations between PSC performance, and material and interfacial properties. Nevertheless, in this research the environmental stability of PSCs with ALD SnO_2 has not been addressed, though in other literature it was shown that a barrier layer of ALD SnO_2 significantly improved this [60, 62].

2.4 Summary

In this chapter, the perovskite crystal and its photovoltaic application have been introduced. Furthermore, the challenges that PSCs currently face have been elaborated, among which especially the environmental stability and J-V hysteresis appear to be the main concerns. Then, some solutions for these challenges have been presented, including the planar configuration, partial substitution of constituents, and the application of an inorganic ETL, which have already been adopted in our PSC design. Lastly, the supposed requirements for inorganic ETLs have been discussed, which include layer electrical continuity, optical transparency, and suitable energy levels. Thereby, examples of suitable inorganic ETLs have been provided, with a special focus on the past recent research into the application of ALD SnO_2 as an ETL in PSCs.

[4] C_{60}-SAM: buckminsterfullerene self-assembled monolayer.

Chapter 3

Experimental Details on Characterization Methods and Fabrication of Perovskite Solar Cells

In this chapter, first a description is given of the methods applied for the compositional, structural and morphological, electrical, optical and energy level characterizations performed on the atomic layer deposited tin oxide and/or the complete perovskite solar cells. This serves as a theoretical background for the subsequent results chapters; every section specifies the physics on which the measurement relies, the experimental details, and the outcome(s) it provides. Second, a comprehensive explanation about electrochemical impedance spectroscopy is provided, among other things, containing the utilized theoretical, physical principles, the measurement set-up and proceedings, and the interpretation of the measurement data. Third, details on the perovskite solar cell fabrication are presented, followed by their performance characterizations.

3.1 Compositional Characterization Techniques

3.1.1 X-ray Photoelectron Spectroscopy

Equipment applied: *K-Alpha^{TM}+ X-ray Photoelectron Spectrometer (XPS) System, ThermoFisher Scientific*

X-ray photoelectron spectroscopy (XPS) can be applied to determine, among other things, the elemental composition, chemical state, and electronic state of a material surface. To this end, a sample in an ultra-high vacuum (10^{-8} mbar) is irradiated with monoenergetic X-ray photons, which are able to emit bonded core electrons until approximately 10 nm below the material surface. By examining the kinetic energy of these emitted electrons, the binding energies they experienced and the work function of the material can be determined using the following formula:

$$E_{kin} = E_{ph} - E_{bin} - \Phi, \tag{3.1}$$

where E_{kin} is the kinetic energy of an emitted electron, E_{ph} is the energy of the incident X-ray photons (Al K_α, 1486.7 eV), E_{bin} is the binding energy of an electron in a bonded state (also called: ionization energy), and Φ is the work function that is dependent on the sample material and the spectrometer itself.

Since every element has its own characteristic set of electron binding energies, the material composition can be qualitatively identified by comparing peak positions in an XPS spectrum with literature values. Furthermore, the relative elemental composition of the studied material can be quantitatively constituted using the number of detected electrons per element. In order to more accurately measure this, scans on a small range can be executed with a high resolution of 0.1 eV. This all gains understanding about, for instance, whether the sample consists of elements that were expected, whether there is surface contamination, what stoichiometry the material approximately adopts, and which specific atomic bonds are present.

Moreover, a sputtering function can be applied to further extend knowledge about the bulk of a material. An argon ion sputtering tool is able to remove an adjustable level of material, after which again an XPS measurement can be performed. Consequently, surface contamination can be removed, or also a so-called "depth profile" of the material can be composed.

Lastly, apart from the compositional characterization XPS is capable of measuring the valence band maximum (VBM) of a material too. By slowly scanning the first few electronvolts (eV) of binding energies, a steep increase in counts appears at the VBM energy, which indicates the position of the material's Fermi level with respect to the valence band ($E_F - E_V$).

However, there are also drawbacks to be considered for this measurement technique. First, light elements such as hydrogen and helium cannot easily be detected by which, for example, hydrogen doping in a film is hardly detectable. Second, oxygen could be preferentially removed during the sputtering, after which the oxygen content could be underestimated.

3.1.2 Rutherford Backscattering Spectrometry & Elastic Recoil Detection

Equipment applied: *2MV Tandetron, High Voltage Engineering Europe (measurement performed by Detect99)*

Rutherford backscattering spectrometry (RBS) is a diagnostic tool to verify material structure and composition. High-energy alpha particles (He^+, 1900 keV) are shot on stationary particles in the sample to be measured. Ideally, the alpha particles elastically collide with the stationary particles (i.e., no energy or momentum is transferred), since the stationary particles are generally heavier (see Figure 3.1a). According to the laws of energy and momentum conservation:

$$E_{scat} = k \cdot E_{in}, \tag{3.2}$$

where E_{scat} and E_{in} are the energies of the alpha particle after and before the collision, respectively, and k is the kinematical factor. This factor is defined as:

$$k = \left(\frac{m_1 \cos\theta_1 + \sqrt{{m_2}^2 - {m_1}^2 \cdot \sin^2(\theta_1)}}{m_1 + m_2} \right)^2, \tag{3.3}$$

where m_1 and m_2 are the masses of the alpha particle and a stationary nucleus inside the sample, respectively, and θ_1 is the scattering angle of the alpha particle (in the laboratory frame of reference). Since m_1 and E_{in} are known, and the variety of θ_1 and E_{scat} combinations can be measured by a rotational detector, corresponding values for m_2 can be calculated. By comparing them to known atomic masses, the elemental composition inside the sample can be investigated.

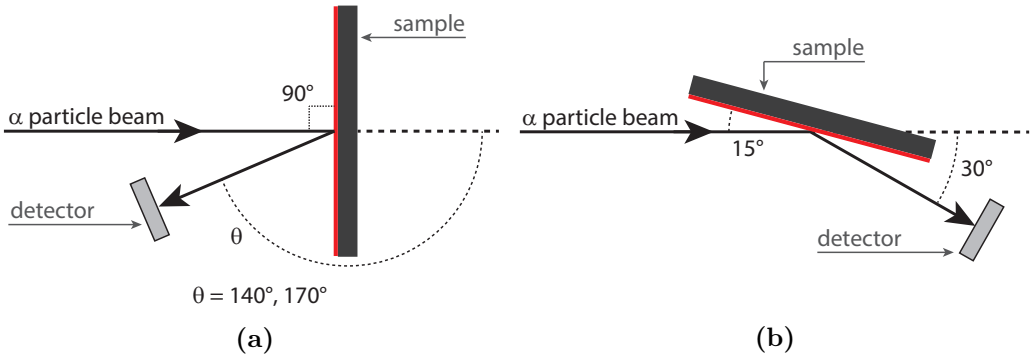

Figure 3.1: *The schematic diagrams for RBS (a) and ERD (b) measurements. For RBS, a beam of alpha particles is shot on a sample perpendicularly, by which they are scattered back. Each particle scatters back under a different angle θ and can be observed by a detector around the same angle. Here, 140° and 170° have been chosen as measurement angles. For ERD, the sample is positioned under a glancing angle (here: 15°), such that ejected hydrogen atoms can be detected by the detector (at 30°).*

Though, the described method only provides information about which elements are inside the sample; in this manner, still their absolute presences remain unresolved. This can be tackled by comparing the measured number of scattered alpha particles Q_{scat} within a certain solid angle with the known number of incident alpha particles Q_{in}. Then, for a certain element the number of stationary particles per cm^2 N_{stat} can be calculated via:

$$N_{stat} = \frac{Q_{scat}}{\sigma(\theta) \cdot Q_{in}}, \tag{3.4}$$

in which $\sigma(\theta)$ is the scattering cross-section. This σ is dependent of, among other things, the colliding elements, the initial energy of the alpha particle, and the scattering angle. In this manner, also the absolute concentrations of elements inside the sample can be determined.

With the same set-up, an elastic recoil detection (ERD) measurement can be performed. RBS mainly works for stationary particles heavier than alpha particles, but hydrogen atoms are easily recoiled instead of scattered against, due to their lower mass. Hereby, they can even be ejected from the sample. Thankfully, the very same system can also detect these hydrogen atoms by adjusting the angle in which the sample is placed. Namely for ERD, it is positioned at a glancing incidence angle (see Figure 3.1b). Eventually, this additional information about the hydrogen content inside a material can form a huge merit, for example, with respect to XPS measurement results.

N.B.: the RBS and ERD measurements performed in this research have the following accuracies: 7% for H, 4% for O, and 2% for Sn. Additionally, the detection limit for C is $20 \cdot 10^{15}$ at/cm^2.

3.2 Structural and Morphological Characterization Techniques

3.2.1 X-ray Diffraction

Equipment applied: *PANalytical X'Pert PRO MRD*

X-ray diffraction (XRD) or X-ray crystallography can be used to retrieve whether crystal structures are present in a material. Monochromatic X-rays (Cu K_α, 8.04 keV, 0.154 nm) are sent towards a sample under a certain angle ω, over where they are scattered by the atoms in the material, see Figure 3.2a. A diffraction spectrum can be composed

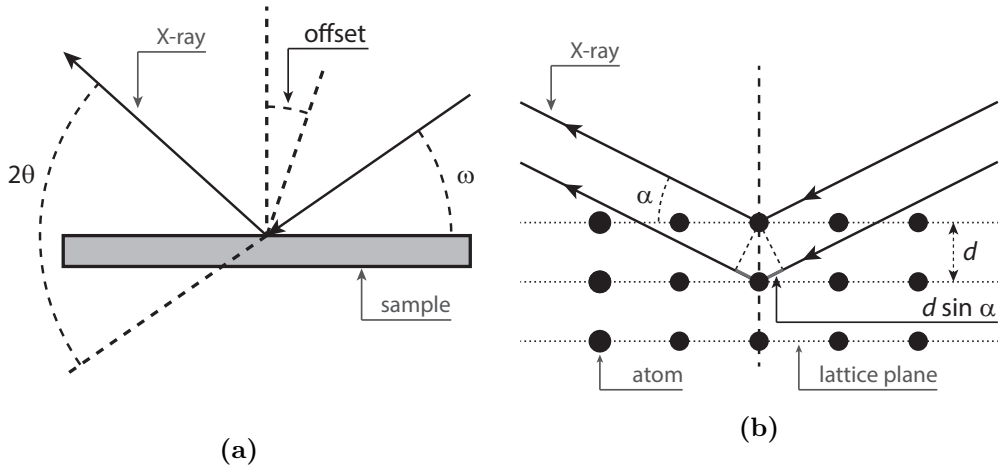

Figure 3.2: *Working principle of an XRD measurement. (a) Incident X-rays under an angle ω are diffracted on a sample and leave the sample under various angles 2θ. An offset can be applied to remove signals from the substrate. (b) As Bragg's law is satisfied, constructive interference occurs and much higher intensities are measured.*

by measuring the beam intensities as a function of the diffracted beam direction angles 2θ. These beam intensities become higher as more constructive interference occurs, which happens when multiple atomic lattice planes diffract X-rays in the same manner, and Bragg's law is satisfied:

$$2 \cdot d \cdot \sin\alpha = n \cdot \lambda. \tag{3.5}$$

Here, d is the distance between the diffracting atomic lattice planes, α is the angle of incident X-rays, n is an integer, and λ is the wavelength of the X-ray beam (see also Figure 3.2b). The measured angles, 2θ at which much higher X-ray intensities are detected, can be compared with literature values for the surveyed material. In such way, the crystal orientation(s) and its/their amount of presence in a sample can be determined. This indicates whether a material is monocrystalline, polycrystalline, or just amorphous.

Since in this research very thin layers had to be examined with XRD, grazing incidence diffraction (GI-XRD) has been applied beside the above described "gonio" measurement. In the GI-XRD mode, the incident beam angle is chosen very small and close to the material's critical angle. In this manner, diffraction from the surface can be measured with high precision, because the penetration of X-rays is restricted.

3.2.2 Transmission Electron Microscopy

Equipment applied: *JEOL ARM 200 (probe corrected)*

Transmission electron microscopy (TEM) is a microscopy technique in vacuum that images an ultrathin sample (< 100 nm) by transmitting electrons through it. Emitted electrons are first accelerated to an energy of 200 keV, since higher electron velocities decrease their wavelengths and provide enhanced sample penetration. Both these aspects eventually improve the image resolution. Second, multiple electromagnetic lenses are applied to diverge the electron beam before, and converge it after transmission through the sample to be imaged. Eventually, the modified beam consists of, among other things, transmitted, elastically and inelastically scattered and backscattered electrons that can be observed by various detectors.

In our measurements, transmitted electrons have been used to compose a sample picture on a charge-coupled device (CCD). Since local thickness or composition variations in the sample can scatter electrons differently compared to their surroundings, and (local) crystal structures can also diffract electrons, a lower number of electrons is finally transmitted straight through. Thus, via intensity variations in the image, the atomic structure of a thin layer can be studied, even with atomic accuracy (~ 0.2 nm). To examine our SnO_2 layers, special TEM-windows made of thin silicon nitride (SiN) with a ~ 5 nm coating of ALD SiO_2 have been applied. These TEM-windows contribute minimally to the eventual image, because of the low mass density and amorphous nature of SiN.

Apart from TEM top view images, also cross-sectional images can be manufactured to investigate the vertical structure of a sample. This has been performed for complete PSCs. To this end, a sample to be measured is first bisected by a focused ion beam. Gallium atoms from a liquid metal ion source are ionized by an electric field, then hit the sample surface, and consequently sputter away the sample atoms. In order to protect the sample top surface, a protective layer of platinum is deposited on top in advance. Afterwards, TEM can be applied to image the sample from the side in multiple measurement modes. In this research, first a conventional bright field TEM image has been made, as described above. A second applied manner has been high angle angular dark field scanning transmission electron microscopy (HAADF-STEM). Here, a focused electron beam scans the sample to be measured according to a raster, and the electrons that scatter or diffract from the surface towards outside the main transmitted beam are used to produce an image with atomic resolution.

3.2.3 Scanning Electron Microscopy

Equipment applied: *FEI MK2 Helios Nanolab 600*

Scanning electron microscopy (SEM) is a high-vacuum ($\lesssim 5{\cdot}10^{-5}$ mbar) imaging technique that uses electrons to image the surface top view of a sample. An electron beam is focused and accelerated by electromagnetic lenses to an energy of 2.00 keV, and scans a surface according to a predefined raster. The electrons interact with the surface atoms, and two types of all detectable electrons are utilized to compose an image, which are backscattered and secondary electrons. Backscattered electrons are the incident electrons that are scattered by the atomic nuclei, and secondary electrons are formerly core electrons that are ionized by incident electrons. By combining the number of detected electrons with the scanned raster positions, information is obtained about the topography of the sample. High-resolution images can therefore be composed in order to study a material surface. However, it should be taken into consideration that figures can become somewhat blurred if the sample cannot discharge from electrons. This usually happens when, for instance,

the substrate is composed of very resistive material. Finally, cross-sectional images can be made with SEM too, after bisecting the samples in a similar manner as described for TEM (see Section 3.2.2).

3.3 Electrical Characterization Techniques

3.3.1 Hall Effect

Equipment applied: *ECOPIA Hall Effect Measurement System HMS-5300*

The Hall effect can be used to eventually determine, among other things, the charge carrier density, the resistivity, and the charge carrier mobility of a material. An electric current I_x is sent through a material to be measured, and simultaneously a magnetic field B_z is applied on the sample: see Figure 3.3. Thereby, the charges in the material experience the

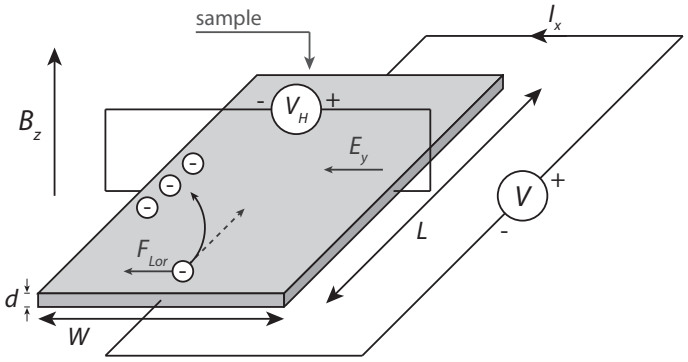

Figure 3.3: *The set-up to measure the Hall effect. A current I_x is sent through the material to be measured, while a magnetic field B_z is applied on it too. Hereby, the incoming electrons experience the magnetic part of the Lorentz force F_{Lor}, by which they bend towards one edge of the sample. Over there they accumulate, causing a potential difference V_H between the two edges of the sample.*

magnetic part of the Lorentz force F_{Lor}, in the direction perpendicular to both I_x and B_z. This causes separation of positive and negative charges, each moving towards an opposite side of the material. Definitely, this charge separation generates an electric field E_y in the sample, which increases as large as necessary to cancel the Lorentz force.

The final electric field that can be quantified by measuring the potential over the two opposite edges. This potential is called the Hall voltage V_H and can be calculated via:

$$V_H = \frac{I_x B_z}{den_e}, \tag{3.6}$$

in which d is the thickness of the sample, e is the elementary charge, and n_e is the electron density. Since for a measurement I_x, B_z, and d are known and V_H can be measured, the electron density n_e can be calculated.

Moreover, the resistivity ρ can be easily determined by measuring the voltage over and current through the sample, while the magnetic field is turned off. From the resistivity and the known electron density, both the conductivity σ and the electron mobility μ_e can be calculated using:

$$\frac{1}{\rho} = \sigma = n_e \cdot e \cdot \mu_e. \tag{3.7}$$

N.B.: aforementioned equations are applicable for n-type semiconductors with mainly electrons as charge carriers.

3.4 Optical and Energy Level Characterization Techniques

3.4.1 Spectroscopic Ellipsometry

Equipment applied: *UV VASE® Ellipsometer M2000D (ex situ) and NIR Ellipsometer M2000U (in situ), J.A. Woollam Co.*

Spectroscopic ellipsometry (SE) measures the difference in light polarization between an incident and a reflected light beam, upon reflection on a sample to be investigated. See Figure 3.4 for a schematic of the set-up. The measured polarization difference is compared to a mathematical model in order to calculate dielectric properties of a sample material, such that, for instance, its thickness, optical band gap, absorption coefficient, and refractive indices are revealed.

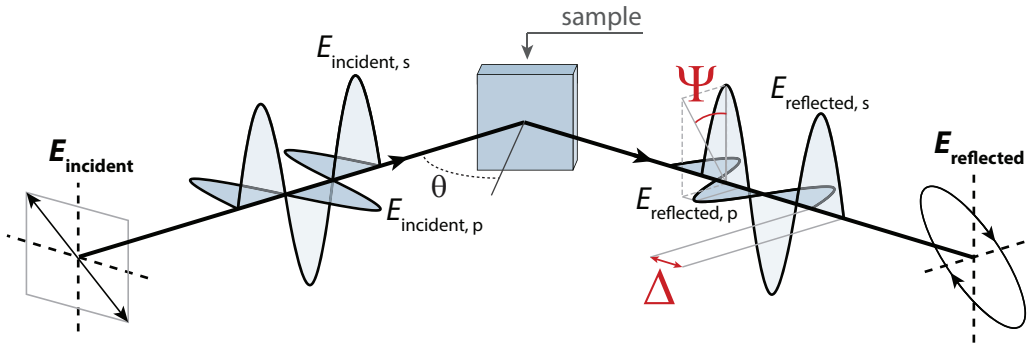

Figure 3.4: *A schematic representation of the SE working principle. Incident light with electromagnetic s- and p-components $E_{incident,\ s}$ and $E_{incident,\ p}$ is reflected on a sample under angle θ, after which a light polarization difference occurs and the reflected electromagnetic components are $E_{reflected,\ s}$ and $E_{reflected,\ s}$. These s- and p-components have different amplitudes and a phase difference, represented by Ψ and Δ, respectively.*

Quantitatively, the polarization difference is given by an amplitude ratio Ψ and a phase difference Δ between the s- and p-components[1] of the incident and reflected electromagnetic radiation. The amplitudes of the s- and p-components of the reflected light beam are normalized to the incident values, by which complex Fresnel reflection coefficients r_s and r_p are obtained. Then, the complex reflectance ratio ρ is calculated via:

$$\rho = \frac{r_p}{r_s} = \tan\Psi \cdot e^{i\Delta}. \tag{3.8}$$

In order to obtain the aforementioned dielectric properties, first the polarization differences are determined for a broad spectral range, for instance, from 0.75 eV until 5.00 eV (for NIR-SE), or from 1.25 eV until 6.50 eV (for UV-SE). Moreover, in this research the reflection angle θ has been varied between 65° and 75° in steps of 5°, for the *ex situ* measurements in particular. Second, all these data can be fitted by using applicable mathematical models, which finally compute the desired physical quantities.

For this research, the Cauchy model has been applied to determine layer thicknesses and growth per ALD cycle, and the Tauc-Lorentz model has been adopted to quantify dielectric functions $\varepsilon(E_{\text{photon}})$. From the dielectric function, the extinction coefficient $k(E_{\text{photon}})$ has been applied to calculate the absorption coefficient $\alpha(E_{\text{photon}})$. Via this

[1]The s-component is oscillating perpendicular to the plane of incidence, and parallel to the sample surface. The p-component is oscillating parallel to the plane of incidence.

absorption coefficient, eventually the optical band gap of the materials could be determined, by checking the photon energy at which $(\alpha h\nu)^2$ shows a steep increase. Hereby, it has been assumed that our material, SnO_2, has a direct band gap.

3.4.2 Ultraviolet-Visible-Near Infrared Spectroscopy

Equipment applied: *Agilent Cary 5000*

Ultraviolet-visible-near infrared spectroscopy (UV-VIS-NIR) is capable of measuring the transmittance and reflectance of a material for a broad wavelength range (175 - 3300 nm). For instance, the transmittance T is determined from the incident light and the transmitted light intensities I_{in} and I_{trans}:

$$T = I_{trans}/I_{in}. \tag{3.9}$$

From the two quantities transmittance T and reflectance R, also the absorbance A can be calculated:

$$A = 1 - R - T. \tag{3.10}$$

These three properties indicate, for example, whether a material is suitable to be applied as an ETL in a PSC, since ETLs have to be transparent for photons in the light range that has to be absorbed by the perovskite.

3.4.3 Ultraviolet Photoelectron Spectroscopy

Equipment applied: *VG EscaLab II (multichamber), ThermoFisher Scientific*

Ultraviolet photoelectron spectroscopy (UPS) is a diagnostic tool to measure the molecular orbital energies in the valence range. It functions similarly to XPS (see Section 3.1.1), but instead of X-rays it applies ultraviolet radiation from a helium gas discharge (He I, 21.2 eV) in an ultra-high vacuum (10^{-8} Pa). Since the energy of these photons is lower, the method is not able to measure high orbital binding energies; though, it is capable of measuring a low energy range with a higher accuracy. Additionally, it can only reach 2 to 3 nm below the material surface, in contrast to a ~ 10 nm measurement depth for XPS.

By applying this method, more precise values of the valence band maximum (VBM) and the work function (WF) of a material can be determined. The VBM value is equal to the lowest binding energy for which electrons are detected (similar to XPS), and the WF value can be determined by subtracting the energy width within which electrons are detected from the initial photon energy. To enable both these determinations, the Fermi level has to be calibrated at a binding energy of 0 eV. Eventually, the ionization potential (IP) can be calculated by summing the VBM and the WF values.

3.5 Electrochemical Impedance Spectroscopy

Electrochemical impedance spectroscopy (EIS) can be adopted to measure the frequency-dependent impedance of a material. An AC voltage is applied across an electrochemical cell, which contains an electrolyte solution and a sample to be researched, and simultaneously the current response of this system is measured. Hereby, the impedance of the system can be calculated for a broad frequency spectrum, via which various material properties can be studied in high detail. Therefore, EIS has been widely applied to characterize thin films, for example, to research their corrosion protection, or their use in solar cells, batteries, and (bio-)sensors [63].

In this research, EIS has been adopted to qualitatively describe bulk and interface material properties via the raw measurement data, and to quantitatively determine material doping densities via the Mott-Schottky approach. In the next sections, a description is provided on:

- the theoretical, physical principles on which the characterizations are based;
- the general functioning of EIS and the experimental details on the specific set-up and procedures applied in this research;
- the qualitative and quantitative EIS data processing in order to obtain physical understanding of the bulk and the interface.

3.5.1 Theoretical Background

Formation of a Schottky Barrier

The theory elaborated in this section has been especially based on [64, 65].

Most decisive for the impedance of a system is the interface between the electrolyte solution and the sample to be characterized, which contains in our case an n-type semiconducting material. As the electrolyte and the sample form a junction, charges flow across the interface to minimize the potential energy of the system. Usually, this is caused by a work function difference between the two materials. Then, these flowing charges may accumulate at or near the interface, for instance, at dangling bonds at the semiconductor surface, or at oxygen atoms and impurities in the semiconductor near the interface.

Consequently, the initial electronical properties of the interface are affected. To visualize this, the energy band diagrams of various configurations of a sample - solution system are displayed in Figure 3.5. Figure 3.5a shows the conduction band (CB), valence band

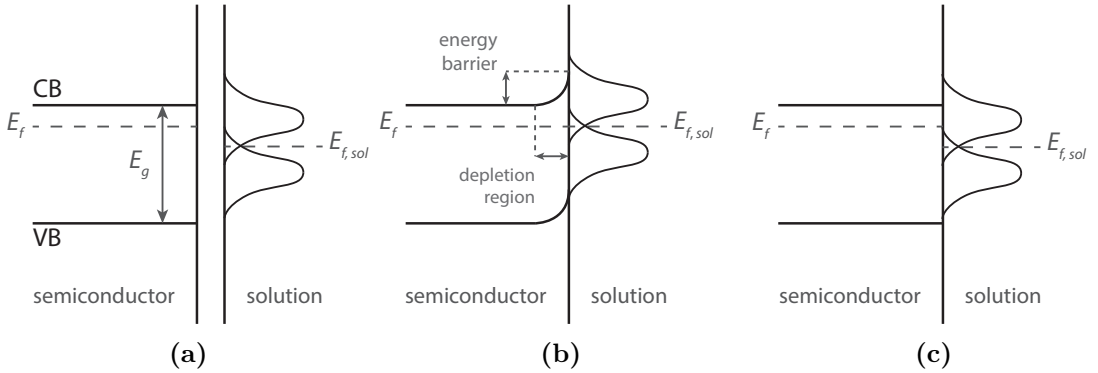

Figure 3.5: *Schematics of energy band diagrams of various configurations of a system containing a sample with semiconducting material, and an electrolyte solution. (a) The sample and the solution have been separated. (b) The sample and the solution have been connected, by which band bending has occurred. (c) A forward bias has been applied such that the energy barrier has disappeared.*

(VB), Fermi level (E_f) and band gap (E_g) of the semiconducting material (left), and the distribution of various energy states in the solution with their own Fermi level ($E_{f,sol}$) (right). If E_f is higher than $E_{f,sol}$ such as depicted, electron flow from the sample towards the solution aligns the two Fermi levels. However, hereby the electrons can get trapped as mentioned before. Consequently, other electrons are repelled from the interface and

a depletion region inside the sample is established. Furthermore, band bending upwards is caused such that an energy barrier eV_b is formed, and eventually electron flow across the interface is reduced. This phenomenon is called a Schottky barrier, and is depicted in Figure 3.5b.

As an external voltage is applied across the interface, the band bending can be adapted. If a reverse bias of magnitude V is applied such that the solution is negative, the depletion region becomes broader and the energy barrier increases even further to $e(V_b + V)$. However, if a forward bias of magnitude V is applied such that the solution is positive, the barrier decreases to $e(V_b - V)$ and current can more easily flow. When this forward bias is equal to the barrier voltage itself, the upward band bending even disappears (see Figure 3.5c). The bias at which this happens is called the flat-band potential V_{fb}.

In conclusion, the band bending at an interface of a semiconducting material and an electrolyte solution greatly influences the interfacial electrical properties, whether or not in combination with a bias potential. However, beside a qualitative physical knowledge of, for instance, this Schottky barrier, its charge current behavior can also be easily quantified by treating it as an electrical circuit, with components such as capacitors and resistors. In the next section, a description is provided on how to derive physical quantities from the Schottky barrier by modeling it as an electrical circuit with a capacitor.

Mott-Schottky Analysis

The theory elaborated in this section has been especially based on [65, 66].

The Schottky barrier as depicted in Figure 3.5b can be considered as a parallel plate or double layer capacitor. In the semiconducting material, positive charge accumulates near the interface as a consequence of the Schottky barrier. In the electrolyte solution, this positive charge is balanced by a sheet of negative charge near the interface. Thus, positive and negative charge are separated from each other at a non-conductive interface, which is similar to a capacitor.

The Mott-Schottky equation describes the capacitance of this double layer for any applied bias voltage:

$$C^{-2} = \frac{2}{\varepsilon_0 \varepsilon_r A^2 e N_D} \left(V - V_{fb} - \frac{k_B T}{e} \right). \tag{3.11}$$

Here, C is the interfacial capacitance, ε_0 is the vacuum permittivity, ε_r is the relative permittivity of the semiconducting material, A is the interfacial surface area, e is the elementary charge, N_D is the doping density of the semiconducting material, V is the applied bias potential, V_{fb} is the flat-band potential, k_B is the Boltzmann constant, and T is the temperature of the system. For a complete derivation of this equation, the reader is referred to [65].

When the capacitance is determined for a variety of applied bias potentials, a (C^{-2}, V) plot can be designed in which a linear relation should be discernible. By fitting this linear behavior following $C^{-2}(V) = r \cdot V + s$, N_D can be determined from the slope r according:

$$N_D = \frac{2}{\varepsilon_0 \varepsilon_r A^2 e} \cdot \frac{1}{r}. \tag{3.12}$$

Moreover, the energy distance between the conduction band minimum and the Fermi level of the semiconducting material $E_C - E_F$ can be calculated via:

$$E_C - E_F = \frac{k_B T}{e} \ln \left(\frac{N_C}{N_D} \right), \tag{3.13}$$

in which the effective density of states in the conduction band N_C is determined via:

$$N_C = 2\left(\frac{2\pi m^* k_B T}{h^2}\right)^{3/2}. \tag{3.14}$$

Here, m^* is the electron effective mass of the semiconducting material and h is the Planck constant.

In order to perform this Mott-Schottky analysis, EIS can be adopted to acquire the interfacial capacitance C as a function of the bias voltage V, since it can measure frequency dependent impedances of a system under different applied bias voltages. In the next sections, it is described how these impedance data are obtained by EIS, and how the capacitance values can be derived from them.

3.5.2 Electrochemical Impedance Spectroscopy Measurement

The theory elaborated in this section has been especially based on [67].

As described before, the basis of an EIS set-up consists of an electrochemical cell with an electrolyte solution, in which the sample to be measured is inserted. To construct an electrical circuit, two electrodes are placed inside the solution: the sample itself is one of the electrodes, and a metal is usually the other electrode. Then, across the cell a DC bias voltage V_{DC} is applied, together with a small AC voltage V_{AC} on top: $V(t) = V_{DC} + V_{AC} \cdot \sin(\omega t)$, in which ω is the (angular) AC frequency and t is the time. Concurrently, the system current response $I(t) = I_{DC} + I_{AC} \cdot \sin(\omega t + \varphi)$ is measured, which can have a phase difference φ with respect to the voltage signal, and the impedance $\mathbf{Z} = \frac{V(t)}{I(t)}$ can be calculated. This procedure is then followed for a certain set of frequencies, by which finally the impedance as a function of frequency $\mathbf{Z}(\omega)$ is obtained.

Before the qualitative and quantitative analysis of this $\mathbf{Z}(\omega)$ is treated, for example, to obtain $C^{-2}(V)$ for the Mott-Schottky analysis, the EIS set-up applied for these measurements is presented in the next section, together with an overview of the measurement settings.

Experimental Set-up and Settings

Equipment applied: *Metrohm Autolab 86265, potentiostat-galvanostat PGSTAT30, Frequency Response Analyzer module*

In Figure 3.6, a schematic of the EIS set-up is given (left), combined with a schematic of the sample configuration (right). The electrochemical cell filled with ~ 300 mL electrolyte solution has established the basis of the set-up. The electrolyte solution has been chosen to be a HCl solution (30%, VWR Chemicals) diluted with ultrapure water to a pH of 2.6, together with 0.5 M of dissolved KCl (EMSURE®)[2]. The so-called working electrode has consisted of the sample to be characterized, and a platinum mesh has served as the counter electrode. A reference electrode (Ag/AgCl in saturated KCl solution) has been utilized to provide an electrochemical reference potential. Eventually, these all have been placed inside a Faraday cage to prevent external interferences, and all measurements have been performed in ambient air under room temperature.

Outside this cage, the electrodes have been connected to a potentiostat instrument that has both provided the working potentials and measured the current responses. Dependent on the measurement, the bias potentials V_{DC} have been varied from maximally 1.6 V until

[2]Similar to the solution reported by Kavan *et al.* (2017) [61].

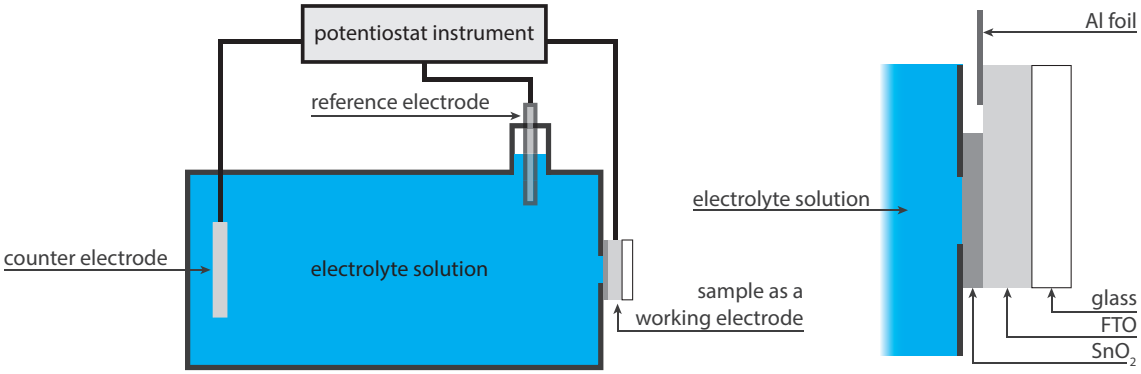

Figure 3.6: *A schematic of the EIS set-up (left) and the configuration of the connected sample as a working electrode (right). An electrochemical cell is filled with an electrolyte solution, after which a potentiostat instrument provides the desired potential over the working electrode and the counter electrode, with respect to the electrolyte potential measured by the reference electrode. Furthermore, the potentiostat instrument measures the current response, by which the system impedance can be determined. The sample consists of a stack of glass, FTO, and ALD SnO_2, and is connected to the electrical circuit via the FTO and aluminium foil on top.*

minimally -0.7 V via steps of 0.05 V or 0.1 V. To induce frequency dependent impedance behavior, a single sine wave has been chosen with V_{AC} relatively small (0.01 V, RMS) to make the current response pseudo-linear, since a highly non-linear response can easily be obtained in this case of an electrochemical cell. Per applied V_{DC}, frequency scans have usually ranged from $5 \cdot 10^5$ Hz until 10^{-1} Hz, with in general 50 logarithmically divided steps in between.

Sample Preparation

Glass with a fluorine doped tin oxide (FTO) layer (TEC^{TM} 15, Pilkington) has been chosen as a substrate material. First, these substrates have been ultrasonically cleaned in both acetone and ethanol for 10 minutes each. Then, via the method described later in Chapter 4, the samples have been treated with an oxygen plasma, and an ALD SnO_2 layer has been deposited on top of the FTO layer. One part of the substrate has been kept free from SnO_2 deposition, as depicted in Figure 3.6 (right). Hereby, the current should travel through the entire SnO_2 layer before it can be detected by the system via the conductive FTO layer and aluminium foil.

Before each EIS measurement, the samples have been treated again with an oxygen plasma[3], to simulate the procedure for the production of PSCs and thereby have a more comparable interface during this measurement. Subsequently, the samples have been connected to the electrochemical cell, and the cell has been filled with electrolyte solution as soon as possible, to prevent surface contamination from ambient air. Then, the measurement could be started. Nevertheless, for some samples a delay time has been chosen between the moment that the electrochemical cell had been filled with solution and the start of the measurement, to check whether this would make a difference in the results. Eventually, 0.87 cm^2 of the SnO_2 layer has been in contact with the solution.

[3]Comparable to the pre-deposition plasma treatment described earlier.

3.5.3 Electrochemical Impedance Spectroscopy Data Processing

The theory elaborated in this section has been especially based on [67].

The impedance data $\mathbf{Z} = \frac{V(t)}{I(t)}$ can be presented as a complex number in two ways: $\mathbf{Z} = Z' + jZ'' = |Z|\exp(j\varphi)$. Here, Z' and Z'' are the real and the imaginary parts of the impedance, respectively, and $|Z|$ and φ are the modulus and the phase angle of the impedance, respectively. All these quantities can be dependent on ω. These components are conventionally used to depict the $\mathbf{Z}(\omega)$ in Nyquist or Bode plots; examples are provided by Figure 3.7. From these plots, it is possible to recognize the electrical com-

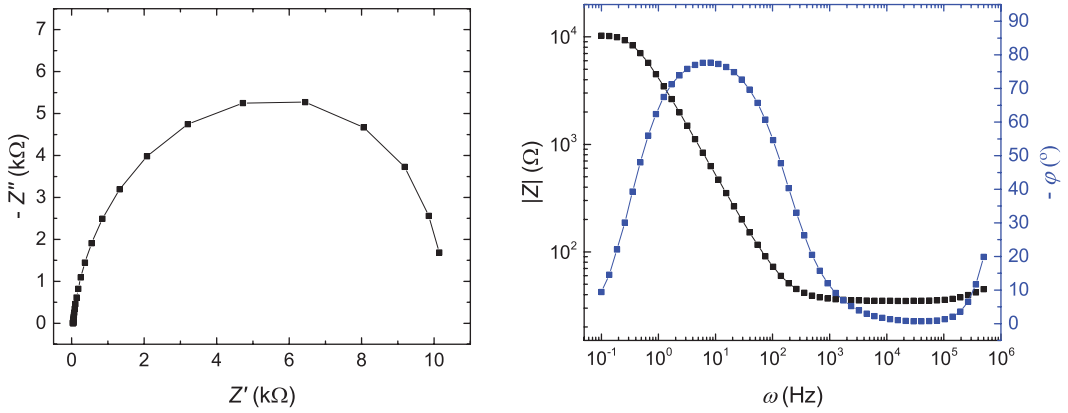

Figure 3.7: *The presentation of EIS measurement data in a Nyquist plot (left) and in Bode plots (right).*

ponents necessary to construct a circuit equivalent to the measured data. In a Nyquist plot $-Z''$ is plotted against Z', and in Bode plots $|Z|$ and $-\varphi$ are plotted against ω ($|Z|$ and ω usually on a logarithmic scale). When the shape of the graphs has been examined and processed into an electrical circuit, the data can also be fitted to determine the corresponding numerical characteristics of the circuit components.

In the subsequent paragraphs, first a description is provided on how to detect which electrical circuit is similar to the measured data of the sample - solution system. Furthermore, a method is provided to qualitatively analyze how the circuit component properties transform as the bias potential changes. Both can already provide physical understanding of the investigated system. Second, it is explained how this circuit can be fitted with software, in order to extract the actual values of the electrical components. The latter is most relevant for the earlier elaborated Mott-Schottky analysis.

Qualitative Analysis to Determine Electrical Circuit and Physical Interpretation

The theory elaborated in this section has been especially based on [68].

To recognize circuit components in the $\mathbf{Z}(\omega)$ data, it is necessary to understand their individual $\mathbf{Z}(\omega)$ behaviors. For a resistor and a capacitor, these $\mathbf{Z}(\omega)$ behaviors are described along $|Z|$ and $-\varphi$, since the Bode plots can be more straightforwardly examined. For a resistor, the impedance is frequency independent: $|Z|$ is equal to the resistance R and there is no phase angle ($\varphi = 0°$), for all frequencies. However for a capacitor, the impedance *is*

dependent on the frequency: $|Z| = \frac{1}{j\omega C}$, and the AC current response leads the AC voltage wave by $\varphi = -90°$. By knowing these properties per component, an electrical circuit can be designed that has a $\mathbf{Z}(\omega)$ equal to the measured data of the investigated system.

The general shape of a Bode modulus plot belonging to this sample - solution interface is given in Figure 3.8. In the high ω range $|Z|$ is constant (A), which indicates resistive

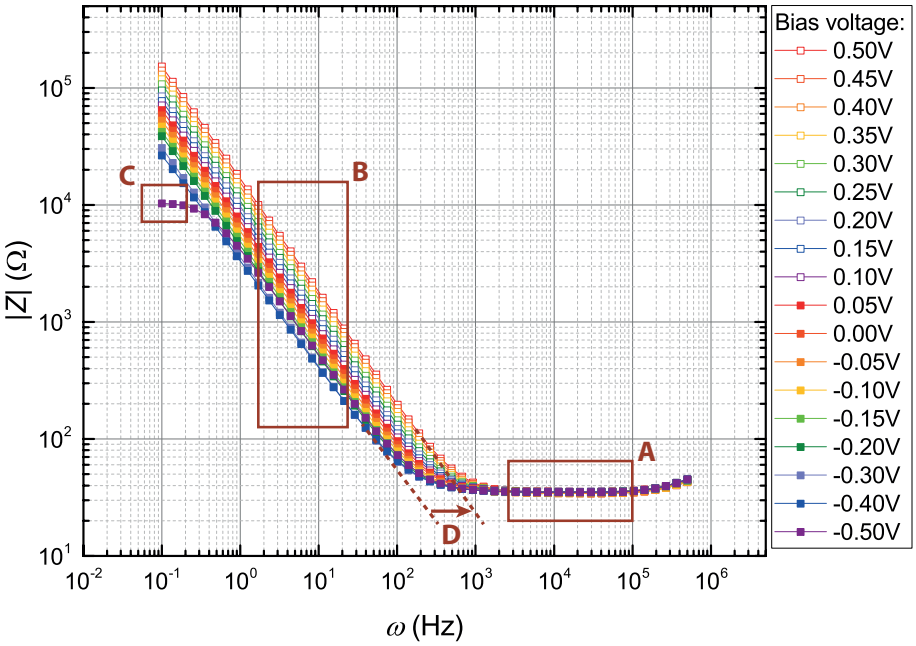

Figure 3.8: *General Bode modulus plots of EIS measurements on a sample - solution interface. Frequency scans have been sequentially performed for every indicated V_{bias} from 0.50 V to - 0.50 V.*

behavior. At some lower ω, $|Z|$ starts to increase for decreasing ω (B): this implies capacitive behavior. Lastly, usually for relatively low bias potentials it can be seen that $|Z|$ becomes constant again at relatively low ω (C). This reveals that the capacitive behavior is suppressed by another, stronger resistive behavior.

From these observations, it is clear that the electrical circuit should at least contain a resistor and a capacitor in parallel (that is non-ideal and thus a constant phase element (CPE), as will be described later), combined with a resistor in series. This circuit is called a "simple Randles" circuit, and has been depicted in Figure 3.9. For the series resistor,

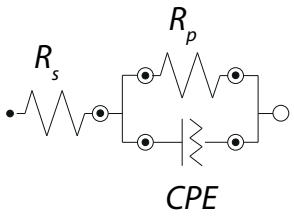

Figure 3.9: *The simple Randles electrical circuit: a resistor R_p and capacitor (actually, CPE) in parallel, in series with a resistor R_s.*

the value of R_s is roughly equivalent to the constant $|Z|$ at high ω (A), and the value of the parallel resistor is approximately corresponding to the constant $|Z|$ at low ω (C). From the slope of the capacitive part of the Bode modulus plot (B), the magnitude of the

capacitor can be determined. Though, it is easier to compare the values of capacitance C by evaluating at what ω the capacitive behavior starts (D); the higher the cut-off ω, the lower the value of C.

Nevertheless, the capacitive behavior belonging to the sample - solution system is rarely perfect. Usually, non-ideality has to be considered, for instance, due to an inhomogeneous sample surface. A proper manner to tackle this is to use a constant phase element (CPE) as a substitution for the capacitor. This CPE has an impedance equal to:

$$Z_{\mathrm{CPE}}(\omega) = \frac{1}{C \cdot (j\omega)^n}, \tag{3.15}$$

with n a non-ideality factor [61, 69, 70]. A perfect capacitor holds $n = 1$, but in practice n regularly has a value between 0.7 and 1. In the Bode modulus plot, a non-ideal capacitance can be more easily identified as the $|Z|$ slope towards lower ω is less steep than it should be according to $|Z| = \frac{1}{j\omega C}$.

Subsequently, a common example of a Bode phase plot is given by Figure 3.10. Sim-

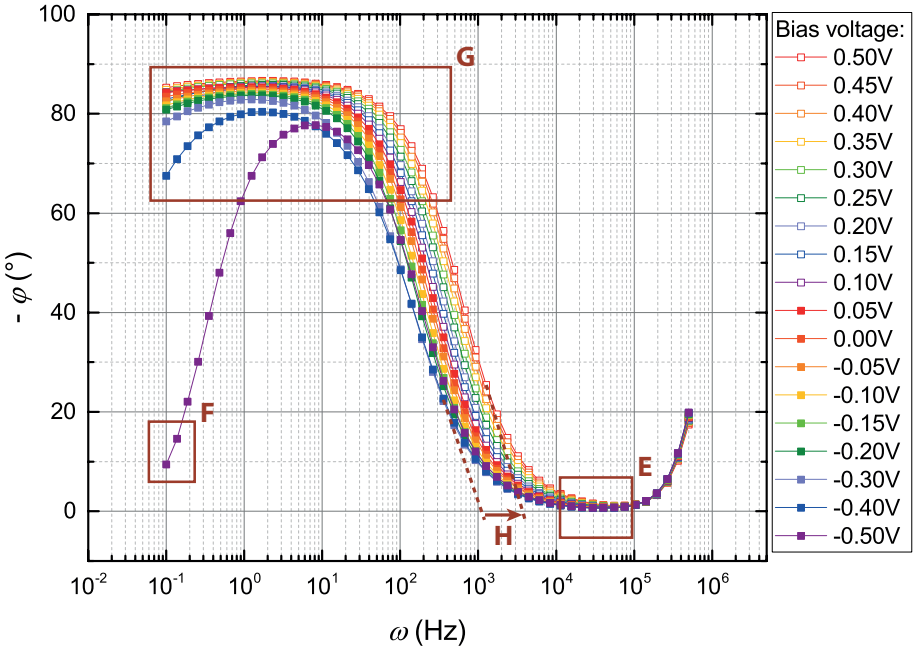

Figure 3.10: *General Bode phase plots of EIS measurements on a sample - solution interface. Frequency scans have been sequentially performed for every indicated V_{bias} from 0.50 V to - 0.50 V.*

ilarly, resistive behavior is observed at high ω, since the phase angle sticks at 0° (E). Furthermore, for the relatively low bias potential it goes towards 0° again for lower ω (F), indicating that the parallel resistance gains influence on the total impedance. In the mediate ω region, the phase angle goes towards $-90°$, but does not completely reach it (G). This additionally illustrates non-ideal capacitive behavior.

From this Bode phase plot one can also deduce some component properties. For instance, the broader the ω region for which the phase angle has the broad capacitance peak (G), the higher the value of R_p, since the phase only goes towards 0° again for resistive behavior. In the meantime, the capacitive behavior keeps magnifying $|Z|$, until R_p is large enough to suppress the impedance of the capacitance. Furthermore, the lower the maximum $-\varphi$ (G) the lower the value of n, so the less ideal the capacitor is. Eventually,

it also holds here that the higher the cut-off ω for which the $-\varphi$ starts to increase, the lower the capacitance value C (H).

In addition to finding the corresponding electrical circuit, this circuit should be physically interpreted. Considering the components in Figure 3.9, R_s represents the resistance caused by, among other things, the electrodes and the electrolyte solution. Of course, the CPE represents the interface between the sample and the solution, at which a Schottky barrier and thus a double layer capacitance is formed. Finally, R_p is included to count for the charges that do manage to pass the interface, and thereby experience resistance.

Quantitative Analysis to Determine Numerical Characteristics of Electrical Circuit Components

Beside the qualitative analysis as presented above, to determine the electrical circuit design, a quantitative analysis can be executed. Then, the numerical properties of the electrical circuit components as shown in Figure 3.9 are determined.

To this end, Nova software (Metrohm Autolab B.V.) has been applied, which adopts the non-linear least squares method to estimate the component characteristics from the measured data for all applied bias potentials. Hereby, the values R_s and R_p have been determined, as well as the admittance Y and ideality factor n of the capacitor. Usually, the excellence of the fits (given by χ^2) was maximally 0.01. From Y and n, the corresponding value of C was calculated via [61]:

$$C = \frac{(R_p \cdot Y)^{1/n}}{R_p}. \tag{3.16}$$

Eventually, these values of C for a range of bias potentials V have been utilized to perform the Mott-Schottky analysis.

3.5.4 Summary

In this EIS experimental description, it has been elaborated that we use the formation of a Schottky barrier at a sample - electrolyte solution interface to obtain physical understanding of the bulk and interface properties of semiconducting material. Via EIS, the frequency dependent impedance of this system can be investigated for various bias potentials, from which an equivalent electrical circuit can be constituted. Furthermore, by fitting the measurement data along this equivalent circuit, numerical characteristics of the circuit components can be obtained. These characteristics can be used to calculate the material doping density and the energy level distance between the conduction band minimum and the Fermi level via the Mott-Schottky analysis.

3.6 Fabrication and Characterization of Perovskite Solar Cells

3.6.1 Fabrication of Perovskite Solar Cells

For this research, perovskite solar cells have been fabricated at Solliance[4] in an n-i-p configuration, such as depicted in Figure 3.11. The production process starts with tin doped indium oxide (ITO) coated glass substrates (Naranjo B.V.): these have been ultrasonically

[4]Solliance: a solar energy R&D initiative of ECN, Holst Centre, imec, TNO, Forschungszentrum Jülich and TU/e. Solliance Solar Research, High Tech Campus 21, 5656AE Eindhoven.

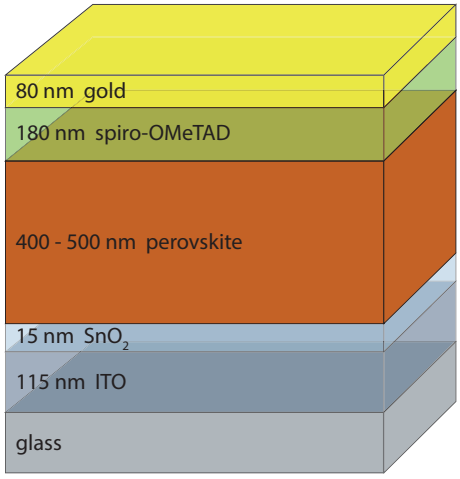

Figure 3.11: *Configuration of our n-i-p perovskite solar cell design. For each layer, the material and its approximate thickness have been indicated.*

cleaned for 5 minutes in dissolved detergent[5], deionized water, and isopropanol. Afterwards, 15 nm of ALD SnO_2 has been deposited according to the recipe described later in Chapter 4, at deposition temperatures of 50°C - 200°C. Subsequently, the proceedings have continued in a N_2 filled glovebox (0.1 ppm O_2, 0.1 ppm H_2O). Perovskite precursor solution has been prepared by mixing lead(II) iodide, lead(II) bromide, methylammonium iodide, formamidinium iodide, and cesium iodide in dimethylformamide[6]. To this end, a method reported elsewhere has been followed [19]. The ingredients have been chosen considering the arguments specified in Section 2.2.2. Eventually, this has led to the following perovskite composition: $Cs_{0.05}(MA_{0.15}FA_{0.85})_{0.95}Pb(I_{0.9}Br_{0.1})_3$.

Shortly prior to the spin-coating of the perovskite precursor solution, the SnO_2 covered ITO substrates have been cleaned by applying an O_2 plasma treatment at room temperature and 1 mbar pressure for 2.5 minutes, applying an RF power of 600 W. Then, perovskite precursor solution has been spin-coated on top of the substrates at a rotation speed of 5000 rpm for 60 seconds, using chlorobenzene[7]. Finally, the perovskite layer of $\sim 400 - 500$ nm has been annealed at a temperature of 100°C for 30 minutes, in order to crystallize the material. To finish the device, spiro-OMeTAD solution[8] has been spin-coated on top of the crystallized perovskite at 2000 rpm for 60 seconds, delivering an HTL layer of ~ 180 nm. After an overnight air exposure to dope the spiro-OMeTAD with oxygen, ~ 80 nm gold has been deposited on top via thermal evaporation. Eventually, the finished perovskite solar cells have been stored in a glovebox filled with N_2 to prevent decomposition of the perovskite crystals (as described in Section 2.1.2).

[5]Extran® MA 01, Sigma-Aldrich Co. LLC. Dissolved in deionized water, ratio 1:7.

[6]Lead(II) iodide: PbI_2, TCI Europe N.V. Lead(II) bromide: $PbBr_2$, Dyesol LTD. Methylammonium iodide: CH_3NH_3I or MAI, Dyesol LTD. Formamidinium iodide: $CH_3(NH_2)_2I$ or FAI, Dyesol LTD. Cesium iodide: CsI, TCI Europe N.V. Dimethylformamide: $(CH_3)_2NC(O)H$ or DMF, Sigma-Aldrich Co. LLC.

[7]Chlorobenzene: C_6H_5Cl, Sigma-Aldrich Co. LLC.

[8]The spiro-OMeTAD (Lumtec) has been dissolved for 80 mg/ml in chlorobenzene, which has been doped with 28.5 µL of 4-*tert*-butylpyridine (*t*BP; 96% purity, Sigma-Aldrich Co. LLC) and 17.5 µL of a 520 mg/ml solution of lithium bis(trifluoromethanesulfonyl)imide (LiTFSI; 99.95% purity, Sigma-Aldrich Co. LLC) in acetonitrile (CH_3CN; Sigma-Aldrich Co. LLC).

3.6.2 Characterization of Perovskite Solar Cells

Current Density - Voltage Curve

Equipment applied: *ABET Sun 2000 (Class A solar simulator), Keithley 2420 (source-meter)*
Current density - voltage curve (J-V) measurements can be performed to identify a solar cell's performance, which is usually quantified by the V_{OC}, J_{SC}, FF, and PCE. The first three quantities can be extracted from a (J, V)-graph, see Figure 3.12 for an example.

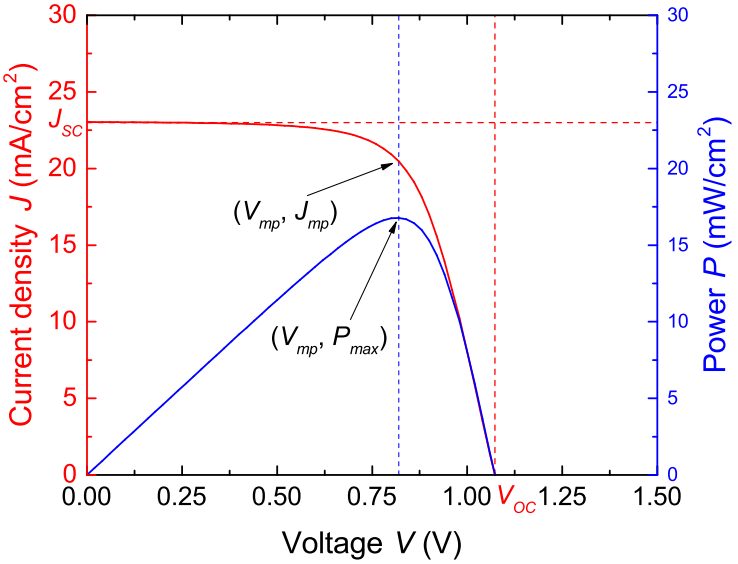

Figure 3.12: *Example of a (J, V)-graph (red, measured) combined with associated (P, V)-graph (blue, calculated). The red dashed lines indicate the V_{OC} and J_{SC}, the blue dashed line indicates the V_{mp} belonging to the maximum power point P_{max}. By extrapolating this line, the J_{mp} can be found.*

In such a graph, the current density J extracted from the solar cell is given as a function of the applied voltage V across its contacts. To be able to compare the performances of various solar cells, the following quantities are generally derived from the (J, V)-graph:

- the open-circuit voltage (V_{OC}): the voltage between the two cell contacts when no external circuit is connected, thus no current is flowing;
- short-circuit current density (J_{SC}): the current density as the voltage across the cell is zero;
- fill factor (FF): the maximum power obtainable from the solar cell divided by the product of V_{OC} and J_{SC}, indicating how well the cell approaches its maximum output;
- power conversion efficiency (PCE): the solar cell's energy output divided by the light source's energy input, indicating how efficiently the cell converts light into electricity.

In order to obtain these data, a solar cell is illuminated by a solar simulator that imitates natural sunlight of AM1.5G [9]. While this solar cell is illuminated, generally a range of voltages is applied across the solar cell and the corresponding current densities

[9] AM1.5G holds that the simulated spectrum is approximately the same as the direct and diffuse part of the solar spectrum, after having traveled through 1.5 times the Earth's atmosphere thickness.

are measured. Furthermore, the scan direction and scan rate of the voltage can be tuned; the voltage scan can start from positive to negative values (reverse scan) or from negative to positive values (forward scan), and with various scan rates in the order of mV/s or V/s. In the case of PSCs, choices for these two measurement settings can give very different J-V behavior (as described as hysteresis in Section 2.1.2).

To reveal the long-term performance of a solar cell, one can perform, for instance, a maximum power point (MPP) tracking measurement. Then, the performance of a solar cell is continuously characterized, by measuring the PCE at the maximum power point as a function of time. In this manner, it can be investigated whether a PSC's performance remains constant or not.

All our measurements have been performed in an N_2 environment (0.1 ppm O_2, 0.1 ppm H_2O), to prevent degradation of the solar cells. The solar simulator has radiated with 100 mW/cm^2 illumination power density, and the solar cells have been covered with a metallic mask that has a fixed aperture to illuminate the same active cell area during every measurement.

Photoluminescence Spectroscopy

Photoluminescence spectroscopy (PL) can be applied to examine the band gap of a semiconductor, and the radiative charge recombination within a material. The technique uses mono-energetic photons to excite electrons from the valence band to the conduction band, after which a large fraction of the excited electrons recombine with holes. Thereby, a photon is spontaneously emitted with another photon energy similar to the semiconductor band gap energy. By measuring light intensities over a broad spectrum with a charge-coupled device (CCD), a peak occurs at the certain band gap energy of the semiconductor. Beside recombination with holes within the semiconductor bulk, the excited electrons can be extracted from the material into another layer in contact, such as a hole or electron transport layer. Hereby, the semiconductor does not radiate a photon at the certain band gap energy, so the PL intensity peak decreases (called PL quenching). Both these events can be observed via a steady-state (SS) PL measurements, which in our case function continuously at a photon wavelength of 532 nm.

Furthermore, a time-resolved measurement (TR) can be executed: then, the photoluminescence intensity is measured as a function of time after the excitation by a short laser pulse, in our case at a photon wavelength of 635 nm. The longer the photoluminescence intensity stays high, the less radiative charge recombination or the less efficient charge extraction towards nearby layers occurs.

Chapter 4

Atomic Layer Deposition of Tin Oxide

At the end of Chapter 2, it is described why atomic layer deposition (ALD) is our preferential deposition technique. In this chapter, the ALD process we employed to deposit SnO_2 layers is presented in detail: the applied deposition set-up, precursor and co-reactant are discussed, together with the process development and a characterization of the layer thickness growth per cycle at various deposition temperatures. A general, extended description of ALD as a deposition principle can be found in Appendix A.

4.1 Set-up, Proceedings and Materials

4.1.1 ALD Reactor and General Procedure

Our ALD process has been developed in an OpAL reactor[1]. A schematic of this device is shown in Figure 4.1, accompanied by a description of its main parts in the figure caption.

Prior to SnO_2 depositions, the OpAL reactor chamber is covered with aluminium oxide (via thermal ALD) and SnO_2 itself, such that as little as possible contamination from previous ALD processes could occur. After heating up the loaded substrates to the desired deposition temperature at a base pressure of ~ 1 mTorr, the "ALD recipe" starts with an inductively coupled oxygen (O_2) plasma (RF power: 300 W, ~ 100 mTorr, 3 min) to remove environmental surface contamination and to initiate growth.

Subsequently, the first half-cycle begins by introducing precursor (TDMASn) to the reactor chamber. To this end, argon (Ar) is used as a carrier gas to bubble through it. The precursor molecules react with available surface groups of the substrate, and simultaneously release ligands. When ideally all reactive sites have been covered, the bubbler line and the reactor chamber are purged with Ar to remove reaction products and left-over precursor molecules. During the second half-cycle, the reactor chamber is filled with O_2 gas to stabilize at a pressure of ~ 100 mTorr, after which an inductively coupled plasma (RF power: 300 W) is ignited. This O_2 plasma removes the left-over organic ligands and leaves a (sub-)monolayer of SnO_2 behind. As this step has finished, the reaction products and left-over oxygen are purged and pumped away with Ar, and the next ALD cycle can start. Finally, all these steps are repeated for a predefined number of cycles.

[1] OpAL: *Compact open-load system for ALD*, Oxford Instruments plc.

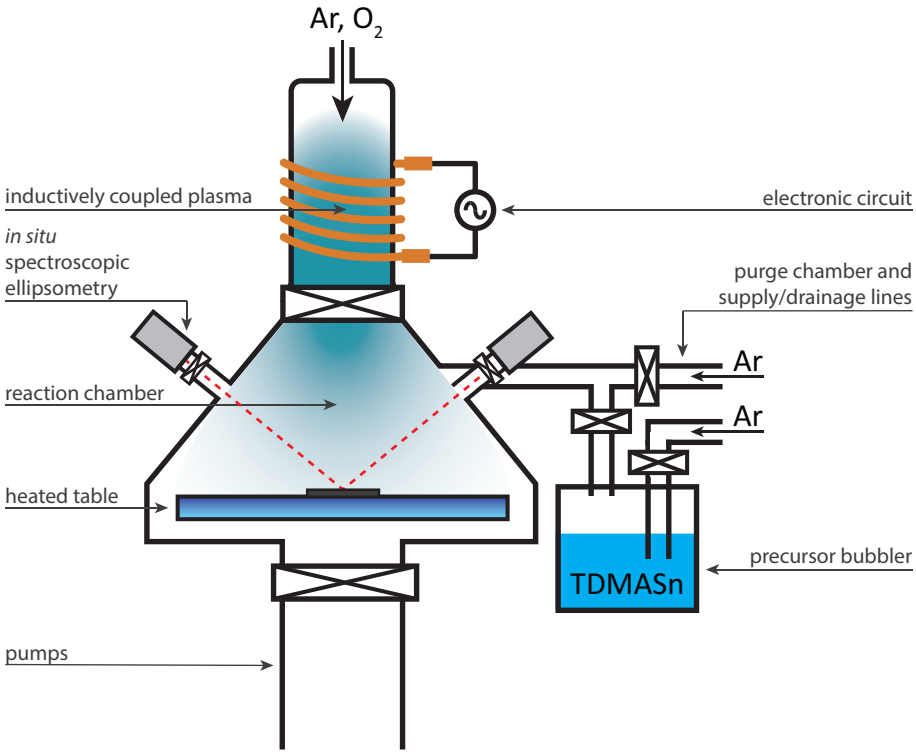

Figure 4.1: *Schematic of the OpAL system: the reactor chamber has a heated table on which substrates can be placed. Below the heated table, two dry pumps are available to initially pump down the reactor chamber to a processing pressure typically below 1 mTorr, and to pump away all reaction products and input gases during processing. The reactor chamber can be filled with precursor by flowing argon (Ar) as a carrier gas through the bubbler. Further on, the Ar supply line can be used to purge the reactor chamber with Ar. From the top, Ar can be introduced to purge the reactor chamber too, while through this entry also O_2 gas can be added to the reactor chamber. This O_2 can be turned into an O_2 plasma by igniting it with the inductively coupled plasma source. Lastly, an in-situ spectroscopic ellipsometer can be mounted to measure the dielectric properties of the layer that is being deposited, to determine its thickness and refractive indices.*

4.1.2 Choice of Precursor and Co-reactant

To produce SnO_2, various precursors incorporating tin can be chosen: for instance, tin-(IV)iodide (SnI_4) [71–73], tin(IV)chloride ($SnCl_4$) [71, 74, 75], and tetrakis(dimethylamino)tin(IV) (TDMASn, $((CH_3)_2N)_4Sn$; see Figure 4.2) [15, 22–24, 60–62, 76–79]. Among them, TDMASn (99.9 % purity, Sigma-Aldrich Co. LLC) has been adopted for our ALD process, since the use of the halide precursors can yield undesirable toxic gases and acids as reaction products [76, 81], such as Cl_2, HCl, I_2 and HI. These species may be harmful for the ALD system, and require careful waste management. Additionally, it has been shown in multiple investigations that processes with TDMASn deliver a higher growth per ALD cycle (GPC) compared to processes using $SnCl_4$ and SnI_4 [74–77, 79, 81]. Accordingly, by using TDMASn a shorter processing time is required to grow a layer, which is beneficial for both research and industrial purposes.

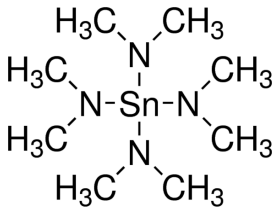

Figure 4.2: *Structural formula of the TDMASn precursor. Taken from [80].*

In combination with precursor TDMASn, studies have mainly adopted water (H_2O) [15, 23, 77, 79], hydrogen peroxide (H_2O_2) [76, 79], ozone (O_3) [22, 23, 78], and oxygen (O_2) plasma [23, 24] as a co-reactant. For this research, O_2 plasma has been selected since it produces high quality thin films for a wide temperature window (50°C - 200°C) [82], which is for this research an advantage because the TDMASn precursor decomposes at temperatures above $\sim$ 230°C [79]. Moreover, the O_2 only performs as a co-reactant while the plasma is activated. In this way, during subsequent steps no direct reaction can occur between precursor molecules and O_2 gas remaining from insufficient purge steps. Otherwise, this could lead to a chemical vapor deposition effect, reducing the quality of the SnO_2 films.

4.2 Development of ALD Recipe

In addition to the provided general overview of the ALD process, certain settings of the ALD recipe have to be chosen carefully in order to obtain a controllable and reproducible deposition, as also argued in Section A.3 in Appendix A. In this section, a description of the settings for the ALD SnO_2 process at a deposition temperature of 100°C is provided, involving the choice of recipe step durations and input gas flow rates to achieve a saturated and uniform growth. To be able to confirm these requirements, layer thicknesses have been measured using spectroscopic ellipsometry (SE).[2]

In order to design a useful sequence of recipe step durations, saturation curves have been developed to check for every ALD cycle timestep duration when the GPC saturates. To this end, various timestep sequences have been applied: for instance, the recipe x - 20 s - 5 s - 10 s - 5 s has been used to develop the TDMASn dose saturation curve. In this recipe, variable TDMASn dose times x have been chosen, succeeded by the fixed timesteps for TDMASn purge (20 s), O_2 gas pressure stabilization (5 s), O_2 plasma dose (10 s), and O_2 purge (5 s). Similarly, the TDMASn purge time, O_2 plasma dose time, and O_2 purge time have been varied to develop the TDMASn purge, O_2 plasma dose, and O_2 purge saturation curves, respectively. Every recipe with a unique variable timestep has been executed for 50 cycles on crystalline silicon substrates, with an initial SnO_2 layer of 5 nm. To determine the thickness growth, every 5 cycles an *in-situ* SE measurement has been performed.

The resulting saturation curves are presented in Figure 4.3, with the specific recipe that has been used to develop them given in the inset. As can be seen, the TDMASn dose step eventually shows no saturation; an effect that was observed earlier by Elam *et al.* (2008). They suggested that this may be attributed to a slow desorption of ligand products. Since these ligand products are likely to bind firmly to the hydroxylated SnO_2 surface, they could prevent new precursor molecules to react with the surface during the TDMASn dose

[2] A detailed description of this diagnostic tool can be found in Section 3.4.1.

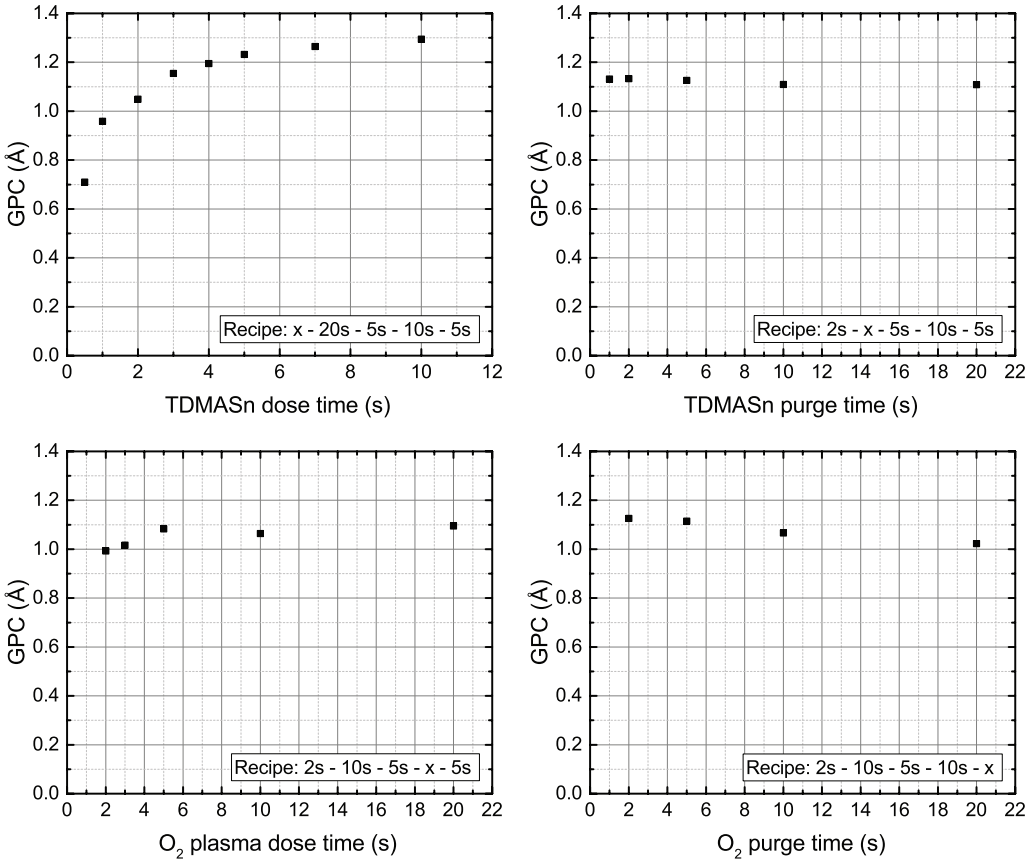

Figure 4.3: *Saturation curves for the ALD SnO_2 process development at a deposition temperature of 100˚C. The growth per cycle (GPC) has been determined for various timestep durations, for every ALD cycle step. The applicable recipe for this purpose is given in the inset. Data obtained via in situ SE measurements.*

step [76]. As the TDMASn dose step is chosen longer, some ligand products may desorb and give opportunities for precursor molecules to still bind to the surface. Thereby, the surface may seem unsaturated yet. Further on, it is clear that the TDMASn purge time can be kept short to reach growth saturation, since the GPC shows to barely decrease for longer timesteps such as 10 s and 20 s. Next, the O_2 plasma dose fully saturates after approximately 10 s, and finally the O_2 purge time exhibits only a tiny GPC decrease after 10 s.

From these data, a suitable ALD recipe has been designed to grow SnO_2; see Table 4.1 for the final choices made for the multiple timesteps during an ALD cycle. The recipe contains a TDMASn dose of 2 s since the deposition uniformity was good (as is shown in the next paragraph). Furthermore, a short dose time step is preferred for efficient processing and for potential processing on top of perovskite, given the reduced chemical stability of this material. Then, this dose step is followed by a long Ar purge of 10 s. Subsequently, first O_2 is introduced to the reactor chamber with a duration of 5 s to reach a stable gas pressure, before 10 s of inductively coupled plasma is ignited. Finally, 5 s of Ar purge is added to remove reaction products and left-over O_2.

To compare the uniformity between depositions performed with various combinations of input gas flow rates, the SnO_2 layer thickness growth has been measured at different positions on the reactor substrate table. The positions were chosen at the edges of imag-

inary 4" and 6" circular wafers, which would be centered on the OpAL substrate table. See the left of Figure 4.4 for a schematic of the positions. Then, Formula 4.1 is applied to

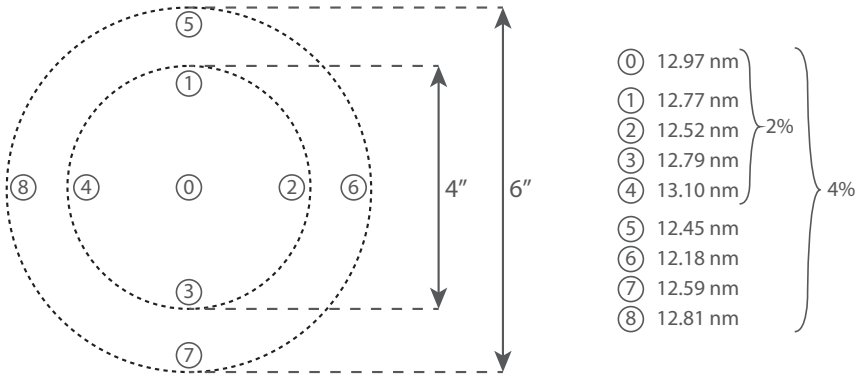

Figure 4.4: *Positions at which thickness is measured to determine the uniformity (left), together with the measured thicknesses themselves (right). Position 0 is at the center of the substrate table, 1-4 are at the edges of an imaginary 4" wafer, and 5-8 at the edges of an imaginary 6" wafer. Data obtained via ex situ SE measurements.*

easily, numerically compare the deposition uniformity of various recipes:

$$\text{uniformity} = \frac{\max(d_i) - \min(d_i)}{2 \cdot \text{average}(d_i)} \times 100\%, \tag{4.1}$$

in which d_i ($i = 0, 1, 2, ..., 8$) is the SnO_2 layer thickness measured at the indicated positions. Investigations have shown that the most optimal sequence of flow rates for the time recipe shown in Table 4.1 yields the thicknesses as shown at the right of Figure 4.4, which were determined from *ex-situ* SE data. Applying Formula 4.1, this means that favorable levels of uniformity were obtained: 2 % at the 4" positions and 4 % at the 6" positions for SnO_2 layers of 12 - 13 nm.

For a full detailed (technical) overview of the entire ALD recipe, see Table 4.1.

Table 4.1: *The final ALD recipe used in this research to deposit SnO_2, with all technical details.*

Recipe step	**TDMASn dose**	**TDMASn purge**	**O_2 gas stabilization**	**O_2 plasma**	**O_2 purge**
Argon bubbler (valve)	100 sccm (dose)	1 sccm (FB)	1 sccm (FB)	1 sccm (FB)	100 sccm (FB)
Argon purge (valve)	250 sccm (FP)	250 sccm (prec)	1 sccm (FP)	1 sccm (FP)	250 sccm (PT)
ICP flow	Ar: 100 sccm	Ar: 100 sccm	Ar: 20 sccm O_2: 100 sccm	Ar: 20 sccm O_2: 100 sccm	Ar: 100 sccm
Precursor	dose	-	-	-	-
ICP RF power	-	-	-	300 W	-
Duration	2 s	10 s	5 s	10 s	5 s

$T_{\text{bubbler}} = 45°C$. $T_{\text{precursor line}} = 65°C$.

Legend: FB: foreline for bubbler argon. FP: foreline for purge argon. PT: purge thermal. Prec: precursor line. sccm: standard cubic centimeters per minute, cm^3/min.

4.3 Growth of SnO_2 at Different Temperatures

After the described development of the ALD process at a deposition temperature of 100°C, the recipe described in the previous section has been extended to deposition temperatures 50°C, 150°C and 200°C. Figure 4.5 shows the SnO_2 layer growth against the number of cycles for the ALD processes at deposition temperatures of 50°C, 100°C, 150°C and 200°C. For all these temperatures, the GPC has been determined using the thickness growth during last 100 cycles: see the legend for the corresponding values. A linear growth

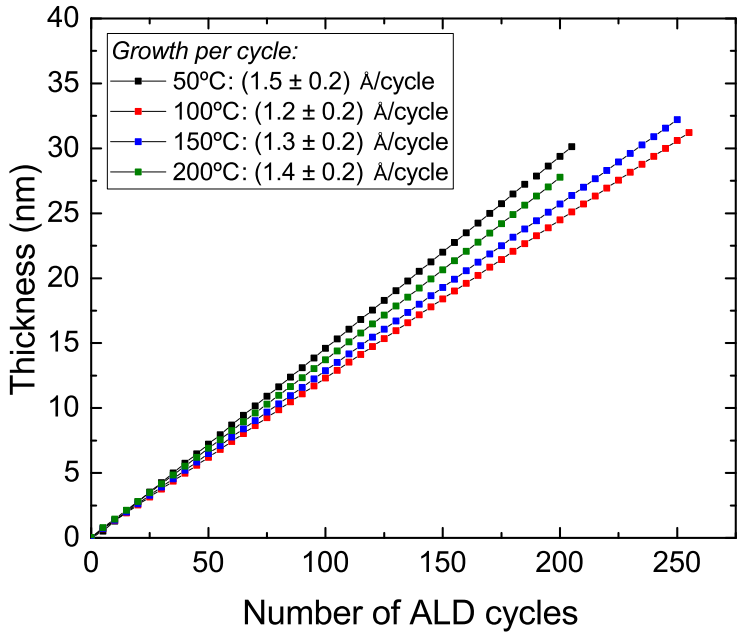

Figure 4.5: *Development of SnO_2 layer thicknesses as a function of the number of ALD cycles, for various deposition temperatures. In the legend, the accompanying GPCs can be found per temperature, which have an error of 0.2 Å/cycle on the basis of reproducibility. It is assumed that this error is related to the deposition system. Data obtained via in situ SE measurements.*

behavior without nucleation delay is observed for all the films deposited at the researched temperatures, without a significant temperature dependence in GPC since they reside in each others error margins. Furthermore, these GPCs appear to be comparable with GPCs reported in literature about ALD SnO_2 growth using TDMASn and O_2 plasma [23,25,83].

4.4 Summary

In this chapter, an overview of the ALD reactor and the proceedings for the deposition of SnO_2 layers is provided, together with a motivation for choosing TDMASn as a precursor and O_2 plasma as a co-reactant for our ALD process. Furthermore, it has been shown how our plasma enhanced ALD recipe has been developed in terms of suitable timestep durations and appropriate gas flow rates, concluded with a final ALD recipe that is able to deliver uniform SnO_2 films. Eventually, the ALD process has been successfully extended to other deposition temperatures: linear growth with similar GPCs at different deposition temperatures have been achieved.

Chapter 5

Material Characterizations of Atomic Layer Deposited Tin Oxide

In this chapter, results of an extensive characterization of atomic layer deposited SnO_2 layers are presented in order to elucidate their material properties as a function of the deposition temperature. The outcomes are provided in the categories chemical composition, structural and morphological, electrical, optical and energy level characterizations. Additionally, a more detailed section is devoted to the results from electrochemical impedance spectroscopy measurements.

5.1 Chemical Composition Characterization

To investigate the elemental composition of the atomic layer deposited SnO_2, first XPS surveys have been recorded for the deposition temperature range under investigation: see Figure B.1 in Appendix B for two examples. These surveys have clarified that mainly the elements tin, oxygen, carbon and nitrogen should be further examined. Therefore, scans have been performed around the most explicitly present binding energies of these elements, after having sputtered away surface contamination present due to air exposure. The results of these scans on all SnO_2 layers are shown in Figure 5.1.

As can be seen, Sn and O are clearly present in all SnO_2 layers, while the contributions from C and N decrease for increasing deposition temperature to negligible levels. By comparing the peak areas according to the indicated fitting procedure, relative elemental concentrations have been calculated: see Table 5.1. From this table, it can be clearly observed that surface contamination of mainly C is removed after one sputtering step.

Table 5.1: *Relative elemental composition of SnO_2 layers of $\sim$ 30 nm thick, deposited at various temperatures. Obtained from peak fitting XPS data before and after one sputtering step, which was applied to remove surface contamination.*

Temperature T	**Relative concentration before sputtering step**				**Relative concentration after sputtering step**			
	C1s	**N1s**	**O1s**	**Sn3d**	**C1s**	**N1s**	**O1s**	**Sn3d**
°C	at.%				at.%			
50	15.5 ± 0.5	6.6 ± 0.2	55 ± 2	22 ± 1	6.0 ± 0.6	5.9 ± 0.8	56 ± 2	33 ± 2
100	9.5 ± 0.8	2.8 ± 0.3	60 ± 2	28 ± 3	3.5 ± 0.6	2.2 ± 0.5	59 ± 3	35 ± 2
150	5 ± 4	0.5 ± 0.1	61 ± 2	33 ± 6	-	-	60 ± 3	38 ± 4
200	7.3 ± 0.1	-	61 ± 2	30 ± 2	-	-	62 ± 3	38 ± 3

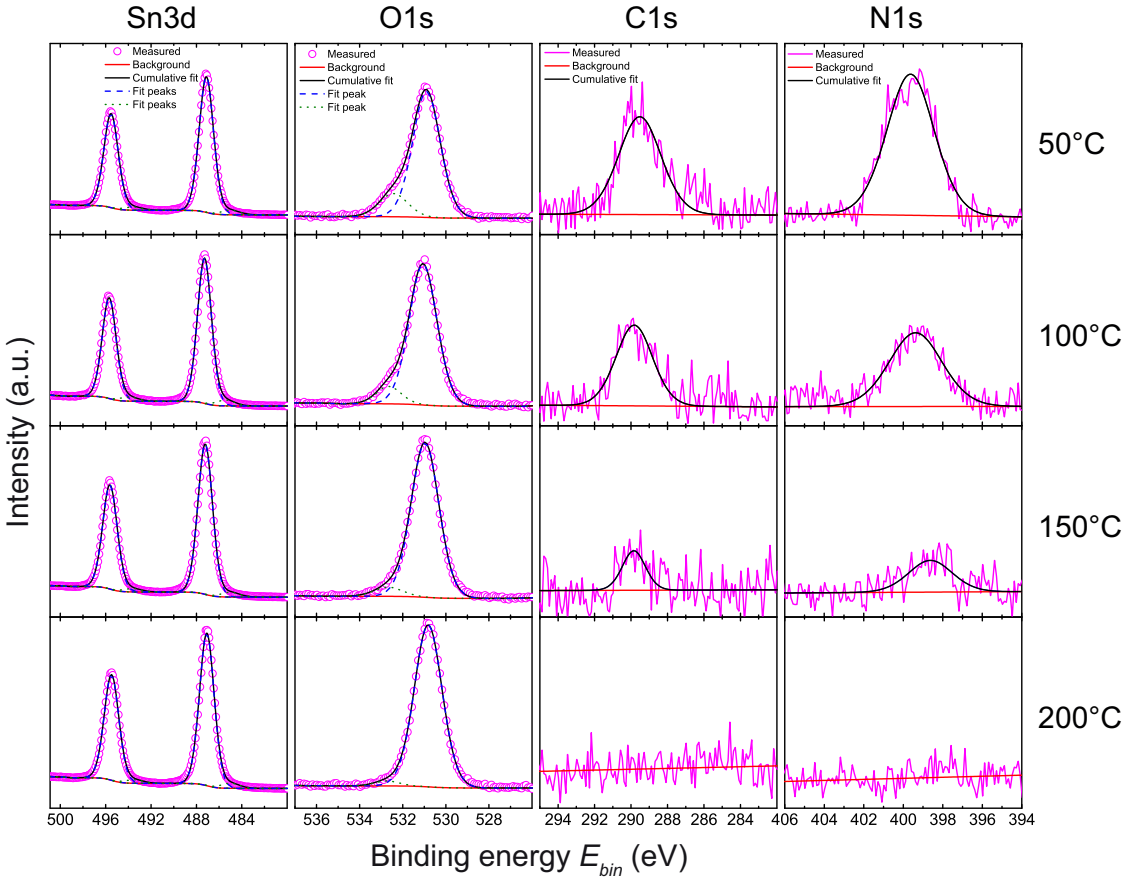

Figure 5.1: *XPS scans after one sputtering step around the binding energies of Sn3d, O1s, C1s and N1s for SnO_2 layers of ∼ 30 nm thick, deposited at various temperatures. Across the measured data, the adopted fitting procedure has been indicated. N.B.: the intensity scales are different per examined element.*

Apart from the presence of elements, also information about their oxidation state and covalent bonding can be derived. As can be seen in Figure 5.1, the Sn peaks appear at 495.6 eV and 487.0 eV. Since the Sn3d peaks of Sn^{2+} (for SnO) and Sn^{4+} (for SnO_2) practically overlap, valence band spectra are necessary to define the oxidation state of the Sn [84, 85]. Figure B.2 in Appendix B depicts the valence band spectra of SnO_2 layers deposited at various temperatures, measured by XPS. From these valence band spectra, it is obvious that the characteristic Sn5s peak of SnO that should appear between 2.5 and 3 eV is negligible in our SnO_2 layers, which means that these layers mainly contain SnO_2-bonds [84].

Assessing the O scans in Figure 5.1 for 50°C and 100°C especially, it is evident that the data consist of more than only the O1s peak at 530.9 eV that originates from the SnO_2 bonds [85]. Around 532.5 eV another contribution is visible, which could be assigned to OH-groups, nitrates, and/or bonds with C [86,87]. Then, the C1s binding energy at 289.5 eV is probably related to a carbonate or a C=O bond [86,87], and the N1s binding energy at 395.0 - 395.5 eV may hint towards a bond with C [86, 87]. All these observations for the O, C and N binding energies could be related to an incomplete surface ligand removal during the ALD process at 50°C and 100°C. These deposition temperatures could be too low for a sufficient reactivity of the O_2 plasma, contrary to deposition temperatures of 150°C and 200°C that both have negligible C and N contents. Additionally, the OH-

groups may be explained by chemisorbed and/or hydroxylated oxygen species, or by the settlement of ALD reactor background H_2O in the material. After all, these impurities have been observed and similarly explained earlier for ALD of SnO_2 at relatively low deposition temperatures [76, 78, 79].

Finally, in order to check whether the evaluated chemical composition is homogeneous in film thickness, a sputtering procedure has been executed to determine depth profiles for SnO_2 layers of $\sim$ 30 nm thick deposited at all temperatures: see Figure 5.2. From

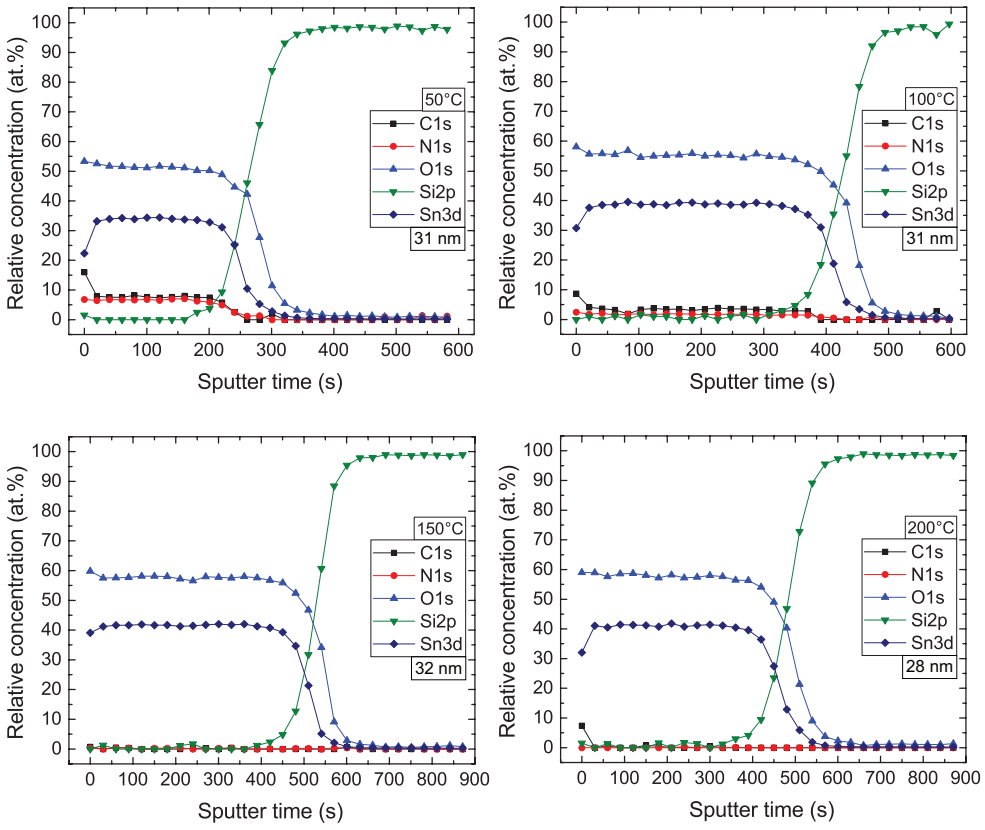

Figure 5.2: *XPS depth profiles of SnO_2 layers of $\sim$ 30 nm thick, deposited at various temperatures. The relative concentration is given as a function of the sputtering time, which serves as an indication of the measurement depth. Here, the silicon (Si2p) signal has been considered as well, to count for the substrate material. A higher relative concentration of C at 0 s sputter time is due to surface contamination from ambient air.*

these depth profiles, it is clear that the film compositions are uniform throughout the layer thickness for all SnO_2 layers deposited at different temperatures. Furthermore, it can be seen that the higher the deposition temperature, the longer is the sputtering time required to reach the silicon substrate. This indicates that the SnO_2 layers deposited at higher temperatures have a higher mass density.

Subsequently, to confirm the XPS results and gain knowledge about the hydrogen content that is undetectable by XPS, the SnO_2 layers have been more accurately characterized via RBS and ERD measurements. See Table 5.2 for the processed results, containing the mass density and the relative elemental concentrations per SnO_2 layer deposition temperature. From the refractive index and the mass density, it can be seen that indeed the

Table 5.2: *Mass density and relative elemental concentration of SnO_2 films deposited at different temperatures from RBS and ERD measurements, combined with their thicknesses and refractive indices from SE measurements (via Cauchy and Tauc Lorentz models, respectively). The RBS and ERD results have been corrected for the native SiO_2 layer on the c-Si substrate. Measurement accuracies: 7% for H, 4% for O, and 2% for Sn.*

Temperature T	**Thickness d**	**Refractive index n**	**Mass density ρ**	**Relative concentration**		
				H	**O**	**Sn**
°C	nm	*(at 1.96eV)*	g/cm^3	at.%		
50	31	1.75	4.10	20.2	56.8	23.0
100	29	1.86	5.16	12.9	60.2	26.9
150	29	1.95	5.17	7.7	61.6	30.7
200	36	2.00	6.14	3.8	64.7	31.5

densities of the SnO_2 layers increase for increasing deposition temperatures, in agreement with literature [76,78]. For SnO_2 deposited at 200°C, the value even approaches the mass density of stoichiometric SnO_2 (6.9 - 7.0 g/cm^3, [76, 88, 89]). Moreover, the presence of OH-groups observed by XPS is confirmed by the large concentration of H in the SnO_2 layers deposited at 50°C and 100°C. Surprisingly, presence of C and N expected from XPS results could not be certified by these RBS measurements, probably because their concentrations are below the detection limits of the system.

5.2 Structural and Morphological Characterization

In order to explore any crystallinity of the ALD SnO_2 layers, XRD characterizations have been performed. Figure 5.3a shows XRD spectra of SnO_2 layers deposited at various temperatures on c-Si substrates.

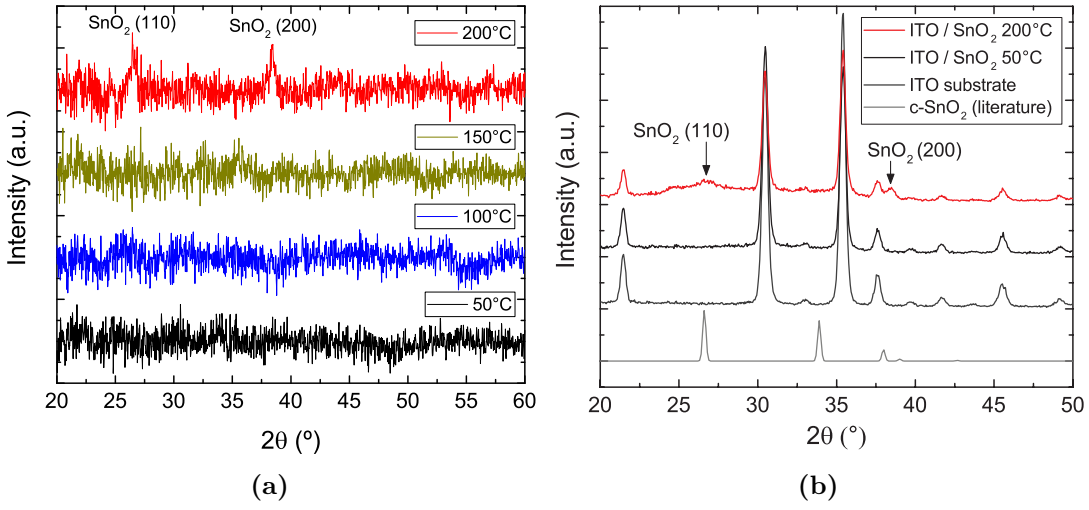

Figure 5.3: *(a) XRD spectra of SnO_2 layers of ∼ 30 nm thick, deposited at various temperatures on crystalline silicon (c-Si) substrates. (b) GI-XRD spectra of SnO_2 layers of ∼ 30 nm thick, deposited at 50°C and 200°C on glass/ITO substrates. As references, XRD patterns of a bare glass/ITO substrate and of crystalline SnO_2 from literature (JCPDF 41.1445, [90]) have been included.*

From these spectra, significant SnO_2 crystalline peaks of lattice planes (110) and (200) can be observed for the SnO_2 film deposited at 200°C. Still, the intensities of these peaks are quite low, which indicates that the SnO_2 deposited at 200°C consists of a small number of crystallites with different orientations. The SnO_2 layers deposited at lower temperatures are found amorphous, in agreement with literature [77–79].

Additionally, to examine whether the SnO_2 layers grow similarly on our glass substrates with ITO (used for the production of PSCs), two SnO_2 layers have been deposited at 50°C and 200°C on glass/ITO substrates. To further investigate the crystallinity in more detail, GI-XRD measurements have been executed. See Figure 5.3b for the GI-XRD spectra on these samples, together with a reference for a bare glass with ITO layer, and the crystalline SnO_2 patterns from literature. Indeed, these plots exhibit similar amorphous and crystalline behavior as observed for SnO_2 deposited on c-Si at 50°C and 200°C, respectively.

TEM has been carried out to corroborate the XRD findings. Figure 5.4 shows an overview of TEM-images for SnO_2 layers deposited at 50°C and 200°C. In subfigures (a)

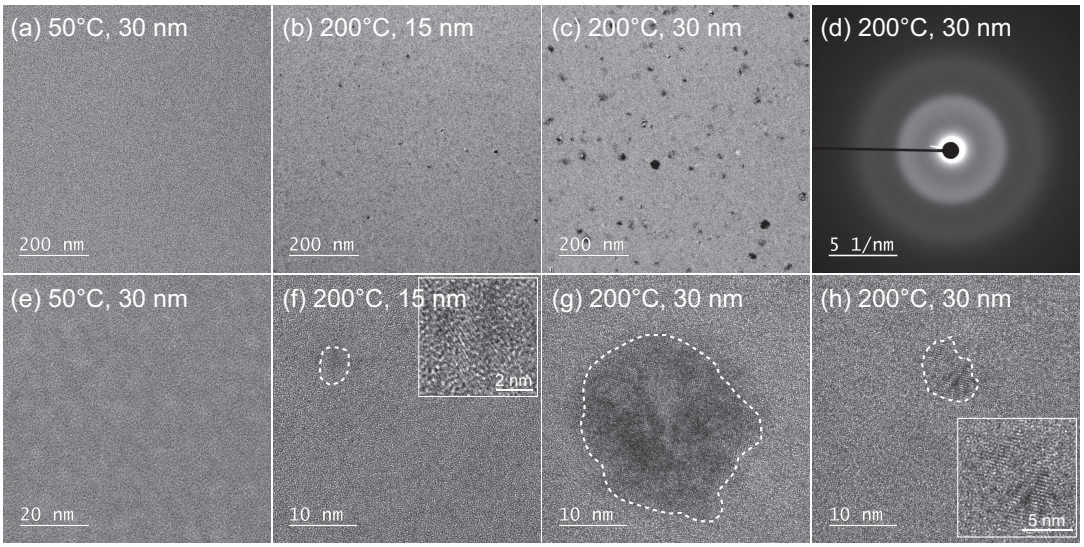

Figure 5.4: *TEM top view images of SnO_2 layers deposited on TEM-windows at 50˚C and 200˚C. (a) and (e) show the top view of a SnO_2 layer of 30 nm thick deposited at 50˚C, with low and high magnifications. (b), (f), (c), (g), and (h) show the top view of SnO_2 layers of 15 nm and 30 nm thick deposited on TEM-windows at 200˚C, with low and high magnifications. The dotted lines in the zoomed pictures indicate crystallites. (d) provides an electron diffraction pattern of a SnO_2 layer of 30 nm thick deposited at 200˚C.*

and (e), TEM images of SnO_2 layers of 30 nm deposited at 50°C are presented, in which no crystal structures are observed. In contrast, subfigures (b) and (f) of the SnO_2 layer of 15 nm thick deposited at 200°C contain a few small dark spots of $\sim$ 4 - 5 nm width. As this layer is grown thicker to 30 nm, more and larger dark spots appear in the images, see subfigure (c). For instance, zoomed-in images show a spot of $\sim$ 25 nm width (subfigure (g)) and a spot of $\sim$ 7 - 8 nm (subfigure (h)). This analysis confirms that SnO_2 layers deposited at 200°C have small crystallites. The size and the site density of these crystallites both develop as the layer thickness increases. Nevertheless, it should be mentioned that the major fraction of this film is still amorphous, as confirmed by the electron diffraction pattern depicted in subfigure (d).

5.3 Electrical Characterization

To investigate the electrical properties of the SnO_2 layers, the carrier density N_e, Hall mobility μ_{Hall} and resistivity ρ have been determined by means of Hall measurements; see Table 5.3. The SnO_2 layers deposited at 50°C and 100°C appeared to be very resistive, most

Table 5.3: *Results from Hall measurements on SnO_2 layers deposited at various temperatures on c-Si substrates with ∼ 450 nm SiO_2 as a resistive substrate layer. Thickness obtained via SE measurements.*

Temperature T	**Thickness** d	**Carrier density** N_e	**Mobility** μ_{Hall}	**Resistivity** ρ
°C	nm	10^{19} cm^{-3}	cm^2/V·s	10^{-3} Ω·cm
50	(32.6 ± 0.6)	-	-	-
100	(30.4 ± 0.4)	-	-	-
150	(32.3 ± 0.1)	(6.5 ± 1.0)	(9.2 ± 1.0)	(10.7 ± 0.3)
200	(18.4 ± 0.2)	(9.6 ± 0.5)	(36 ± 1)	(1.8 ± 0.1)
	(33.0 ± 0.5)	(8.4 ± 0.2)	(34.6 ± 0.6)	(2.1 ± 0.1)

certainly due to their porous/amorphous phase [61, 78, 79]. As the deposition temperature increases, the layers become conductive, which is in agreement with the changes in material structures discussed earlier in this chapter. Eventually, comparable trends and quantities for N_e, μ_{Hall} and ρ have been obtained in literature on ALD SnO_2 [76, 78].

5.4 Optical and Energy Level Characterization

5.4.1 Optical Characterization

One of the requirements for SnO_2 as an ETL in an n-i-p PSC is a high transparency for the visible light spectrum. Therefore, the absorption coefficient α has been determined from the extinction coefficient k. This k has been obtained from SE measurements on SnO_2 layers for all deposition temperatures, by fitting the SE data with a Tauc-Lorentz model. See Figure 5.5a for the calculated α against the photon energy $h\nu$.

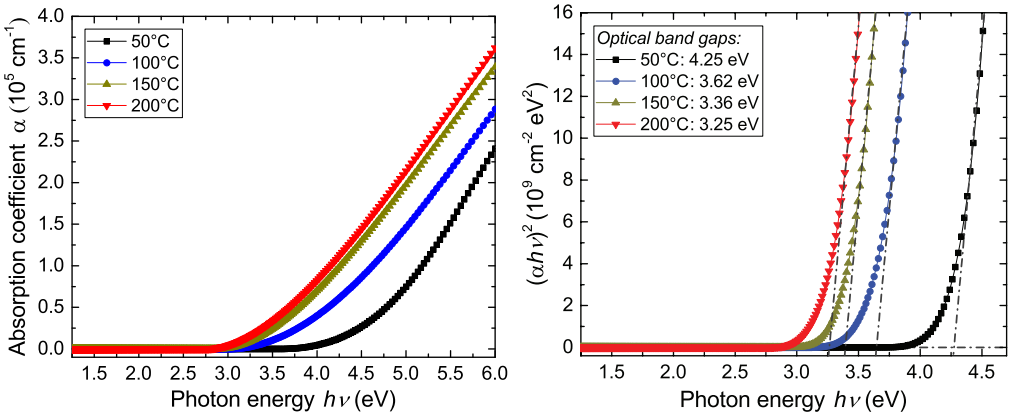

(a) **(b)**

Figure 5.5: *Absorption coefficient α (a), and $(\alpha h\nu)^2$ (b) as a function of the photon energy $h\nu$ for SnO_2 layers of ∼ 30 nm thick, deposited at different temperatures. Obtained from fitting SE measurement data with a Tauc-Lorentz model.*

As can be seen, all SnO_2 layers deposited at different temperatures are transparent for the full visible light spectrum, although the optical band gap appears to decrease for SnO_2 deposited at increasing temperatures. To determine the exact optical band gap of the SnO_2 layers, Tauc plots ($(\alpha h\nu)^2$ against $h\nu$) have been composed, as can be seen in Figure 5.5b. Hereby, it has been assumed that the SnO_2 layers have a direct optical band gap, such as reported elsewhere [49, 79, 91]. The values for the optical band gaps have been obtained from the $h\nu$ value where a linear extrapolation through the steep increase of $(\alpha h\nu)^2$ reaches zero absorption, as shown in the legend. The values range between 4.25 eV for SnO_2 deposited at 50°C to 3.25 eV for SnO_2 deposited at 200°C. This development has been observed in literature on ALD of SnO_2, and it has been attributed to an evolution from a solely amorphous phase to a nanocrystalline phase for increasing deposition temperatures [77, 78].

To validate the information about the transparency, UV-VIS-NIR spectroscopy measurements have been executed. The results are reported in Figure 5.6. These data confirm

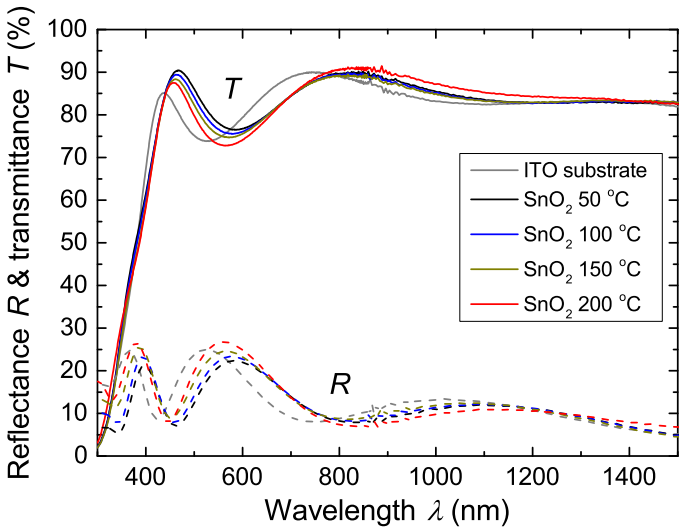

Figure 5.6: *Reflectance and transmittance spectra for SnO_2 layers of ∼ 30 nm deposited at various temperatures on glass substrates with ∼ 200 nm ITO. As a reference, the spectrum for a bare glass/ITO substrate has been included. Measured by UV-VIS-NIR spectroscopy.*

the high transparency of all SnO_2 layers; with respect to the glass/ITO substrate, no significant extra absorption is detected.

5.4.2 Energy Level Characterization

Next to the determination of the optical band gaps, the impact of the SnO_2 deposition temperature on the specific energy levels of the SnO_2 has been investigated. From UPS measurements, the work function (WF) values and valence band maximum (VBM) values have been determined by examining the binding energy value for which a linear extrapolation through the intensity data at the intensity offset intersects the background signal. This has been performed for SnO_2 layers deposited at 50°C and 200°C in order to sketch the energy band structure for the two most extreme case studies. See Figure 5.7 for the results of the measurements on the work function and valence band maximum values.

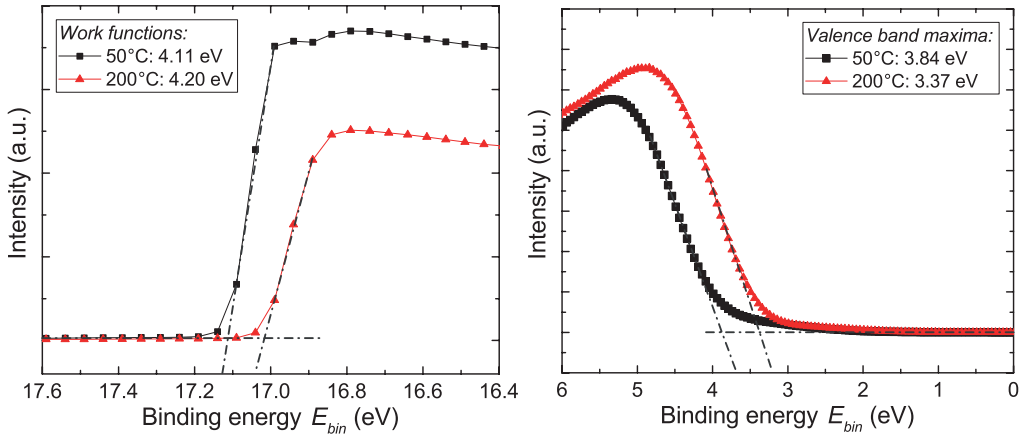

Figure 5.7: *UPS spectra to determine the work function (left) and valence band maximum (right) values for SnO_2 layers of 15 nm thick deposited at 50°C and 200°C on c-Si substrates. The legends present the obtained quantities. N.B.: for these measurements, the Fermi level has been calibrated at 0 eV.*

As can be seen, the calculated work function values for SnO_2 deposited at 50°C and 200°C are 4.11 eV and 4.20 eV, respectively, and the valence band maximum values are 3.84 eV and 3.37 eV, respectively. The valence band maximum values and their mutual difference are very comparable with the values extracted from XPS valence band spectra, as presented in Figure B.2 in Appendix B. Additionally, the work function values fall within a reasonably comparable range of 4.1 - 4.7 eV of those described in other literature on ALD SnO_2 [22, 23, 92]. Hereby, it should be remarked that both deposition conditions and surface modification or contamination are probably the main factors for differences between the values reported here and in literature. Besides, no clear energy states appear to be present within the band gap between the Fermi level (E_F) and the valence band maximum for SnO_2 layers deposited at both 50°C and 200°C, as shown in the UPS valence band maximum spectra.

These values collected via UPS can be used to sketch the energy band diagram for SnO_2 deposited at 50°C and 200°C: see Figure 5.8. Here, also the ionization potential (IP) has been calculated and reported, and the optical band gap has been used to position the conduction band (CB) minimum. The Fermi level for the SnO_2 film deposited at 200°C appears to be located within the CB: this suggests that the material is degenerate, as has been reported in literature before [61,93]. This would as well explain the high conductivity as shown in Section 5.3.

Furthermore, it has been confirmed that the work function and the valence band maximum values of the examined SnO_2 layers are independent on both the substrate (c-Si and glass/ITO) and an O_2 plasma treatment[1] performed before the UPS measurement. This indicates that the values obtained here can be used later on when the energy band structure at the the SnO_2/perovskite interface is investigated.

[1] RF power: 600 W, 1 mbar, 2.5 min.

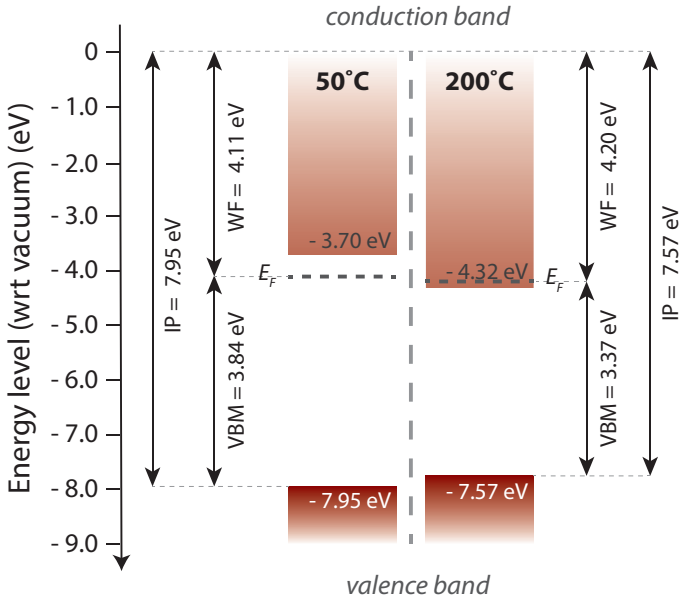

Figure 5.8: *Energy band diagrams for SnO_2 deposited at 50˚C and 200˚C, constituted with work function and valence band maximum values determined via UPS measurements. N.B.: for the position of the conduction band minimum, the optical band gap obtained from SE measurements has been used (see Figure 5.5b).*

5.5 Electrochemical Impedance Spectroscopy Characterizations

In addition to the characterizations described earlier in this chapter, EIS has been adopted to qualitatively describe the SnO_2 - electrolyte solution system via equivalent electrical circuits. Furthermore, quantitative information has been obtained in terms of doping density and accordingly, the energy level distance between the material's CB minimum and E_F.

Before characterizing ALD SnO_2 layers, first the bare glass substrates with only FTO have been investigated in order to validate this measurement technique. Appendix C provides the followed procedure and the results from this validation, concluding that the applied EIS technique functions well. Subsequently, measurements have been performed on SnO_2 layers deposited at 200°C and 50°C. Given the fact that these two cases appeared to require significantly different data processing and interpretation, their results and discussions are presented separately.

5.5.1 Results & Discussion on SnO_2 Deposited at 200°C

According to the raw measurement data[2], the simple Randles circuit as shown in Figure 3.9 could be applied to fit the data. Furthermore, this holds that the physical interpretation of the interface is equal to the one elaborated in Section 3.5.3. Subsequently, the capacitances have been calculated with Equation 3.16 using the fitted values, and they have been plotted in a (C^{-2}, V) plot as presented in Figure 5.9.

Per sample, the data behavior has been approximated by a linear fit from the onset of the steep curve on. By using Equations 3.12, 3.14 and 3.13, the doping density N_D and

[2]Example Figures 3.8 and 3.10 are Bode modulus and phase plots, respectively, of a SnO_2 layer of 15 nm thick deposited at 200°C.

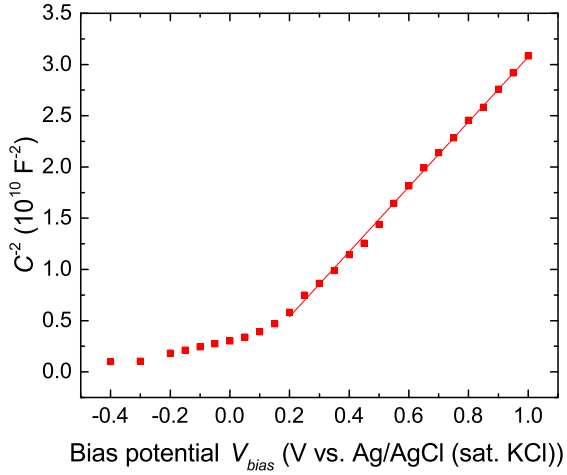

Figure 5.9: *A (C^{-2}, V) plot of a glass/FTO substrate with a SnO_2 layer of 30 nm thick deposited at 200°C, measured by EIS. The data has been fitted using a simple Randles circuit, and finally the capacitance has been determined for various bias potentials.*

the energy level distance between the CB minimum and the Fermi level $E_C - E_F$ have been calculated. Here, the following general and SnO_2 specific input values have been utilized: $\varepsilon_0 = 8.85 \cdot 10^{-12}$ F/m, $\varepsilon_{r,\,SnO_2} = 10$ [61], $A = 8.66 \cdot 10^{-5}$ m^2, $e = 1.60 \cdot 10^{-19}$ C, $k = 1.38 \cdot 10^{-23}$ m^2 kg s^{-2} K^{-1}, $T = 293$ K, $m_e = 9.11 \cdot 10^{-31}$ kg, $m^*_{SnO_2} = 0.3$ [61], $h = 6.63 \cdot 10^{-34}$ m^2 kg s^{-1}. From these input values, $N_C = 3.98 \cdot 10^{18}$ cm^{-3} has been calculated for the benefit of Equation 3.13. See Table 5.4 for the final results of all examined samples, from different SnO_2 deposition batches and with varying thicknesses.

Table 5.4: *N_D and $E_C - E_F$ results from Mott-Schottky calculations on EIS data for five characterized glass/FTO substrates with a SnO_2 layer deposited at 200°C. The samples have been deposited in two batches, with two different SnO_2 layer thicknesses. As a reference, the results for the two characterized bare glass substrates with FTO (see Appendix C) have been included.*

Sample no.	**Thickness** d	**Doping density** N_D	$E_C - E_F$
	nm	cm^{-3}	eV
1.1	15	$(1.12 \pm 0.03) \cdot 10^{21}$	- 0.14
1.2	15	$(1.09 \pm 0.01) \cdot 10^{21}$	- 0.14
1.3	30	$(1.17 \pm 0.04) \cdot 10^{21}$	- 0.14
2.1	15	$(5.7 \pm 0.7) \cdot 10^{20}$	- 0.13
2.2	30	$(5.93 \pm 0.06) \cdot 10^{20}$	- 0.13
FTO.1		$(6.5 \pm 0.3) \cdot 10^{20}$	- 0.13
FTO.2		$(1.14 \pm 0.06) \cdot 10^{21}$	- 0.15

In general, the doping densities are comparable with values reported by Kavan *et al.* (2017) for ALD SnO_2: for as deposited SnO_2 (at 118°C), they found $N_D = 1.5 \cdot 10^{21}$ cm^{-3}, and for the same SnO_2 layer after calcination at 450°C, they found $N_D = 1.0 \cdot 10^{21}$ cm^{-3} [61]. Furthermore, from the results one can conclude that the thickness of the SnO_2 layer within the investigated range does not affect the results. However, a different SnO_2 deposition batch apparently does have an influence, since the values for N_D are almost a factor of 2 smaller. Though, this has a small effect on the calculated values for

$E_C - E_F$. Still, for both SnO_2 batches E_F appears to reside within the CB, which holds that the SnO_2 layers deposited at 200°C are degenerate semiconducting materials. This confirms the suggestion about the position of E_F within the CB, postulated in the previous section, and it corresponds to the electrical conductivity obtained by Hall measurements (see Section 5.3). Moreover, the results seem comparable with the results achieved for FTO layers. A same order of degeneracy and a similar doping density have been measured for both materials, although for the ALD SnO_2 deposited at 200°C it is still unclear what could be responsible for this doping. In literature, it has been suggested that donor-type intrinsic defects from tin interstitials, oxygen vacancies or hydrogen dopants could be responsible for the doping [93–95], but it would require further research to confirm these doping mechanisms for our material.

Looking back on the energy band diagram for SnO_2 deposited at 200°C as depicted in Figure 5.8, now it can be constructed without using the optical band gap. This has been performed in Figure 5.10. As can be observed in the figure as well, the band gap between

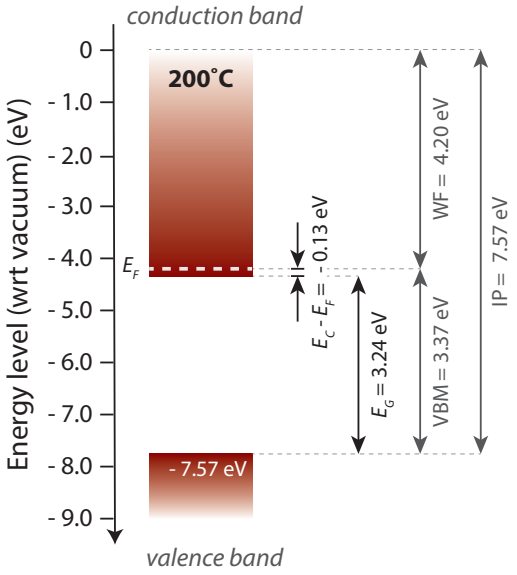

Figure 5.10: *Energy band diagram for SnO_2 deposited at 200˚C, constituted with work function and valence band maximum values determined from UPS measurements, and the difference between conduction band and Fermi level from EIS measurements.*

the valence band and conduction band appears to be 3.24 eV: approximately the same as the optical band gap of 3.25 eV as determined by SE in Section 5.4.

5.5.2 Results & Discussion on SnO_2 Deposited at 50°C

According to the raw measurement data on SnO_2 layers deposited at 50°C, the simple Randles circuit as shown in Figure 3.9 could not be applied to fit the data. Moreover, data fitting appeared to be too challenging with even more complex and extended electrical circuits. Therefore, a qualitative data analysis is described in this section in order to derive material properties. This analysis has been performed along the theoretical background described in Section 3.5.3.

Discussion 1: Porosity

First, the SnO_2 layers deposited at 50°C are considered to be porous, with at least pores large enough for the electrolyte to penetrate. This was already concluded from the SE and RBS/ERD analyses (see Table 5.2), and it is further confirmed by the next analysis of the raw EIS data:

A. It appears that the contact between the sample and the electrolyte solution needs to stabilize still after the start of a measurement, which has not been detected in measurements on SnO_2 layers deposited at 200°C (see Figure 3.8). Presumably, this is caused by the solution that is still penetrating the material pores. This need for stabilization can be observed from the next aspects:

- In the Bode modulus plot shown in Figure 5.11, the first frequency scan at a bias voltage V_{bias} of 0.70 V [3] on a SnO_2 layer of 15 nm thick has a higher $|Z|$ in the high frequency region compared to the subsequent frequency scans at lower V_{bias} (A). This means that the series resistance R_s has been higher for the first measurement, probably because the contact between the sample and the solution had not been completely constituted yet, since the solution still had to penetrate into the pores. Similarly, in Figure 5.12 the Bode modulus plot of measurements on a SnO_2 layer of 30 nm thick is shown, in which it can be seen that the duration of even a few frequency scans has been necessary to lose the noise in $|Z|$ in the high frequency region (A). This could be expected, since a thicker layer may contain deeper pores and could thus require more time to stabilize the sample - solution contact. Besides, it has been confirmed that this behavior is independent of V_{bias} applied at the start of the measurement. Measurements have been performed with a higher starting value for V_{bias}, which have delivered a similar behavior.

- Beside the noise in the high frequency range during the measurements at the first values for V_{bias}, it can be seen in Figure 5.11 that the values of $|Z|$ at the high frequencies (which are approximately R_s) are different for a few frequency scans (B). This effect becomes even larger for measurements on a thicker SnO_2 layer (30 nm) as shown in Figure 5.12 (B), which probably suggests that the contact between the sample and the solution is still being established during the filling of pores. According to Perrotta (2016), this effect can even last for several hours dependent on the pore dimensions [63], which could be an explanation for the strong and prolonged effect observed here.

- Furthermore, noisy data have been obtained for measurements at the first values of V_{bias} when different delay times have been applied between the constitution of the sample - solution contact and the start of the measurement. Figure 5.13 shows Bode modulus plots of EIS measurements on a SnO_2 layer of 10 nm thick, (a) after 5 min delay time and (b) after 20 min delay time. It may be clear that a longer delay time, thus a longer time for the solution to penetrate into the pores, has provided less noisy data in the high frequency region (C).

B. Compared to the data of SnO_2 layers deposited at 200°C (see Figures 3.8 and 3.10), the capacitive behavior of SnO_2 layers deposited at 50°C deviates from ideal performance, and porosity is probably the main factor causing such non-ideal performance [96]. This can be observed from the following aspects:

[3] Concerning the EIS results: every unit V is actually "V vs. Ag/AgCl (sat. KCl)".

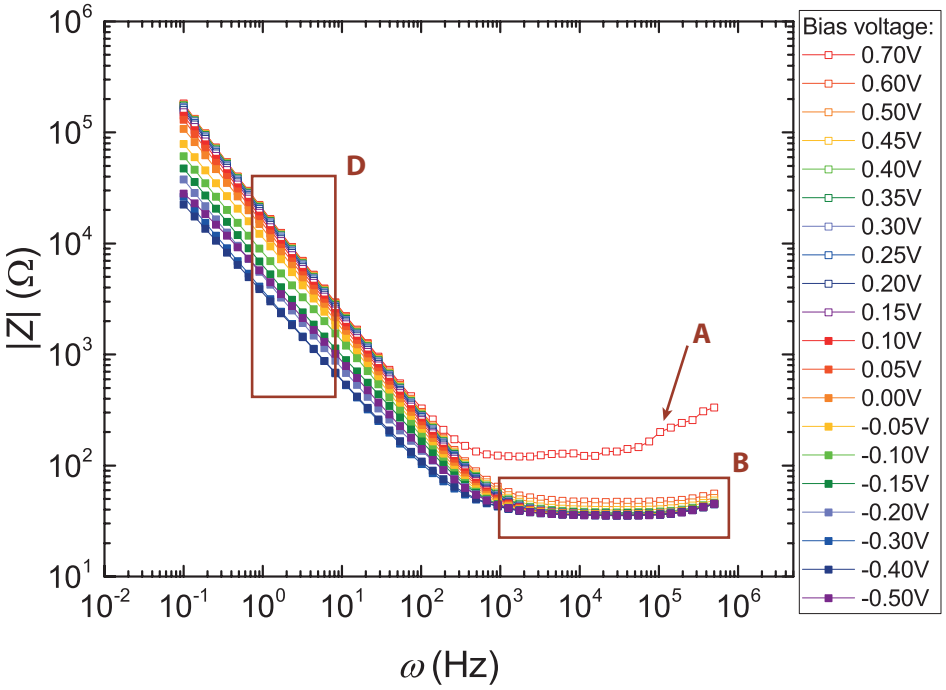

Figure 5.11: *Bode **modulus** plot of EIS measurements on a SnO_2 layer of **15 nm** thick, deposited at 50˚C. Frequency scans have been sequentially performed for every indicated V_{bias} from 0.70 V to - 0.50 V. In the plot, specific data has been indicated, to which is referred in the main text.*

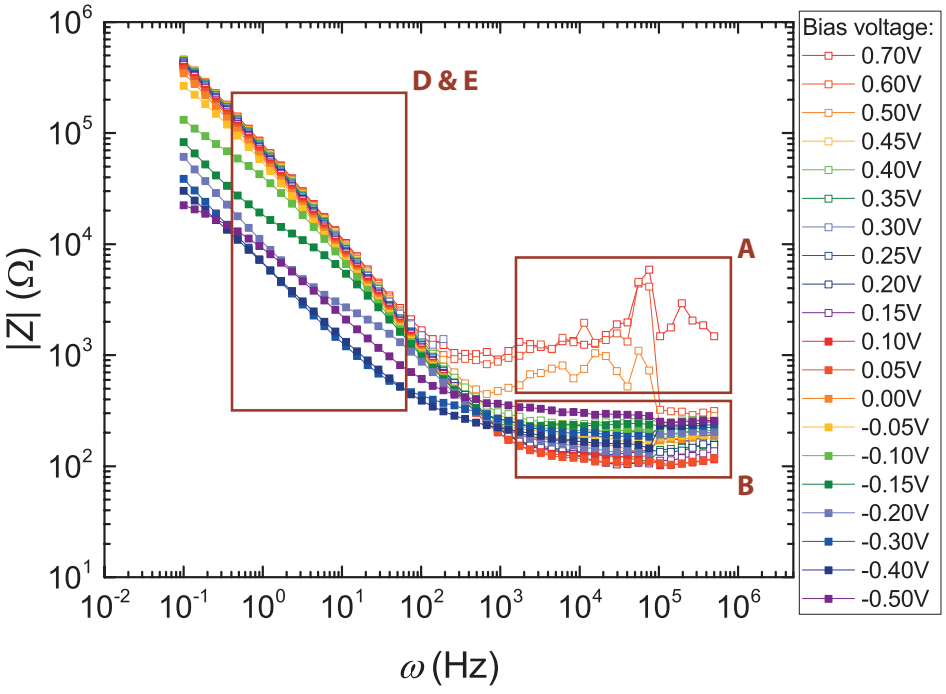

Figure 5.12: *Bode **modulus** plot of EIS measurements on a SnO_2 layer of **30 nm** thick, deposited at 50˚C. Frequency scans have been sequentially performed for every indicated V_{bias} from 0.70 V to - 0.50 V. In the plot, specific data has been indicated, to which is referred in the main text.*

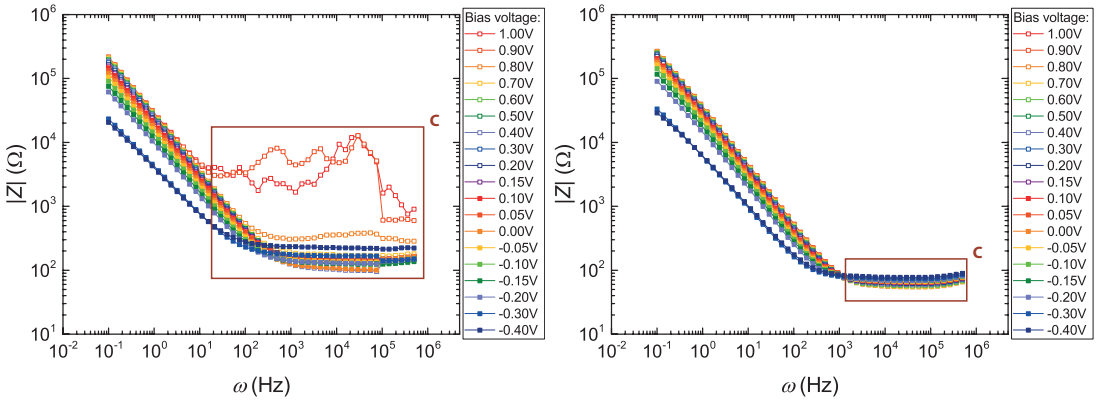

(a) *Delay time: 5 min.* **(b)** *Delay time: 20 min.*

Figure 5.13: *Bode modulus plots of EIS measurements on two different SnO_2 layers of 10 nm thick deposited at 50˚C, both with a different delay time between the constitution of the sample - solution contact and the start of the measurement. In the plots, specific data has been indicated, to which is referred in the main text.*

- In Figure 5.11, the slope of the capacitive part of the data decreases faster for decreasing V_{bias} (D) compared to its 200°C counterpart. Thus, the capacitance non-ideality factor n decreases faster for the SnO_2 deposited at 50°C as V_{bias} decreases. This indicates that this SnO_2 layer is more inhomogeneous in thickness or composition, or that it is porous [97]. Since the first explanation can be disregarded based on the chemical analysis reported earlier, porosity is expected to be the cause. Furthermore, the decrease in n is even larger for the thicker SnO_2 layer (30 nm) deposited at 50°C, see Figure 5.12 (D), which holds that the thicker SnO_2 layer possesses a higher content of porosity.

- Particularly for the SnO_2 layer of 30 nm thick, the measurement data reach a maximum phase angle of only - 80°, as can be seen in the Bode phase plot in Figure 5.14 (D). This $-\varphi$ is lower than the maximum phase angle obtained for SnO_2 deposited at 200°C (see Figure 3.10 (G)). This additionally implies that the SnO_2 layer deposited at 50°C has a less ideal capacitive behavior, and that it is thus presumably porous.

C. The capacitive part of the EIS data of the SnO_2 layer deposited at 50°C seems to contain multiple different contributions, which is not applicable for the SnO_2 deposited at 200°C. Probably, pores of different dimensions each contribute differently to the total EIS data, instead of a uniform layer that contributes as a whole to the EIS data [63, 96, 98]. This can be inferred by the following considerations:

- Multiple peaks can be observed in the low/mediate frequency region (that represents the capacitive part) for some V_{bias} in the Bode phase plot for data of 15 nm SnO_2 deposited at 50°C (Figure 5.15) (E). For a uniform layer, normally only one phase peak represents the capacitive part of the layer, but apparently for this layer multiple contributions add up to the total capacitance. The latter becomes even more evident in Figure 5.14 (E), which presents the impedance phase data of a thicker SnO_2 layer (30 nm).

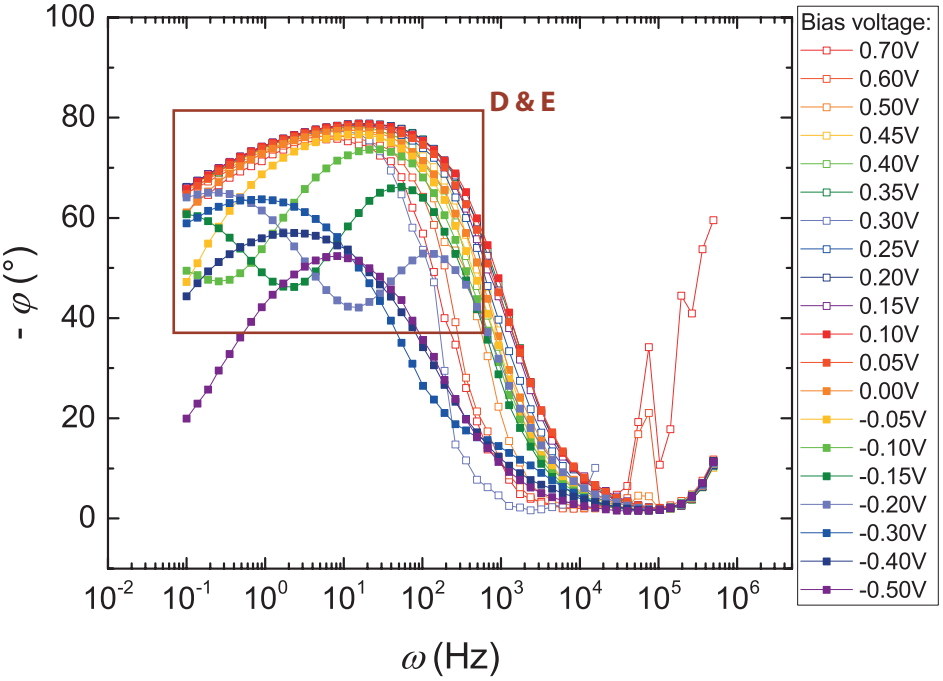

Figure 5.14: *Bode **phase** plot of EIS measurements on a SnO_2 layer of **30 nm** thick, deposited at 50°C. Frequency scans have been sequentially performed for every indicated V_{bias} from 0.70 V to - 0.50 V. In the plot, specific data has been indicated, to which is referred in the main text.*

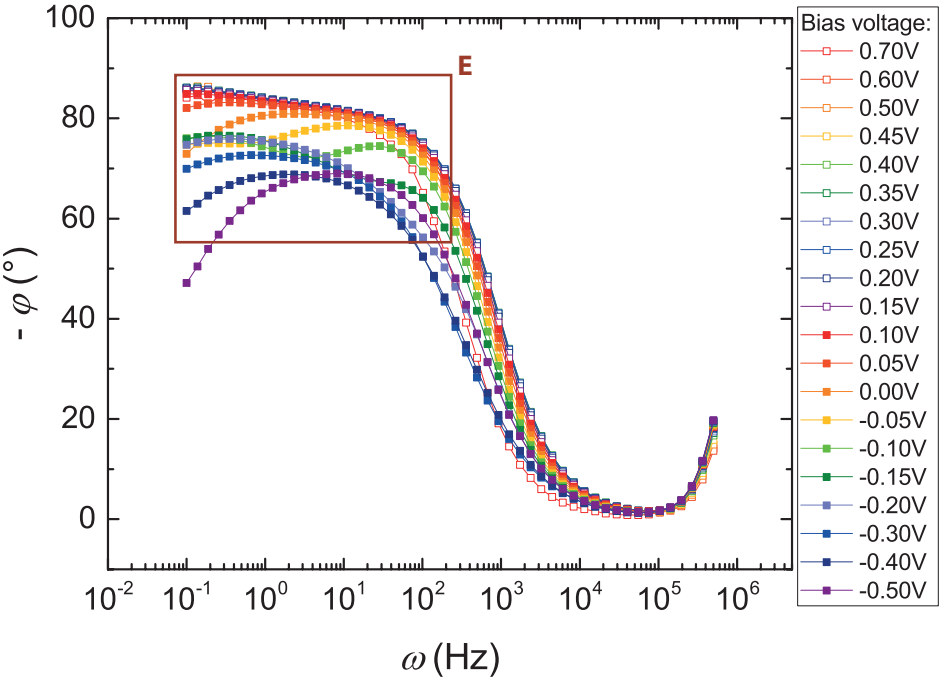

Figure 5.15: *Bode **phase** plot of EIS measurements on a SnO_2 layer of **15 nm** thick, deposited at 50°C. Frequency scans have been sequentially performed for every indicated V_{bias} from 0.70 V to - 0.50 V. In the plot, specific data has been indicated, to which is referred in the main text.*

- Moreover, in the low/mediate frequency region (that represents the capacitive part), different slopes can be observed in the data for some V_{bias} in the Bode modulus plot for data of 30 nm SnO_2 deposited at 50°C: see in Figure 5.12) (E). This also implies that multiple contributions with different values for n build up the capacitive part of the data.

Discussion 2: Resistivity

Second, it has been found that the SnO_2 layers deposited at 50°C are electrically more resistive than the SnO_2 layers deposited at 200°C. This can be inferred by the following observations.

As mentioned in Section 3.5.3, the value for R_p represents the resistance that charges experience as they cross the SnO_2 layer. Values for R_p have been determined for the SnO_2 layers deposited at 200°C at V_{bias} , since the EIS data of those samples could be fitted using the simple Randles circuit. As an example, values of R_p for a SnO_2 layer of 30 nm thick deposited at 200°C are presented in Table 5.5 for a few V_{bias}. The V_{bias} between -0.15 V and 0.15 V have been chosen around the flat-band potential of the material. The other two bias potentials have been included as an extra comparison.

Table 5.5: *Parallel resistances R_p from the EIS data of a SnO_2 layer of 30 nm thick deposited at 200˚C, fitted using the simple Randles circuit.*

Bias potential V_{bias}	**Parallel resistance** R_p
V vs. Ag/AgCl (sat. KCl)	MΩ
0.45	1.82
0.30	1.31
0.15	0.816
0.00	0.605
-0.15	0.320

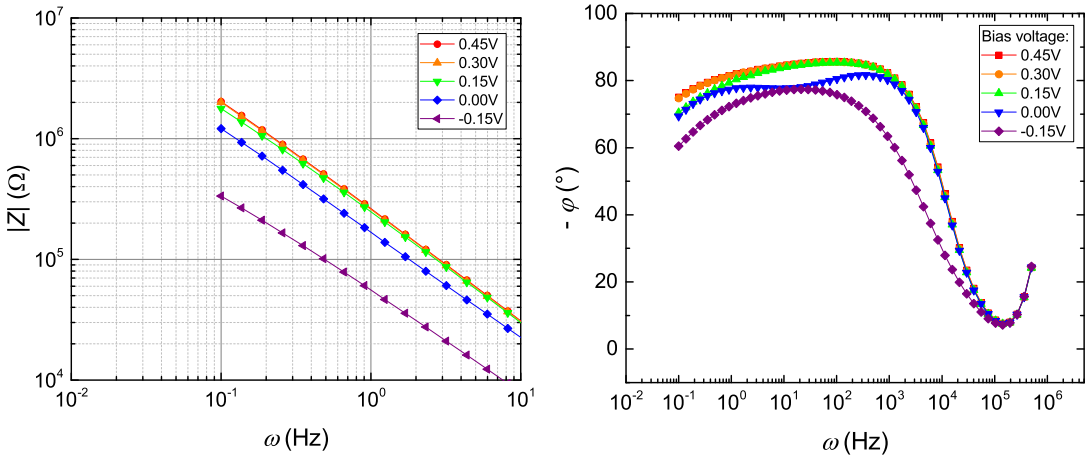

(a) *Bode modulus plot.* **(b)** *Bode phase plot.*

Figure 5.16: *Bode modulus and phase plots of EIS measurements on a SnO_2 layer of 30 nm thick deposited at 50˚C.*

These values for R_p can be compared with the raw EIS data for a SnO_2 layer of 30 nm thick deposited at 50°C at the same values for V_{bias}, see Figure 5.16. As can be seen

in this Figure 5.16a, the $|Z|$ data given in the Bode modulus plot at 10^{-1} Hz have a similar or higher $|Z|$ value compared to the values of R_p of SnO_2 deposited at 200°C at the same values for V_{bias}, as given in Table 5.5. However, since the Bode phase plots belonging to these data (Figure 5.16b) indicate that at 10^{-1} Hz the impedance is still predominantly capacitive (the phase is between - 80° and - 60°), $|Z|$ will keep increasing for a certain frequency range before it becomes constant as it reaches resistive behavior again. Therefore, the final $|Z|$ of SnO_2 deposited at 50°C would arrive at a much higher R_p than the values of R_p for SnO_2 deposited at 200°C, as given in the table.[4] This signifies that the SnO_2 layer deposited at 50°C is relatively much more resistive, which is consistent with the Hall measurements on these amorphous layers.

5.6 Summary

In this chapter, we have presented an extensive variety of characterizations on ALD SnO_2 deposited in the temperature range of 50°C to 200°C. An overview of the revealed material properties is given here:

- In general, tin(IV)oxide has been deposited with a high homogeneity in film thickness. Furthermore, all SnO_2 layers are transparent for the visible light spectrum.
- Carbon ((6.0 ± 0.6) at.%) and nitrogen ((5.9 ± 0.8) at.%) impurities and OH-groups are present in SnO_2 layers deposited at 50°C.[5] The concentrations of these impurities significantly decrease for an increasing deposition temperature. Finally, for the SnO_2 film deposited at 200°C, no carbon and nitrogen impurities have been detected within the detection limits.
- A porous and fully amorphous SnO_2 layer has been grown at 50°C ($\rho_{\text{mass}} = 4.10$ g/cm^3). The SnO_2 layer becomes denser as the deposition temperature increases to 100°C and 150°C, until it reaches a mass density ($\rho_{\text{mass}} = 6.10$ g/cm^3) at a deposition temperature of 200°C that is close to the theoretical SnO_2 bulk mass density ($\rho_{\text{mass}} = 6.9 - 7.0$ g/cm^3). Furthermore, the SnO_2 layer deposited at 200°C consists of an amorphous matrix with nano-crystallites, which grow in site density and size as the layer thickness increases.
- A large electrical resistivity has been obtained for layers deposited at 50°C and 100°C. This resistivity decreases for increasing deposition temperatures towards an electrically conductive SnO_2 film deposited at 200°C ($N_e = (8.4 \pm 0.2) \cdot 10^{20}$ cm^{-3}, $\mu_{Hall} = (34.6 \pm 0.6)$ cm^2/V·s, $\rho_{el} = (2.1 \pm 0.1) \cdot 10^{-3}$ Ω·cm).
- The optical band gap decreases (from 4.25 eV to 3.25 eV) as the SnO_2 deposition temperature increases from 50°C to 200°C. Furthermore, a work function of 4.11 eV and an ionization potential of 7.95 eV have been determined for SnO_2 deposited at 50°C, and a work function of 4.20 eV and an ionization potential of 7.57 eV have been demonstrated for SnO_2 deposited at 200°C. Combined with the optical band gap of 3.25 eV, the SnO_2 deposited at 200°C is characterized to be degenerate semiconducting material.

[4] The only solution to investigate the real R_p of the SnO_2 deposited at 50°C would be to measure until very low frequencies, for instance, until or beyond the mHz range. However, practically this would yield a very prolonged measurement if one measured for this range of low frequencies and for a range of V_{bias}. In addition, it should be taken into account that during these prolonged measurements environmental circumstances can influence the measurement, such that it should also be verified whether the system remains stable in this meantime.

[5] Relative concentrations given for carbon and nitrogen have been measured after one sputtering step.

Chapter 6

Optoelectronic Performance and Interface Characterizations of Perovskite Solar Cells

After an extensive characterization of the atomic layer deposited SnO_2 layers, these have been applied as electron transport layers in perovskite solar cells. This chapter describes the performances that have been achieved for these cells, together with a discussion of the possible causes for the differences in the results. This discussion is supported by characterizations on both the perovskite itself, as well as on its interface with the SnO_2 layers. Finally, a literature comparison of the reported performances for PSCs with ALD SnO_2 is provided.

6.1 Fabrication and Performance Characterization of Perovskite Solar Cells

In this chapter, results are presented for PSCs with SnO_2 layers deposited at a relatively low temperature of 50°C, and at a proportionately high temperature of 200°C. Due to a wrap-around deposition effect inherent to ALD, the conductive SnO_2 layers caused shunting problems in PSCs produced at the start of this research. Special measures have been taken to resolve these practical issues, though due to limited resources it has been chosen to focus only on PSCs with the SnO_2 layers having the largest mutual difference in material properties. Given the importance of this shunting issue for further research, a detailed description about it is provided in Appendix D.

Hence, PSCs have been fabricated according to the procedure described in Section 3.6.1. Figure 6.1 shows SEM, HAADF-STEM and TEM cross-sectional images of these PSCs. The layer stack intended for our PSC design is confirmed by Figures 6.1a and 6.1b. Large perovskite grains of a few hundred nanometers in the lateral direction are visible in Figure 6.1a. Figure 6.1b evidently shows the SnO_2 layer deposited at 50°C, between the ITO and the perovskite. Finally, via Figure 6.1c the amorphous phase of SnO_2 deposited at 50°C can be distinguished, since it possesses no pattern such as the adjacent crystalline ITO and perovskite layers.

To determine the performance of the manufactured PSCs, J-V measurements have been performed. Figure 6.2 presents J-V curves of the best performing PSCs, with SnO_2 layers deposited at either 50°C or 200°C (referred to as 50°C SnO_2 and 200°C SnO_2, respectively). It can be seen that both PSC types exhibit quite large J-V hysteresis

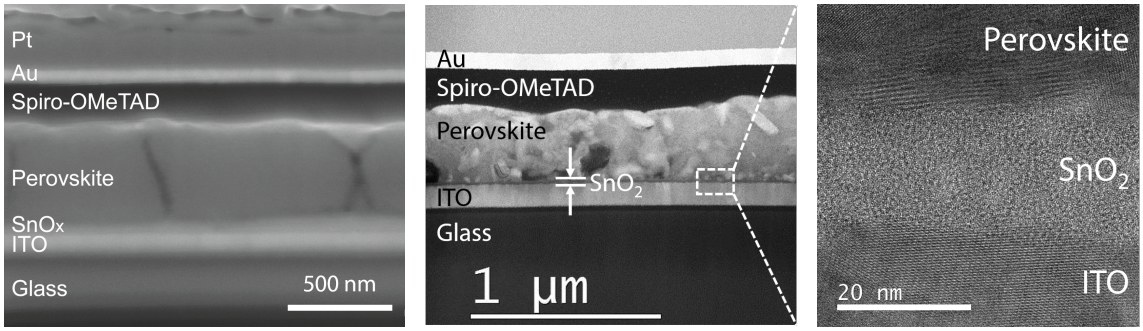

(a) **(b)** **(c)**

Figure 6.1: *Cross-sectional images of our perovskite solar cell with a SnO_2 layer deposited at 50°C, obtained via SEM (a) and HAADF-STEM (b). A high resolution TEM image of the SnO_2 layer is provided in (c).*

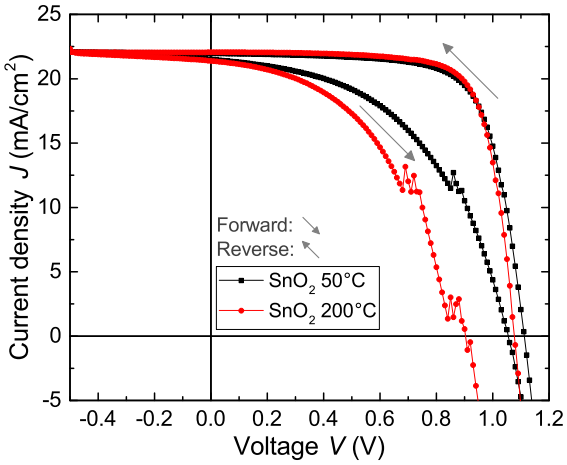

Figure 6.2: *Reverse and forward J-V scans of the best performing PSCs with ETLs of SnO_2 deposited at either 50°C or 200°C. Scan rate: 200 mV/s, stepwise: 10 mV. The wrinkles in the forward scans are due to a measurement set-up bug.*

behavior, as reported earlier in literature (see Section 2.1.2), also in the case of PSCs with ALD SnO_2 [23–25]. For instance, Wang *et al.* (2016) showed a significant hysteresis present in the J-V results for PSCs with ALD SnO_2. They reduced this hysteresis by applying a so-called "C_{60}-SAM[1] interlayer" between the SnO_2 and the perovskite. They reported that the surface defects were passivated by this interlayer, and that the electron transfer between the perovskite and the SnO_2 layer was hereby promoted [24]. In a more recent work of Wang *et al.* (2017), they were able to eliminate the J-V hysteresis almost completely by post-annealing the ALD SnO_2 layer, in addition to applying a C_{60} interlayer. They claimed that this would increase the electron mobility in the SnO_2 and thereby further reduce the imbalance of charge extraction [25]. However, this claim may be doubtful, since they reported no improved results on PSCs with only post-annealed ALD SnO_2 and without a C_{60} interlayer. Next, Hu *et al.* (2017) presented PSCs with ALD SnO_2 that also suffered from J-V hysteresis, and they suggested that it could be dependent on the co-reactant chosen for the SnO_2 ALD process. They found that a PbI_2 interlayer was unintentionally formed between the SnO_2 and the perovskite, which would

[1] C_{60}-SAM: buckminsterfullerene self-assembled monolayer.

establish an energy band alignment dependent on this ALD co-reactant. In case of the SnO_2 layers deposited using ozone, negligible hysteresis was found. Though in case of oxygen plasma or water as a co-reactant, they concluded that the alignment due to the PbI_2 caused electron extraction barriers, which were held responsible for the increased hysteresis [23].

In this work, the observed hysteresis may not be explained by energy band misalignment due to a PbI_2 interlayer. Although PbI_2 presence has been detected in the perovskite of both semi-PSCs with either 50°C SnO_2 or 200°C SnO_2[2], electron extraction at the SnO_2/perovskite interface has appeared to be better for PSCs incorporating 200°C SnO_2 (as shown by PL measurement results later in this chapter) while precisely these PSCs have exhibited a larger hysteresis. Furthermore, it is also improbable that the J-V hysteresis observed for our PSCs has been caused by a rather high ETL resistivity that would induce an imbalanced charge extraction, since the 200°C SnO_2 is much more conductive than our 50°C SnO_2 while the hysteresis is larger for the former.

It is more plausible that the J-V hysteresis of our PSCs has been caused by interface defects. These defects may operate as charge traps, resulting in a dynamic process of trapping and detrapping of charges [99]. However, since the detrapping process may be rather slow, charge extraction can be delayed. Our PSC design contains no specific measures to passivate interface defects with, for instance, a C_{60} interlayer in order to inactivate such trap states. Accordingly, these interface defects may be an explanation for the observed hysteresis. The larger hysteresis for the PSCs with 200°C SnO_2 might then be related to a higher interface defect density. Furthermore, another reasonable origin for an imbalanced charge extraction and thus hysteresis may be ion migration within the perovskite [38, 41]. When the PSC is under illumination, ions may be driven towards the contacts by an internal electric field. However, they cannot be extracted and thus may reside at the interfaces, forming an opposing electric field that reduces the extraction efficiency for electrons and holes. Nevertheless, this may rather be an additional origin for the hysteresis observed in this work, since it is related to the perovskite bulk and can therefore not explain the difference in hysteresis between PSCs with 200°C SnO_2 and 50°C SnO_2.

Apart from the hysteresis, the performances of PSCs with either 50°C SnO_2 or 200°C SnO_2 have been compared. The PCE, V_{OC}, J_{SC}, and FF have been taken from the reverse J-V measurements on a large number of PSCs[3], and the statistical results are given in Figure 6.3. From these statistics, the initial performances of both PSC types appear to be comparable, though on average the J_{SC} and FF are slightly higher for PSCs with 200°C SnO_2. Later on in this chapter, characterizations into the perovskite bulk and the SnO_2/perovskite interface are presented to further investigate these differences.

In addition to the J-V scans, MPP tracking measurements have been performed on both PSC types under a continuous AM1.5G illumination. These results are shown in Figure 6.4. From these results, it can be concluded that the 200°C SnO_2 is preferred for the long-term PSC performance. The PSC with this 200°C SnO_2 layer have shown an approximately constant PCE, while the PSC with an ETL of 50°C SnO_2 experienced a decreasing PCE, until below 8% after 16 hours and even around 4% after 60 hours (results not shown here). The cause for this degradation under continuous illumination remains unclear and is therefore under investigation. One possible explanation could be an instability of the 50°C SnO_2 under UV illumination; the layer might suffer from a UV photon induced degradation comparable to what was found for TiO_2 [53].

[2] PbI_2 presence was detected by XRD, XPS and SEM, see Figures E.1, E.2, and E.3 in Appendix E.
[3] 31 and 13 PSCs with a SnO_2 layer deposited at 50°C and 200°C, respectively.

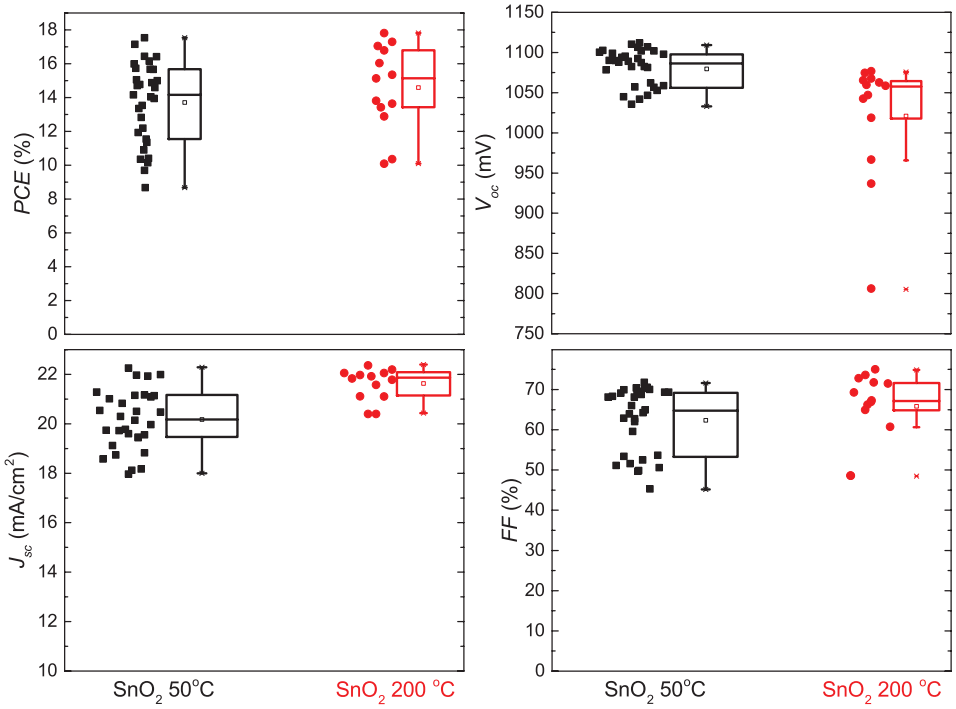

Figure 6.3: *Statistics on the PCE, V_{OC}, J_{SC}, and FF extracted from reverse J-V scans of PSCs, that contain either 15 nm of SnO_2 deposited at 50°C, or 15 nm of SnO_2 deposited at 200°C. Measurement scan rate: 200 mV/s, stepwise: 10 mV.*

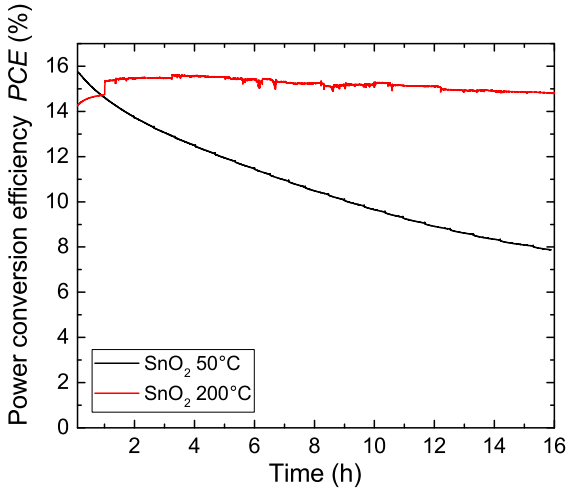

Figure 6.4: *PCEs measured at the maximum power point of PSCs with SnO_2 layers deposited at either 50°C or 200°C, under continuous AM1.5G illumination in an N_2 atmosphere.*

6.2 Bulk and Interface Characterizations on Perovskite Solar Cells

In order to explain the differences in the J_{SC} and FF results, both the perovskite bulk as well as its interface with the SnO_2 ETL have been examined. Possible variations in the first aspect, the perovskite bulk, have been characterized via XRD and XPS to check

whether a similar perovskite layer has been grown on either 50°C SnO_2 or 200°C SnO_2. The results can be found in Figures E.1 and E.2 in Appendix E, respectively.

From these figures, it becomes clear that both the crystal structure and the composition of the two perovskite layers are similar. Though, it should be remarked that the composition measured by XPS only represents the composition within the top $\sim$ 10 nm of the perovskite, thus it could be that the composition is different throughout the layer. Furthermore, when the perovskite grain sizes are compared to each other via SEM top view images (see Figure E.3 in Appendix E), it also confirms that both perovskite crystals exhibit a comparable morphology. In conclusion, it is quite certain that the perovskite has been similarly grown on both SnO_2 layers, which implies that the causes for the performance differences have to be rather attributed to differences between the two types of SnO_2/perovskite interfaces.

To examine the interface between the perovskite layer and the 50°C SnO_2 or 200°C SnO_2 layer, UPS measurements have been executed to determine the energy levels of the perovskite, and PL measurements have been performed in order to check the electron extraction at the SnO_2/perovskite interface.

6.2.1 Energy Level Structure via Ultraviolet Photoelectron Spectroscopy

Figure 6.5 presents the results from UPS measurements on perovskite layers deposited on either 50°C SnO_2 or 200°C SnO_2. The work function values (WF) have been determined at 4.11 eV and 4.21 eV for the perovskites on 50°C SnO_2 and 200°C SnO_2, respectively.[4] These values are quite comparable to values reported elsewhere for $(FAPbI_3)_{0.85}$-$(MAPbBr_3)_{0.15}$ [22] and $MAPbI_3$ [23, 49]. Furthermore, by summing the work function and the valence band maximum (VBM) values, ionization potentials (IP) can be calculated: 5.98 eV and 5.97 eV for the perovskites on 50°C SnO_2 and 200°C SnO_2, respectively. These IP values are slightly larger than the IP values reported, for example, for $MAPbI_3$ (5.66 eV [49]) and for $(FAPbI_3)_{0.85}(MAPbBr_3)_{0.15}$ (5.85 eV [22]). However, larger IP values towards even 6.4 eV have been measured as a certain excess of PbI_2 was incorporated in the film [100]. Since PbI_2 has also been found in our fresh perovskite layers[5], a larger IP therefore seems plausible.

Subsequently, the WF and VBM values of these perovskite layers have been applied to sketch an energy band diagram with energy levels with respect to vacuum, as shown in Figure 6.6. As can be seen, the energy band diagrams of both perovskite layers are very similar. According to the conduction band (CB) minimum alignment between the perovskite and the 50°C SnO_2, electrons may experience an energy barrier (0.69 eV) in an attempt to be extracted from the perovskite. However, given the fair initial J-V performances of PSCs with 50°C SnO_2, this seems unlikely to occur. We suggest that there may be shallow defect energy states within the band gap that assist in extracting electrons. In parallel, the energy band diagram for the PSC with a 200°C SnO_2 layer implies that electrons can be extracted via the CB quite easily. Further on, although the valence band maximum for the 200°C SnO_2 layer is slightly higher than the one for the 50°C SnO_2 layer, it is assumed that both layers successfully block the injection of holes, considering the high V_{OC}s obtained for both PSC types.

[4] These determinations have been performed similarly to the procedure described in Section 5.4.2.
[5] See Figures E.1 and E.3 in Appendix E.

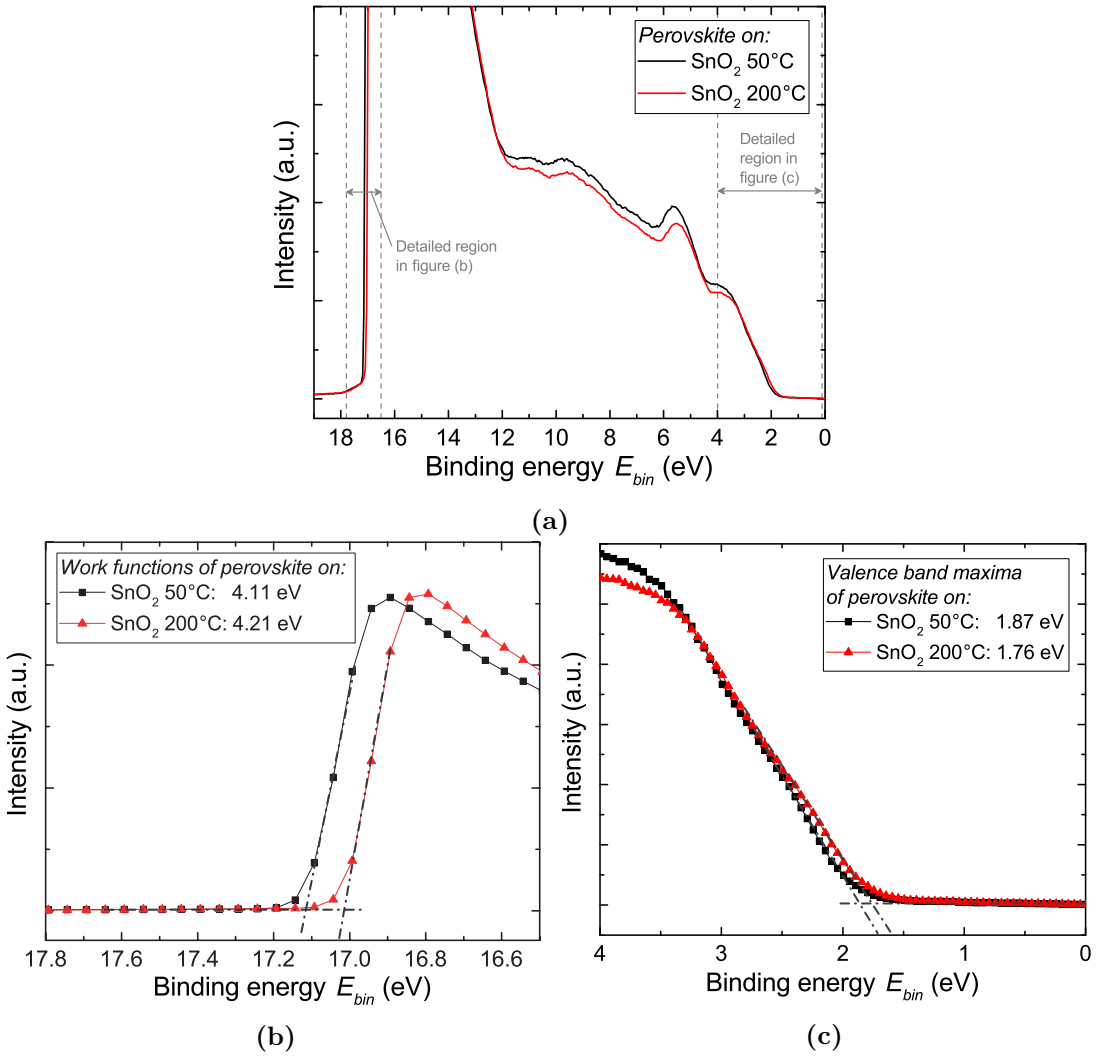

Figure 6.5: *UPS spectra to determine the energy band structures of perovskite crystals grown on 15 nm SnO_2 deposited either at 50°C, or at 200°C. The full UPS spectra are given in (a), with zoomed-in views to determine the work function values (b) and the valence band maximum values (c). The legends present the obtained quantities. N.B.: for these measurements, the Fermi level has been calibrated at 0 eV.*

6.2.2 Electron Extraction Properties via Photoluminescence Spectroscopy

To further investigate the electron transport at the SnO_2/perovskite interface, both steady-state (SS) and time-resolved (TR) PL measurements have been performed. The results are given in Figure 6.7. First, the optical band gap of the perovskite has been determined from Figure 6.7a; PL peaks center at 780 nm, which corresponds to a band gap energy of 1.59 eV. This value is comparable with band gaps reported earlier for multiple cation perovskites [19, 47, 101]. Second, it can be observed in Figure 6.7a that the PL intensity is much lower for a measurement of the perovskite on top of 15 nm 200°C SnO_2. A lower peak intensity, referred to as "PL quenching", indicates that charges are more efficiently extracted from the perovskite into the SnO_2 layer, and thus do not contribute to radiative recombination [2, 24, 102, 103]. Furthermore, this is confirmed by Figure 6.7b, from which it becomes clear that the charge lifetime for the perovskite on top of 200°C SnO_2 decays

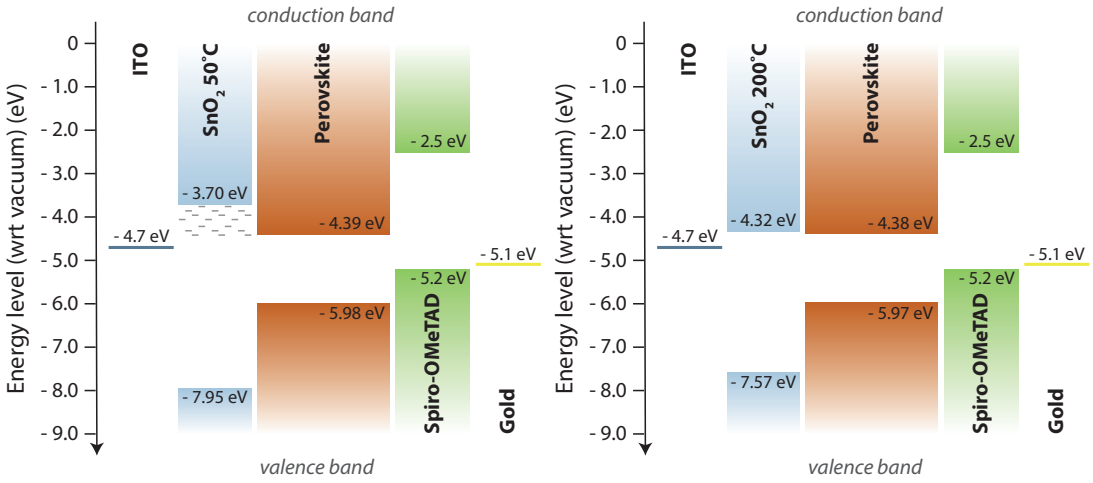

Figure 6.6: *Energy band diagrams for complete PSCs with SnO_2 deposited either at 50°C (a) or at 200°C (b). In the diagram for 50°C SnO_2, shallow defect states have been suggested. Data for the energy levels of the SnO_2 layers have been taken from Section 5.4.2; data for perovskite layers have been determined from UPS and PL measurements (see Figure 6.5 and 6.7); data for spiro-OMeTAD has been taken from literature [56]. N.B.: the energy levels given here are only according to their levels with respect to vacuum, thus no mutual alignment has been taken into account.*

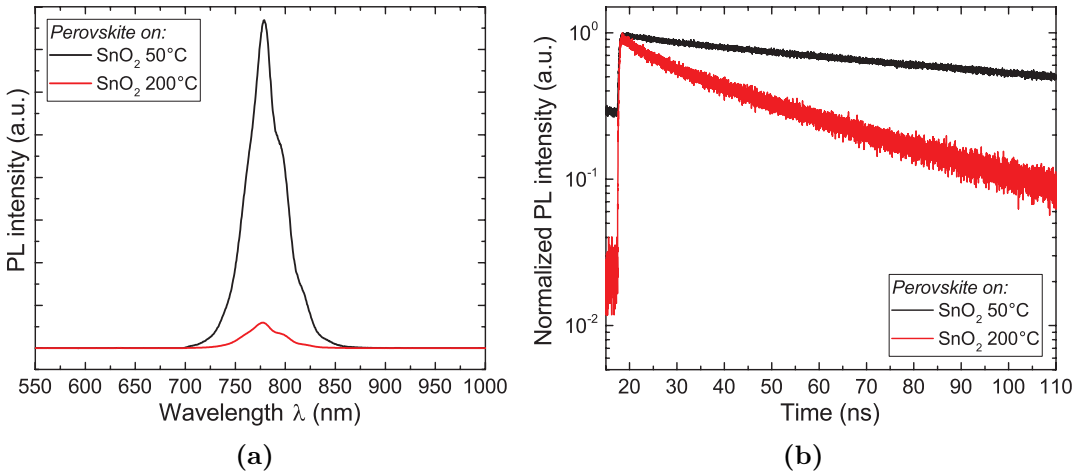

Figure 6.7: *Steady-state (a) and time-resolved (b) photoluminescence spectra of semi-cells (without spiro-OMeTAD and gold) with 15 nm SnO_2 layers deposited either at 50°C or 200°C. The laser beam entered from the SnO_2 side into the perovskite.*

faster [24, 50, 104]. A possible reason for this difference in charge extraction is that the 200°C SnO_2 has a large electrical conductivity, and that the 50°C SnO_2 is highly resistive (as shown via Hall measurements in Section 5.3); an interpretation that has been proposed too by Wang *et al.* (2017) [25]. Accordingly, this difference could be an explanation for the higher J_{SC} and FF for PSCs with 200°C SnO_2.

6.3 Literature Comparison on Perovskite Solar Cell Performances

In Table 6.1, an overview of the J-V results from literature on ALD SnO_2 for PSCs is provided, together with the J-V results obtained in this research. As can be seen, the

Table 6.1: *Overview of literature reporting n-i-p PSCs that incorporate ALD SnO_2 as an ETL. The details of the ALD process (co-reactant and deposition temperature) and cell configuration are given, together with the J_{SC}, V_{OC}, FF, and PCE of their best performing PSC. All ALD processes employed TDMASn as a precursor, and all PSC configurations had a gold electrode on top.*

ALD SnO_2 details	**PSC configuration**	**Dir.**	J_{SC} mA/cm^2	V_{OC} V	FF %	PCE %	**Ref.**
O_3 at 118°C	FTO/SnO_2/$(FAPbI_3)_{0.85}$-$(MAPbBr_3)_{0.15}$/spiro	R	21.3	1.14	74	18.4	[22]
		F	21.2	1.13	75	18.1	
O_2 plasma at 100°C	FTO/SnO_2/$MAPbI_3$/spiro	N/A	21.2	1.07	75.5	17.2	[24]
	FTO/SnO_2/C_{60}-SAM/$MAPbI_3$/spiro		21.4	1.13	79.1	19.0	
	FTO/SnO_2/C_{60}-SAM/ $MAPbI_3$/spiro	R	21.8	1.08	77.0	18.1	
		F	21.8	1.07	75.5	17.6	
O_3 at 100°C	ITO/SnO_2/$MAPbI_3$/ spiro/MoO_3	R	20.5	1.19	67	15.3	[23]
		F	20.3	1.19	68	15.4	
O_2 plasma at 100°C		R	20.5	1.16	63	14.6	
		F	20.3	1.16	61	13.6	
H_2O at 100°C		R	20.9	1.11	59	12.7	
		F	20.4	1.10	48	9.8	
O_2 plasma at 100°C	FTO/SnO_2/ $MA_{0.7}FA_{0.3}PbI_3$/spiro	R	21.7	1.09	73	17.3	[25] **
		F	21.7	1.04	65	14.9	
	FTO/SnO_2*/C_{60}-SAM/ $MA_{0.7}FA_{0.3}PbI_3$/spiro	R	22.4	1.12	79	19.9	
		F	22.4	1.09	77	19.3	
O_2 plasma at 50°C	ITO/SnO_2/triple cation /spiro	R	22.0	1.11	70.1	17.5	TR
		F	21.5	1.06	49.3	11.2	
O_2 plasma at 200°C		R	22.1	1.08	67.3	17.8	
		F	21.4	0.91	43.1	9.1	

Legend: spiro: spiro-OMeTAD. triple cation: $Cs_{0.05}(MA_{0.15}FA_{0.85})_{0.95}Pb(I_{0.9}Br_{0.1})_3$.
Dir.: scan direction. R: reverse scan. F: forward scan. N/A: not available.
*: annealed for 1h at 100°C in ambient air. **: average of multiple PSCs. TR: this research.

(reverse) J-V results of this research are comparable with the highest values reported in literature, although our PSCs still largely suffer from hysteresis. This hysteresis is smaller for other PSCs with ALD SnO_2 (without a passivating interlayer) reported in the presented publications. However, it is well known that J-V hysteresis is scan-rate dependent, and it might be largely reduced at an extremely slow J-V measurement scan rate. Since the results in this table may have been obtained using different scan rates (these were not reported), it might be unfair to compare them.

In addition, from Table 6.1 it is again clear that an interlayer of, for instance, C_{60} between the SnO_2 and the perovskite is beneficial to suppress the hysteresis. Furthermore, other investigations applied FTO instead of ITO as a conductive substrate layer, and/or other perovskite compositions. These differences could have an influence on the J-V parameters and the hysteresis too.

6.4 Summary

In summary, ALD SnO_2 layers deposited at 50°C or 200°C have been successfully implemented as an ETL in our PSCs. Both PSC types have demonstrated a considerable J-V hysteresis and comparable initial performances, although the PSCs with 200°C SnO_2 have exhibited a higher J_{SC} and FF on average. UPS measurements have shown a good hole-blocking ability for both SnO_2 layers, and a presumably non-adverse energy barrier for electrons at the 50°C SnO_2/perovskite interface. A more efficient electron extraction has been characterized by PL measurements at the interface between the 200°C SnO_2 and the perovskite, with respect to the 50°C SnO_2/perovskite interface. Furthermore, a significant degradation on the performance under long-term illumination has been found for PSCs using 50°C SnO_2, whereas up to the investigated period of 16 hours the performance has remained stable for the PSCs with 200°C SnO_2.

Chapter 7

Conclusions and Recommendations

In this research, a large variety of material properties of atomic layer deposited SnO_2 layers has been examined. Hereby, the deposition temperature of the SnO_2 layers has been altered between 50˚C and 200˚C. In particular, electrochemical impedance spectroscopy has been adopted to investigate ultrathin SnO_2 films. Subsequently, the SnO_2 layers deposited at different temperatures have been applied in perovskite solar cells as electron transport layers, in order to correlate the properties of the SnO_2 bulk material and SnO_2/perovskite interface to the overall solar cell performance.

This thesis is completed with conclusions on the research questions related to these topics. Furthermore, a few specific recommendations are provided, which could be used for further investigations into the subjects addressed in this research.

7.1 Conclusions

1. *How are the material properties of atomic layer deposited tin oxide layers affected by the deposition temperature?*

Via atomic layer deposition, tin(IV)oxide layers have been synthesized at deposition temperatures of 50°C, 100°C, 150°C and 200°C. SnO_2 layers deposited at 50°C are amorphous films with significant carbon and nitrogen impurities, and hydroxyl groups. Furthermore, they are porous and therefore have a relatively low mass density of 4.10 g/cm^3. Additionally, the layers exhibit a large electrical resistivity, and are very transparent for the visible light spectrum due to their large optical band gap of 4.25 eV.

The higher the deposition temperature is chosen, the less carbon and nitrogen impurities and hydroxyl groups exist in the films, until negligible levels in the layers deposited at 150°C. The layers stay amorphous for the films grown at 100°C and 150°C, though their mass densities increase. Further on, the optical band gap and the electrical resistivity decrease for an increasing deposition temperature of the SnO_2 layer.

At a deposition temperature of 200°C, a SnO_2 film with a negligible level of impurities is achieved that contains nano-crystallites embedded in an amorphous matrix. Meanwhile, the mass density has increased to 6.10 g/cm^3, which is close to that of 6.95 g/cm^3 for a stoichiometric SnO_2 bulk. Additionally, these layers remain transparent for visible light, although they demonstrate a smaller optical band gap of 3.25 eV, if compared to the SnO_2 deposited at 50°C. Finally, the film has been characterized to be degenerate, which explains the relatively low resistivity of $(1.8 - 2.1) \cdot 10^{-3}$ Ω·cm.

2. *What insights into atomic layer deposited tin oxide properties can be obtained by means of electrochemical impedance spectroscopy?*

In this research, electrochemical impedance spectroscopy has delivered two findings on SnO_2 properties. First, it has been shown that the formation of a tunable Schottky barrier at a metal oxide - electrolyte solution interface causes tunable capacitive behavior, which can eventually be used to calculate the doping density of the metal oxide via the Mott-Schottky equation. Additionally, this quantity can be applied to calculate the energy level difference between the conduction band minimum and the Fermi level, which can be useful to complete an energy band diagram. Second, it has been demonstrated that electrochemical impedance spectroscopy measurements can confirm that a layer is porous.

3. *How do the material and interfacial properties of tin oxide affect the performance of perovskite solar cells?*

Perovskite solar cells with an electron transport layer of SnO_2 deposited at either 50°C or 200°C have demonstrated comparable initial power conversion efficiencies, though with a considerable J-V hysteresis in both types of PSCs. A slightly higher fill factor and short-circuit current have been characterized for the perovskite solar cells with SnO_2 deposited at 200°C, compared to the cells with SnO_2 deposited at 50°C. Presumably, this difference has been caused by a relatively enhanced electron extraction from the perovskite into the SnO_2 layer deposited at 200°C, due to a significantly higher electrical conductivity of this film. Additionally, a fair long-term stability under continuous illumination in an inert atmosphere has been shown for the perovskite solar cells with SnO_2 deposited at 200°C.

7.2 Recommendations

- **Application of Passivation Layers to Address J-V Hysteresis**

In Chapter 6, several causes and measures have been mentioned to explain and solve the J-V hysteresis in PSCs with ALD SnO_2. Since the trapping and detrapping of charges by interface defects seems a reasonably probable cause for the hysteresis observed in our PSCs, passivation layers of, for example, C_{60}-SAM or PCBM[1] will be applied between the SnO_2 and perovskite in order to passivate interface defects. Hereby, the J-V hysteresis should be reduced and the PSC performance would be enhanced.

- **Performances of Perovskite Solar Cells with Various SnO_2 Layer Thicknesses**

To reduce the series resistance for an improved fill factor of the PSCs applying the electrically highly resistive SnO_2 deposited at 50°C, PSCs with various SnO_2 layer thicknesses will be investigated. Special care will be taken to keep the layer conformal for the thinnest layers, in order to prevent shunting pathways between the perovskite and the ITO.

- **Long-term Instability of Perovskite Solar Cells with SnO_2 Layers Deposited at 50°C**

From the preliminary results on the maximum power point (MPP) tracking up to 60 hours, it has been observed that the long-term efficiency largely decreases for PSCs with an ETL of SnO_2 deposited at 50°C. A possible cause could be UV-photon-induced degradation of

[1] PCBM: [6,6]-phenyl-C_{61}-butyric acid methyl ester.

this porous SnO_2, as has been already proposed for PSCs with mesoporous TiO_2 [53]. This possible effect may be detected by applying a UV-filter on top of the PSCs with SnO_2 deposited at 50°C during an MPP-tracking measurement, to evaluate whether their instability will be partly or completely suppressed.

- **Characterization of Perovskite Solar Cells via Impedance Spectroscopy**

In literature, it has been shown that complete PSCs can be characterized by impedance spectroscopy [35, 105–108]. Hereby, further understanding could be achieved about the resistive and capacitive contributions from different solar cell layers and their mutual interfaces. For instance, Juarez-Perez *et al.* (2014) have identified single layer series resistances, recombination resistances, and interfacial capacitive effects, which all have contributed to the insight into J-V measurement results [105]. This specific application of impedance spectroscopy may explain differences between performances of PSCs incorporating various SnO_2 layers.

- **Porosity of SnO_2 Layers Deposited at 50°C**

The porosity observed for SnO_2 layers deposited at 50°C could be further investigated, for example, by adopting other electrolyte solutions during EIS measurements. If these solutions contain ions with different dimensions, it may be evaluated which of these ions can penetrate into the pores, such that the pore dimensions can be investigated. Furthermore, dedicated software could be adopted to process the EIS measurement data, for instance, to fit measurement data of a porous SnO_2 film properly, such that the measurement data can be used to deduce quantitative material properties.

- **Charge Recombination at the SnO_2/Perovskite Interface**

Within this research, one of the unexplored directions has been charge recombination at the SnO_2/perovskite interface. Since this could have an influence on the eventual PSC performances, further understanding of the role of interface defects in charge transport and recombination would be interesting. Investigations may be performed via J-V measurements under different illumination intensities [24, 109], or via impedance spectroscopy (as proposed earlier).

Acknowledgements

This is the very last page I still have to write in order to finalize my thesis, after having written and revised so many other pages. However, this may even be the most important page of my thesis, given the fact that this work would definitely not have been possible without all the support I received during this graduation project.

First of all, I would like to thank Adriana. After my extensive search for a graduation project, you have helped me to find a suitable one that would give me insight in the collaboration with an external research institution, and one that would challenge me given its comprehensive character. Eventually, the latter has demanded much time of me throughout the entire project, both to properly understand all the aspects of this research, and to correctly present them in my output. Probably, it has not been easy to supervise me because sometimes I may have been a headstrong person, so thanks for your patience and persisting help, especially with publishing the NEVAC article and finalizing my project.

Second, of course I really need to thank Yinghuan. You have taught me so much about perovskite solar cells and the available literature, set-ups in the laboratories, dealing with measurement data, et cetera. I have really enjoyed our time together, for instance, when we had "one week of OpAL time" and of course wanted to do too many experiments, or when we had to cycle to and from Solliance. Lastly, in particular I would like to thank you for helping me in writing my thesis, and for revising it very thoroughly (many times).

Third, thanks for your help Valerio (Zardetto) in producing and characterizing the full perovskite solar cells every time. Furthermore, your help for the EIS part of my work has been indispensable: thanks again for explaining me the experimental set-up and proceedings, providing me with suitable substrates, giving me quick feedback via WhatsApp, and discussing the data that was sometimes quite difficult to interpret!

Fourth, I should really be grateful to the entire PMP research group. Without you, I would not have been able to satisfy my need for coffee (sorry Erwin for the high bill). But of course, I also really appreciate the other help I received. Harm, thanks for all the ALD-related discussions. Marcel, Lachlan, Alfredo and Beatriz Barcones Campo, Valerio (di Palma), Saurabh, Christ Weijtens, Pim and Dibya: thanks for the support in terms of TEM-images, PL measurements, SEM-images, cutting and cleaning substrate tutorials, SCAPS simulations, UPS measurements, and discussions, respectively. Thanks Cristian, Caspar, Janneke and Jeroen for your extensive help in the laboratories, and thanks Jeanne and Lianne for all the administrative support.

Lastly, beside all the people that have enabled the graduation project itself, I would undoubtedly like to thank the people that supported me with good advice, recreation, and friendship. In particular, thanks Willemijn, father, mother, Esmée, Scintillatie and de Acht for being there for me during joyful and difficult moments. And furthermore, thanks Berit, Boy, Jochem, Karsten, Marc, Marco, Marlous, Patrick, Remco, Siebe, and Yen Nhi, especially for the coffee breaks and pleasant conversations, eye-opening tips, and playing table tennis.

Appendix A

Basics of Atomic Layer Deposition

A.1 Introduction

Atomic layer deposition (ALD) is a vacuum or low-pressure deposition technique that enables the growth of ultrathin materials, such as metal oxides. Using ALD, the layer thicknesses can be controlled at the Ångstrom level. Unequalled uniformity and excellent conformality can be acquired too, and deposition can happen at relatively low temperatures (< 500°C). Considering these features, ALD overcomes other deposition principles such as sputtering and spin coating [21].

Eventually, these merits enable a vast variety of layers made by ALD, such as: electron and hole transport layers, surface passivation layers, device encapsulation layers, layers with intentional doping, and recombination layers in tandem solar cells [21]. However, the main disadvantages of ALD are that it has a low substrate through-put, and that the nucleation and growth are dependent of the surface to be deposited on.

The theory elaborated in this chapter has been especially based on [28, 110]. Further information about atomic layer deposition in general can be found there.

A.2 Working Principle

During an ALD process, thin films are grown by repeating a so-called "ALD cycle", by which (ideally) one monolayer is deposited. This ALD cycle usually consists of two half-cycles that can be separated from each other by purge steps. In both half-cycles, a substrate is exposed to a certain chemical species, which posses a self-limiting character: the growth stops after the entire original surface has been saturated, which holds that the species do not react with the surface groups of already chemisorbed species. See Figure A.1 for a schematic representation of a full reaction cycle; in this case the growth of SnO_2 is illustrated.

In the first half-cycle, the reaction chamber is filled with a gas, a so-called precursor, that chemisorbs on the substrate at every available surface group. Hereby, it partially releases its ligands (step A). Afterwards, the chamber is purged with an inert gas, in order to remove left-over precursor and reaction products (step B). During the second half-cycle, a co-reactant is admitted to the reaction chamber. This co-reactant removes all ligands of the earlier deposited layer, and leaves new surface groups behind; the same surface groups as the original surface had (step C). Eventually, the remaining co-reactant and reaction products are purged away, again with an inert gas (step D), and one sub-monolayer has

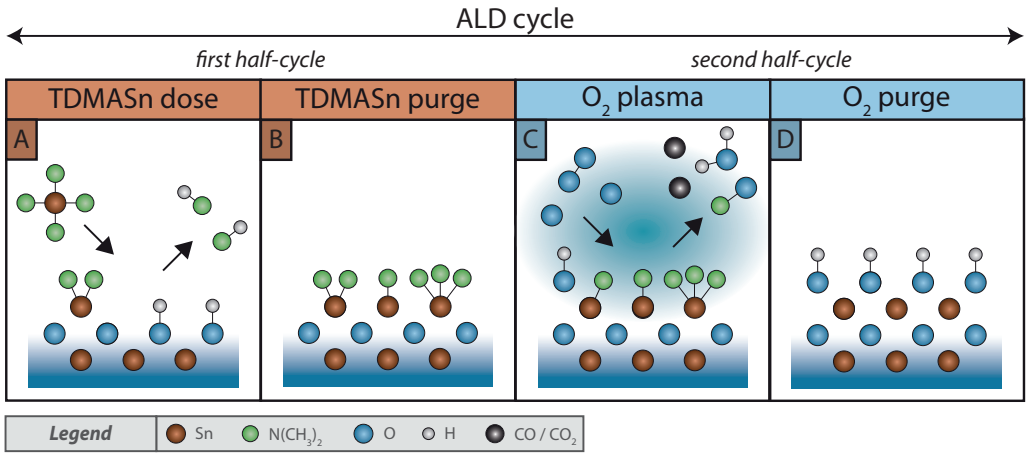

Figure A.1: *Schematic impression of a SnO_2 ALD cycle, divided in two self-limiting half-cycles: one containing the precursor reaction, the other holding the co-reactant step. N.B.: this figure does not aim to represent the precise ALD chemistry. Adapted from [111].*

been deposited. When the growth rate is known, a certain number of cycles can be chosen to obtain a desired thickness.

A.3 Recipe Development

To ensure that an ALD process is controllable and reproducible, certain settings of the so-called "ALD recipe" have to be chosen correctly.

First, precursor and co-reactant have to stay long enough inside the chamber to adequately react with the surface, and to actually obtain full saturated chemisorption at every sample surface location. Though, it is useless to dose precursor or co-reactant too long and thereby provide a surplus. Moreover, both purge step times should be taken sufficiently long to purge the entire chamber, but again: too long purge steps make the process more inefficient. An optimal choice of timesteps can be enabled by producing saturation curves of an ALD process. Hereby, the thickness growth per cycle (GPC) is systematically measured as a function of variable timesteps, in order to find the lowest timestep duration for which the GPC shows no increase anymore. Namely, this implies that growth saturation has been reached.

Second, precursor and co-reactant should be able to reach every substrate position within the designed step time, in order to obtain a fine uniformity. Beside choosing longer timesteps, this can be achieved by creating a suitable gas pressure in the chamber. Therefore, the right flow rates of input gases have to be added to the chamber.

A.4 Application of Plasma

As can be seen in Figure A.1, SnO_2 is grown with TDMASn as a precursor and O_2 plasma as a co-reactant. Originally, ALD processes are executed under high temperatures, such that thermal energy enables surface reactions. This is called thermal ALD. These reactions can, however, also be stimulated by having the energy provided by energetic particles, such as radicals from an oxygen plasma. By applying a plasma as the co-reactant, the technique becomes the so-called Plasma Enhanced Atomic Layer Deposition (PE-ALD).

Advantages of choosing a certain plasma as a co-reactant can be, among other things: improved material properties, lower deposition temperatures, increased growth rate, and reduced purging time. Nevertheless, some disadvantages should also be considered, for example: certain substrate materials are not suitable to be treated with plasma, and it is found that high aspect ratio surfaces are more difficult to be conformally treated.

Appendix B

Additional Figures Material Characterizations of Atomic Layer Deposited Tin Oxide

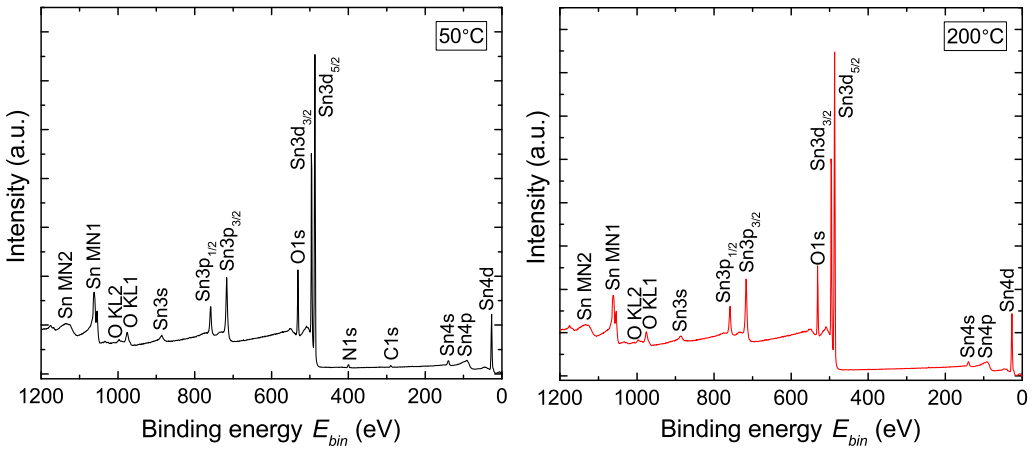

(a) (b)

Figure B.1: *Two examples of XPS surveys over the entire XPS spectrum for SnO_2 layers deposited at 50˚C (a) and 200˚C (b). Mainly, peaks for Sn, O, C and N appear in these surveys.*

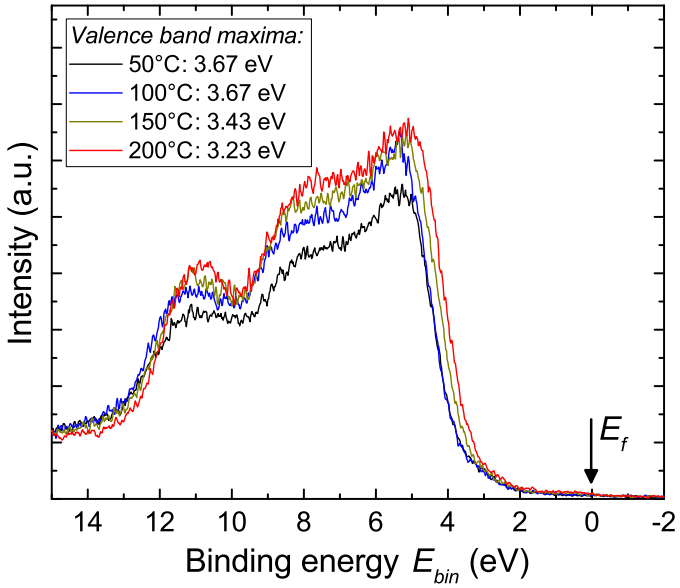

Figure B.2: *XPS valence band spectra for SnO_2 layers deposited at four temperatures. Here, the Fermi level has been calibrated at $E_{bin} = 0$ eV. In the legend, the valence band maxima are provided per SnO_2 deposition temperature.*

Appendix C

Validation of Electrochemical Impedance Spectroscopy Measurements

In order to ratify our EIS measurements, first the bare glass substrates coated with FTO have been investigated. The preparations for the measurement and the measurement itself to characterize the FTO layer have been executed as described in Section 3.5.2. According to the raw measurement data, the simple Randles circuit as shown in Figure 3.9 could be applied to fit the data. Furthermore, this holds that the physical interpretation of the interface is equal to the one elaborated in Section 3.5.3. Subsequently, the capacitances have been calculated with Equation 3.16 using the fitted values, and they have been plotted in a (C^{-2}, V) plot as presented in Figure C.1.

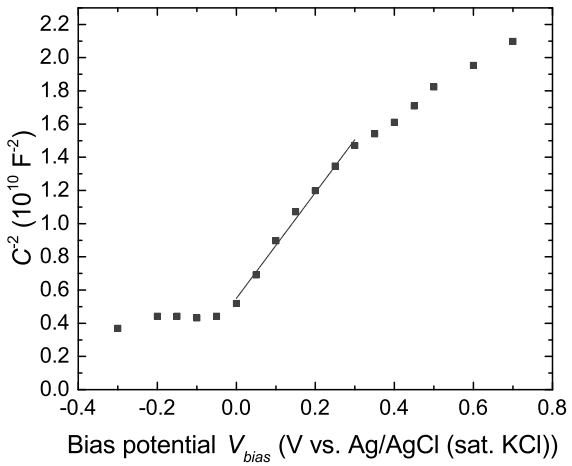

Figure C.1: *A (C^{-2}, V) plot of a bare glass substrate coated with an FTO layer, measured by EIS. The data has been fitted along a simple Randles circuit, and finally the capacitance has been determined for various bias potentials.*

Per sample, the data behavior has been approximated by a linear fit around the onset of the curve. By using Equations 3.12, 3.14 and 3.13, the doping density N_D and the distance between the conduction band minimum and the Fermi level $E_C - E_F$ have been calculated. Here, the following general and FTO specific input values have been utilized: $\varepsilon_0 = 8.85 \cdot 10^{-12}$ F/m, $\varepsilon_{r,\,\mathrm{FTO}} = 9$ [112], $A = 8.66 \cdot 10^{-5}$ m^2, $e = 1.60 \cdot 10^{-19}$ C, $k = 1.38 \cdot 10^{-23}$ m^2 kg s^{-2} K^{-1}, $T = 293$ K, $m_e = 9.11 \cdot 10^{-31}$ kg, $m^*_{\mathrm{FTO}} = 0.27$ [113],

$h = 6.63 \cdot 10^{-34}$ m^2 kg s^{-1}. From these input values, $N_C = 3.40 \cdot 10^{18}$ cm^{-3} has been calculated. See Table C.1 for the final results.

Table C.1: *N_D and $E_C - E_F$ results from Mott-Schottky calculations on EIS data for two characterized bare glass substrates with FTO.*

Sample no.	N_D	$E_C - E_F$
	cm^{-3}	eV
1	$6.55 \cdot 10^{20}$	- 0.13
2	$1.14 \cdot 10^{21}$	- 0.15

As can be seen, the doping density has been determined in the range of 10^{20} - 10^{21} cm^{-3}, which has been reported for FTO in literature before [61, 114, 115]. Furthermore, from these results it can be seen that the Fermi level lies in the conduction band. This implies that the FTO material is degenerate, as may be expected for a transparent conductive oxide. Therefore, this characterization technique has been considered as verified.

Appendix D

Practical Issue of Manufacturing Perovskite Solar Cells

The conductive SnO_2 layers caused shunting problems in the PSCs manufactured at the start of this research. Given the importance of this issue for further research, a detailed description about this practical issue is provided here.

As described in Section 3.6.1, glass substrates with ITO coatings have been deposited with SnO_2 at various deposition temperatures. Schematics of the substrates and the deposition of this SnO_2 layer have been depicted in Figure D.1.

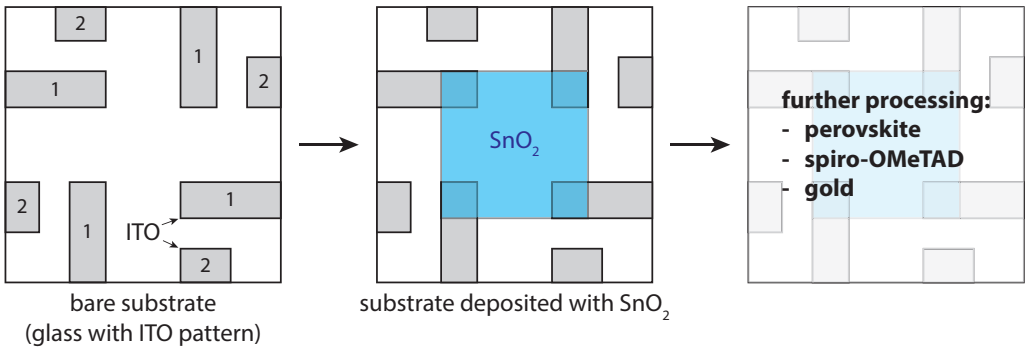

Figure D.1: *Schematic overview of the processing steps for PSC production. A glass substrate with an ITO pattern (left), a substrate with SnO_2 deposited on top (center), further PSC processing steps (right).*

As the PSC is completely composed, the ITO patterns enable the characterization of the PSC at four locations, as if there are four "mini-cells". To this end, the larger ITO strips indicated by no. 1 are applied as TCO front contacts. The smaller ITO strips indicated by no. 2 are used to adhere the gold rear contact.

However, the depicted SnO_2 deposition area in Figure D.1 shows the ideal situation. Figure D.2 shows a realistic schematic of the SnO_2 deposited area, together with the area that was covered by a stainless steel shadow mask during the SnO_2 deposition. SnO_2 was deposited not only at the ITO strips labeled as no. 1, but also at the ITO-free glass region between the ITO strips and even partly on the ITO strips labeled as no. 2. In case of conductive SnO_2 layers, this caused a shunt between ITO strips no. 1 and no. 2, which is indicated by a red arrow (A). Furthermore, SnO_2 had grown underneath the mask and at the edges of the glass substrate, by a wrap-around effect that is inherent to ALD. This

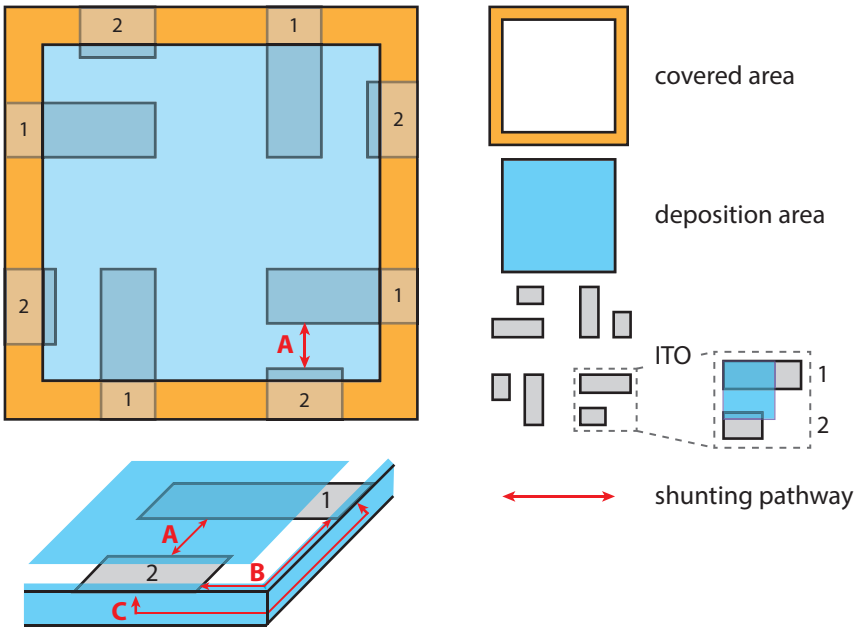

Figure D.2: *Realistic schematic of the former SnO_2 deposition area on a glass substrate with an ITO pattern. Below, a side-view of the substrate is provided. The red arrows indicate shunting pathways, due to wrap-around deposited conductive SnO_2.*

has been shown in the side-view below, and it caused other shunting paths between the ITO strips, as indicated by the other red arrows (B and C).

These practical issues have been resolved by interrupting the shunting pathways: (A) was interrupted by using an appropriate stainless steel mask on top, (B) by mechanically scratching the top, and (C) by mechanically cleaving the edges. Subsequently, the performances for PSCs with conductive SnO_2 layers have indeed improved largely, and the J-V measurement results have indicated no shunting problems anymore.

Appendix E

Additional Figures Optoelectronic Performance and Interface Characterizations of Perovskite Solar Cells

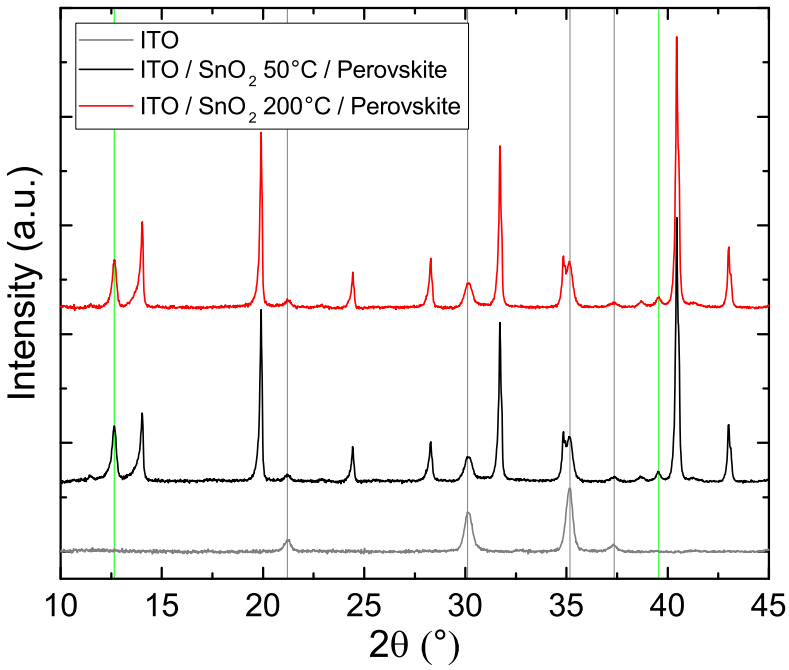

Figure E.1: *XRD spectra of perovskite layers deposited on 15 nm SnO_2 deposited either at 50°C or at 200°C, both on ITO substrates. The graph is extended with an XRD spectrum of solely an ITO substrate. Peaks originating from the ITO substrate are indicated with gray vertical lines. N.B.: the green vertical lines indicate measurement angles corresponding to crystallinity of PbI_2, which is, for example, present on top of the perovskite crystals (see also Figure E.3).*

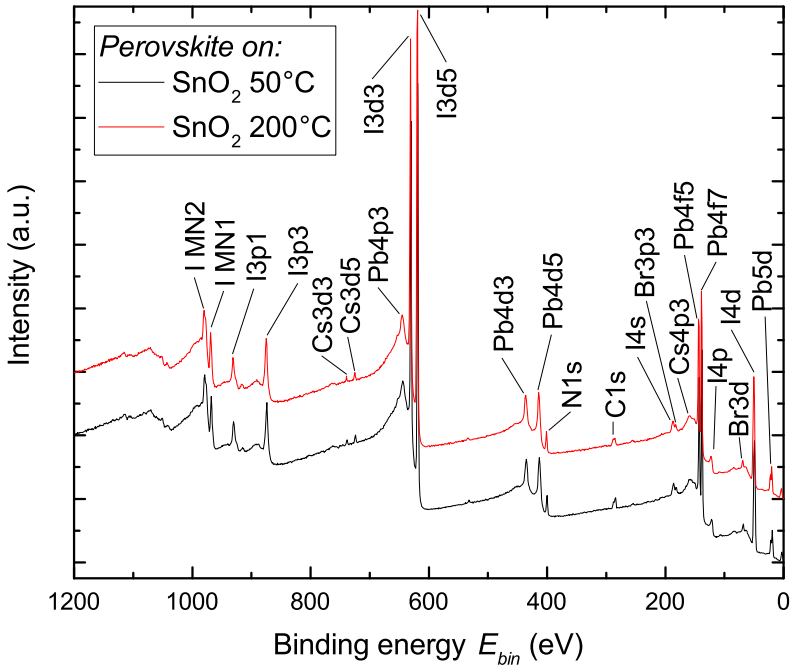

Figure E.2: *XPS surveys for perovskite layers deposited on 15 nm SnO_2 deposited either at 50°C or at 200°C. All constituents of the designed perovskite composition appear in the spectrum.*

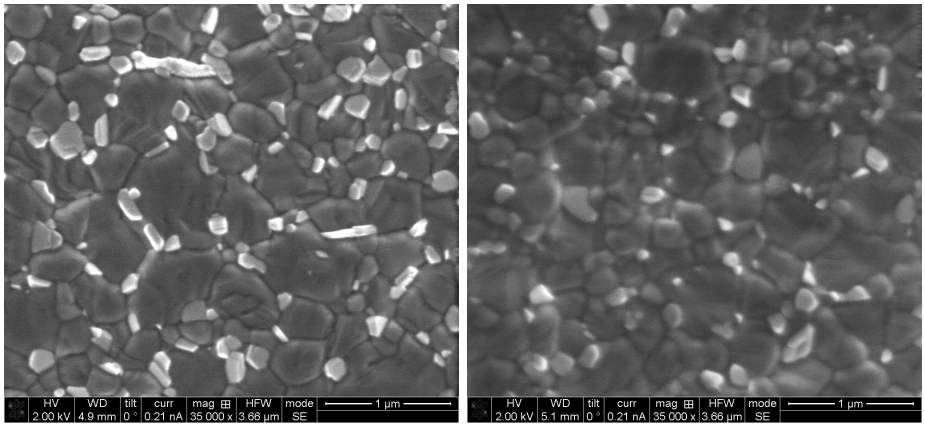

(a) *Perovskite on SnO_2 deposited at 50°C.*

(b) *Perovskite on SnO_2 deposited at 200°C.*

Figure E.3: *SEM top-view images of perovskite layers deposited on 15 nm SnO_2 deposited either at 50°C or at 200°C. As can be seen, both images contain perovskite grains of comparable sizes (dark gray). Furthermore, on both perovskite layers small crystals lie on top (light gray), which are PbI_2 grains from unreacted and/or excess PbI_2 precursor solution (according to [24]).*

References

[1] Di Giacomo, F., Zardetto, V., Lucarelli, G., Cinà, L., Di Carlo, A., Creatore, M., and Brown, T. *Nano Energy* **30**(October), 460–469 dec (2016).

[2] Jung, H. S. and Park, N.-G. *Small* **11**(1), 10–25 jan (2015).

[3] Yusoff, A. R. B. M. and Nazeeruddin, M. K. *The Journal of Physical Chemistry Letters* **7**(5), 851–866 mar (2016).

[4] Di Giacomo, F., Zardetto, V., D'Epifanio, A., Pescetelli, S., Matteocci, F., Razza, S., Di Carlo, A., Licoccia, S., Kessels, W. M. M., Creatore, M., and Brown, T. M. *Advanced Energy Materials* **5**(8), 1401808 apr (2015).

[5] Zardetto, V., Di Giacomo, F., Lucarelli, G., Kessels, W., Brown, T., and Creatore, M. *Solar Energy* **150**, 447–453 jul (2017).

[6] Kojima, A., Teshima, K., Shirai, Y., and Miyasaka, T. *Journal of the American Chemical Society* **131**(17), 6050–6051 may (2009).

[7] Yang, W. S., Park, B.-W., Jung, E. H., Jeon, N. J., Kim, Y. C., Lee, D. U., Shin, S. S., Seo, J., Kim, E. K., Noh, J. H., and Seok, S. I. *Science* **356**(6345), 1376–1379 jun (2017).

[8] National Renewable Energy Laboratory 2017. *NREL, "Best Research-Cell Efficiencies"* (date accessed: 26-06-2017), https://www.nrel.gov/pv/assets/images/efficiency–chart.png.

[9] Yang, G., Tao, H., Qin, P., Ke, W., and Fang, G. *J. Mater. Chem. A* **4**(11), 3970–3990 (2016).

[10] Grätzel, M. *Accounts of Chemical Research* **50**(3), 487–491 mar (2017).

[11] You, J., Meng, L., Song, T.-B., Guo, T.-F., Yang, Y. M., Chang, W.-H., Hong, Z., Chen, H., Zhou, H., Chen, Q., Liu, Y., De Marco, N., and Yang, Y. *Nature Nanotechnology* **11**(1), 75–81 oct (2015).

[12] Koushik, D., Verhees, W. J. H., Kuang, Y., Veenstra, S., Zhang, D., Verheijen, M. A., Creatore, M., and Schropp, R. E. I. *Energy Environ. Sci.* **10**(1), 91–100 (2017).

[13] Green, M. A., Ho-Baillie, A., and Snaith, H. J. *Nature Photonics* **8**(7), 506–514 jun (2014).

[14] Aitola, K., Domanski, K., Correa-Baena, J.-P., Sveinbjörnsson, K., Saliba, M., Abate, A., Grätzel, M., Kauppinen, E., Johansson, E. M. J., Tress, W., Hagfeldt, A., and Boschloo, G. *Advanced Materials* **29**(17), 1606398 may (2017).

[15] Zhao, J., Brinkmann, K. O., Hu, T., Pourdavoud, N., Becker, T., Gahlmann, T., Heiderhoff, R., Polywka, A., Görrn, P., Chen, Y., Cheng, B., and Riedl, T. *Advanced Energy Materials* **7**(14), 1602599 jul (2017).

[16] Li, B., Li, Y., Zheng, C., Gao, D., and Huang, W. *RSC Adv.* **6**(44), 38079–38091 (2016).

[17] Brittman, S., Adhyaksa, G. W. P., and Garnett, E. C. *MRS Communications* **5**(01), 7–26 mar (2015).

[18] Binek, A., Hanusch, F. C., Docampo, P., and Bein, T. *The Journal of Physical Chemistry Letters* **6**(7), 1249–1253 apr (2015).

[19] Saliba, M., Matsui, T., Seo, J.-Y., Domanski, K., Correa-Baena, J.-P., Nazeeruddin, M. K., Zakeeruddin, S. M., Tress, W., Abate, A., Hagfeldt, A., and Grätzel, M. *Energy Environ. Sci.* **9**(6), 1989–1997 (2016).

[20] Wang, D., Wright, M., Elumalai, N. K., and Uddin, A. *Solar Energy Materials and Solar Cells* **147**, 255–275 apr (2016).

[21] Zardetto, V., Williams, B. L., Perrotta, A., Di Giacomo, F., Verheijen, M. A., Andriessen, R., Kessels, W. M. M., and Creatore, M. *Sustainable Energy Fuels* **1**(1), 30–55 (2017).

[22] Correa Baena, J. P., Steier, L., Tress, W., Saliba, M., Neutzner, S., Matsui, T., Giordano, F., Jacobsson, T. J., Srimath Kandada, A. R., Zakeeruddin, S. M., Petrozza, A., Abate, A., Nazeeruddin, M. K., Grätzel, M., and Hagfeldt, A. *Energy Environ. Sci.* **8**(10), 2928–2934 (2015).

[23] Hu, T., Becker, T., Pourdavoud, N., Zhao, J., Brinkmann, K. O., Heiderhoff, R., Gahlmann, T., Huang, Z., Olthof, S., Meerholz, K., Többens, D., Cheng, B., Chen, Y., and Riedl, T. *Advanced Materials* **29**(27), 1606656 jul (2017).

[24] Wang, C., Zhao, D., Grice, C. R., Liao, W., Yu, Y., Cimaroli, A., Shrestha, N., Roland, P. J., Chen, J., Yu, Z., Liu, P., Cheng, N., Ellingson, R. J., Zhao, X., and Yan, Y. *J. Mater. Chem. A* **4**(31), 12080–12087 (2016).

[25] Wang, C., Xiao, C., Yu, Y., Zhao, D., Awni, R. A., Grice, C. R., Ghimire, K., Constantinou, I., Liao, W., Cimaroli, A. J., Liu, P., Chen, J., Podraza, N. J., Jiang, C.-S., Al-Jassim, M. M., Zhao, X., and Yan, Y. *Advanced Energy Materials* **7**(17), 1700414 sep (2017).

[26] George, S. M. *Chemical Reviews* **110**(1), 111–131 jan (2010).

[27] Profijt, H. B., Potts, S. E., van de Sanden, M. C. M., and Kessels, W. M. M. *Journal of Vacuum Science & Technology A: Vacuum, Surfaces, and Films* **29**(5), 050801 sep (2011).

[28] Knoops, H., Potts, S., Bol, A., and Kessels, W. In *Handbook of Crystal Growth*, 1101–1134. Elsevier (2015).

[29] Deng, K. and Li, L. *Advanced Materials Interfaces* **3**(21), 1600505 nov (2016).

[30] Poodt, P., Cameron, D. C., Dickey, E., George, S. M., Kuznetsov, V., Parsons, G. N., Roozeboom, F., Sundaram, G., and Vermeer, A. *Journal of Vacuum Science & Technology A: Vacuum, Surfaces, and Films* **30**(1), 010802 jan (2012).

[31] Kim, I. S. and Martinson, A. B. F. *J. Mater. Chem. A* **3**(40), 20092–20096 (2015).

[32] Schmidt, L. In *38th Rochester Mineralogical Symp. Program Notes*, 31–32, (2011).

[33] Snaith, H. J. *The Journal of Physical Chemistry Letters* **4**(21), 3623–3630 nov (2013).

[34] De Wolf, S., Holovsky, J., Moon, S.-J., Löper, P., Niesen, B., Ledinsky, M., Haug, F.-j., Yum, J.-h., and Ballif, C. *The Journal of Physical Chemistry Letters* **5**(6), 1035–1039 mar (2014).

[35] Kim, H.-S., Lee, C.-R., Im, J.-H., Lee, K.-B., Moehl, T., Marchioro, A., Moon, S.-J., Humphry-Baker, R., Yum, J.-H., Moser, J. E., Grätzel, M., and Park, N.-G. *Scientific Reports* **2**(1), 591 dec (2012).

[36] Snaith, H. J., Abate, A., Ball, J. M., Eperon, G. E., Leijtens, T., Noel, N. K., Stranks, S. D., Wang, J. T.-W., Wojciechowski, K., and Zhang, W. *The Journal of Physical Chemistry Letters* **5**(9), 1511–1515 may (2014).

[37] Leijtens, T., Eperon, G. E., Noel, N. K., Habisreutinger, S. N., Petrozza, A., and Snaith, H. J. *Advanced Energy Materials* **5**(20), 1500963 oct (2015).

[38] Meloni, S., Moehl, T., Tress, W., Franckevičius, M., Saliba, M., Lee, Y. H., Gao, P., Nazeeruddin, M. K., Zakeeruddin, S. M., Rothlisberger, U., and Graetzel, M. *Nature Communications* **7**(May 2015), 10334 feb (2016).

[39] Richardson, G., O'Kane, S. E. J., Niemann, R. G., Peltola, T. A., Foster, J. M., Cameron, P. J., and Walker, A. B. *Energy Environ. Sci.* **9**(4), 1476–1485 (2016).

[40] Jacobs, D. A., Wu, Y., Shen, H., Barugkin, C., Beck, F. J., White, T. P., Weber, K., and Catchpole, K. R. *Phys. Chem. Chem. Phys.* **19**(4), 3094–3103 (2017).

[41] Tress, W., Marinova, N., Moehl, T., Zakeeruddin, S. M., Nazeeruddin, M. K., and Grätzel, M. *Energy Environ. Sci.* **8**(3), 995–1004 (2015).

[42] Stranks, S. D., Eperon, G. E., Grancini, G., Menelaou, C., Alcocer, M. J. P., Leijtens, T., Herz, L. M., Petrozza, A., and Snaith, H. J. *Science* **342**(6156), 341–344 oct (2013).

[43] Shi, D., Adinolfi, V., Comin, R., Yuan, M., Alarousu, E., Buin, A., Chen, Y., Hoogland, S., Rothenberger, A., Katsiev, K., Losovyj, Y., Zhang, X., Dowben, P. A., Mohammed, O. F., Sargent, E. H., and Bakr, O. M. *Science* **347**(6221), 519–522 jan (2015).

[44] Kim, J. H., Liang, P.-W., Williams, S. T., Cho, N., Chueh, C.-C., Glaz, M. S., Ginger, D. S., and Jen, A. K.-Y. *Advanced Materials* **27**(4), 695–701 jan (2015).

[45] Yi, C., Luo, J., Meloni, S., Boziki, A., Ashari-Astani, N., Grätzel, C., Zakeeruddin, S. M., Röthlisberger, U., and Grätzel, M. *Energy Environ. Sci.* **9**(2), 656–662 (2016).

[46] Matsui, T., Seo, J.-Y., Saliba, M., Zakeeruddin, S. M., and Grätzel, M. *Advanced Materials* **29**(15), 1606258 apr (2017).

[47] Lee, J.-W., Kim, D.-H., Kim, H.-S., Seo, S.-W., Cho, S. M., and Park, N.-G. *Advanced Energy Materials* **5**(20), 1501310 oct (2015).

[48] Tan, H., Jain, A., Voznyy, O., Lan, X., García de Arquer, F. P., Fan, J. Z., Quintero-Bermudez, R., Yuan, M., Zhang, B., Zhao, Y., Fan, F., Li, P., Quan, L. N., Zhao, Y., Lu, Z.-H., Yang, Z., Hoogland, S., and Sargent, E. H. *Science* **355**(6326), 722–726 feb (2017).

[49] Barbé, J., Tietze, M. L., Neophytou, M., Murali, B., Alarousu, E., Labban, A. E., Abulikemu, M., Yue, W., Mohammed, O. F., McCulloch, I., Amassian, A., and Del Gobbo, S. *ACS Applied Materials & Interfaces* **9**(13), 11828–11836 apr (2017).

[50] Dong, Q., Shi, Y., Wang, K., Li, Y., Wang, S., Zhang, H., Xing, Y., Du, Y., Bai, X., and Ma, T. *The Journal of Physical Chemistry C* **119**(19), 10212–10217 may (2015).

[51] Murugadoss, G., Kanda, H., Tanaka, S., Nishino, H., Ito, S., Imahori, H., and Umeyama, T. *Journal of Power Sources* **307**, 891–897 mar (2016).

[52] Wu, W.-Q., Chen, D., Caruso, R. A., and Cheng, Y.-B. *J. Mater. Chem. A* **5**(21), 10092–10109 (2017).

[53] Leijtens, T., Eperon, G. E., Pathak, S., Abate, A., Lee, M. M., and Snaith, H. J. *Nature Communications* **4**, 1–8 (2013).

[54] Ke, W., Fang, G., Liu, Q., Xiong, L., Qin, P., Tao, H., Wang, J., Lei, H., Li, B., Wan, J., Yang, G., and Yan, Y. *Journal of the American Chemical Society* **137**(21), 6730–6733 jun (2015).

[55] Rao, H.-S., Chen, B.-X., Li, W.-G., Xu, Y.-F., Chen, H.-Y., Kuang, D.-B., and Su, C.-Y. *Advanced Functional Materials* **25**(46), 7200–7207 dec (2015).

[56] Song, J., Zheng, E., Bian, J., Wang, X.-F., Tian, W., Sanehira, Y., and Miyasaka, T. *J. Mater. Chem. A* **3**(20), 10837–10844 (2015).

[57] Abulikemu, M., Neophytou, M., Barbé, J. M., Tietze, M. L., El Labban, A., Anjum, D. H., Amassian, A., McCulloch, I., and Del Gobbo, S. *J. Mater. Chem. A* **5**(17), 7759–7763 (2017).

[58] Lee, M. M., Teuscher, J., Miyasaka, T., Murakami, T. N., and Snaith, H. J. *Science* **338**(6107), 643–647 nov (2012).

[59] Wu, Y., Yang, X., Chen, H., Zhang, K., Qin, C., Liu, J., Peng, W., Islam, A., Bi, E., Ye, F., Yin, M., Zhang, P., and Han, L. *Applied Physics Express* **7**(5), 052301 may (2014).

[60] Brinkmann, K., Zhao, J., Pourdavoud, N., Becker, T., Hu, T., Olthof, S., Meerholz, K., Hoffmann, L., Gahlmann, T., Heiderhoff, R., Oszajca, M. F., Luechinger, N. A., Rogalla, D., Chen, Y., Cheng, B., and Riedl, T. *Nature Communications* **8**, 13938 jan (2017).

[61] Kavan, L., Steier, L., and Grätzel, M. *The Journal of Physical Chemistry C* **121**(1), 342–350 jan (2017).

[62] Bush, K. A., Palmstrom, A. F., Yu, Z. J., Boccard, M., Cheacharoen, R., Mailoa, J. P., McMeekin, D. P., Hoye, R. L. Z., Bailie, C. D., Leijtens, T., Peters, I. M., Minichetti, M. C., Rolston, N., Prasanna, R., Sofia, S., Harwood, D., Ma, W., Moghadam, F., Snaith, H. J., Buonassisi, T., Holman, Z. C., Bent, S. F., and McGehee, M. D. *Nature Energy* **2**(4), 17009 feb (2017).

[63] Perrotta, A. *Looking down the rabbit hole: nano-porosity in thin films.* PhD thesis, Eindhoven University of Technology, (2016).

[64] Kitai, A. In *Principles of Solar Cells, LEDs and Diodes: The role of the PN junction*, 69–122. John Wiley & Sons, Ltd, Chichester, UK aug (2011).

[65] Gelderman, K., Lee, L., and Donne, S. W. *Journal of Chemical Education* **84**(4), 685 apr (2007).

[66] Paracchino, A., Mathews, N., Hisatomi, T., Stefik, M., Tilley, S. D., and Grätzel, M. *Energy & Environmental Science* **5**(9), 8673 (2012).

[67] Gamry Instruments. *Basics of Electrochemical Impedance Spectroscopy* (date accessed: 08-05-2017), https://www.gamry.com/application–notes/EIS/basics–of–electrochemical–impedance–spectroscopy.

[68] Bardini, L. *Second version of EIS 101, an introduction to electrochemical spectroscopy* (date accessed: 26-07-2017), http://dx.doi.org/10.13140/RG.2.1.2248.5600.

[69] Metikoš-Huković, M., Omanović, S., and Jukić, A. *Electrochimica Acta* **45**(6), 977–986 dec (1999).

[70] Perrotta, A., García, S. J., and Creatore, M. *Plasma Processes and Polymers* **12**(9), 968–979 sep (2015).

[71] Tarre, A., Rosental, A., Aidla, A., Aarik, J., Sundqvist, J., and Hårsta, A. *Vacuum* **67**(3-4), 571–575 sep (2002).

[72] Lu, J., Sundqvist, J., Ottosson, M., Tarre, A., Rosental, A., Aarik, J., and Hårsta, A. *Journal of Crystal Growth* **260**(1-2), 191–200 jan (2004).

[73] Sundqvist, J., Lu, J., Ottosson, M., and Hårsta, A. *Thin Solid Films* **514**(1-2), 63–68 aug (2006).

[74] Cheng, H.-E., Tian, D.-C., and Huang, K.-C. *Procedia Engineering* **36**, 510–515 (2012).

[75] Lee, D.-K., Wan, Z., Bae, J.-S., Lee, H.-B.-R., Ahn, J.-H., Kim, S.-D., Kim, J., and Kwon, S.-H. *Materials Letters* **166**, 163–166 mar (2016).

[76] Elam, J. W., Baker, D. a., Hryn, A. J., Martinson, A. B. F., Pellin, M. J., and Hupp, J. T. *Journal of Vacuum Science & Technology A: Vacuum, Surfaces, and Films* **26**(2), 244–252 mar (2008).

[77] Mullings, M. N., Hägglund, C., and Bent, S. F. *Journal of Vacuum Science & Technology A: Vacuum, Surfaces, and Films* **31**(6), 061503 nov (2013).

[78] Choi, D.-w. and Park, J.-S. *Surface and Coatings Technology* **259**(PB), 238–243 nov (2014).

[79] Choi, D.-w., Maeng, W., and Park, J.-S. *Applied Surface Science* **313**, 585–590 sep (2014).

[80] Sigma-Aldrich. *Tetrakis(dimethylamido)tin(IV) 99.9% trace metals basis* (date accessed: 20-10-2017), http://www.sigmaaldrich.com.

[81] Du, X., Du, Y., and George, S. M. *The Journal of Physical Chemistry A* **112**(39), 9211–9219 oct (2008).

[82] Potts, S. E., Profijt, H. B., Roelofs, R., and Kessels, W. M. M. *Chemical Vapor Deposition* **19**(4-6), 125–133 jun (2013).

[83] Aravindan, V., Jinesh, K., Prabhakar, R. R., Kale, V. S., and Madhavi, S. *Nano Energy* **2**(5), 720–725 sep (2013).

[84] Themlin, J.-M., Chtaïb, M., Henrard, L., Lambin, P., Darville, J., and Gilles, J.-M. *Physical Review B* **46**(4), 2460–2466 jul (1992).

[85] Szuber, J., Czempik, G., Larciprete, R., Koziej, D., and Adamowicz, B. *Thin Solid Films* **391**(2), 198–203 jul (2001).

[86] Thermo Scientific Xray Photoelectron Spectroscopy XPS. *Knowledge Base XPS Interpretation* (date accessed: 09-09-2017), http://xpssimplified.com.

[87] Moulder, J., Stickle, W., Sobol, P., and Bomben, K. *Handbook of X-ray Photoelectron Spectroscopy: A Reference Book of Standard Spectra for Identification and Interpretation of XPS Data*. Physical Electronics, Inc., Minnesota, (1995).

[88] Du, X., Du, Y., and George, S. M. *Journal of Vacuum Science & Technology A: Vacuum, Surfaces, and Films* **23**(4), 581–588 jul (2005).

[89] Batzill, M. and Diebold, U. *Progress in Surface Science* **79**(2-4), 47–154 (2005).

[90] FIZ Karlsruhe. *Inorganic Crystal Structures Database* (date accessed: 16-03-2017), https://icsd.fiz–karlsruhe.de.

[91] Khan, A. F., Mehmood, M., Aslam, M., and Ashraf, M. *Applied Surface Science* **256**(7), 2252–2258 jan (2010).

[92] Trost, S., Behrendt, A., Becker, T., Polywka, A., Görrn, P., and Riedl, T. *Advanced Energy Materials* **5**(17), 1500277 sep (2015).

[93] Lee, Y., Paek, S., Cho, K. T., Oveisi, E., Gao, P., Lee, S., Park, J.-S., Zhang, Y., Humphry-Baker, R., Asiri, A. M., and Nazeeruddin, M. K. *J. Mater. Chem. A* **5**(25), 12729–12734 (2017).

[94] Kiliç, Ç. and Zunger, A. *Physical Review Letters* **88**(9), 095501 feb (2002).

[95] Macco, B., Knoops, H. C. M., and Kessels, W. M. M. *ACS Applied Materials & Interfaces* **7**(30), 16723–16729 aug (2015).

[96] Jorcin, J.-B., Orazem, M. E., Pébère, N., and Tribollet, B. *Electrochimica Acta* **51**(8-9), 1473–1479 jan (2006).

[97] Perrotta, A., García, S. J., Michels, J. J., Andringa, A.-M., and Creatore, M. *ACS Applied Materials & Interfaces* **7**(29), 15968–15977 jul (2015).

[98] Zhang, J. and Desai, V. *Surface and Coatings Technology* **190**(1), 98–109 jan (2005).

[99] Shao, Y., Xiao, Z., Bi, C., Yuan, Y., and Huang, J. *Nature Communications* **5**, 5784 dec (2014).

[100] Emara, J., Schnier, T., Pourdavoud, N., Riedl, T., Meerholz, K., and Olthof, S. *Advanced Materials* **28**(3), 553–559 jan (2016).

[101] Choi, H., Jeong, J., Kim, H.-B., Kim, S., Walker, B., Kim, G.-H., and Kim, J. Y. *Nano Energy* **7**, 80–85 jul (2014).

[102] Ke, W., Zhao, D., Xiao, C., Wang, C., Cimaroli, A. J., Grice, C. R., Yang, M., Li, Z., Jiang, C.-S., Al-Jassim, M., Zhu, K., Kanatzidis, M. G., Fang, G., and Yan, Y. *J. Mater. Chem. A* **4**(37), 14276–14283 (2016).

[103] Liu, X., Tsai, K.-W., Zhu, Z., Sun, Y., Chueh, C.-C., and Jen, A. K.-Y. *Advanced Materials Interfaces* **3**(13), 1600122 jul (2016).

[104] Zhang, H., Cheng, J., Lin, F., He, H., Mao, J., Wong, K. S., Jen, A. K.-Y., and Choy, W. C. H. *ACS Nano* **10**(1), 1503–1511 jan (2016).

[105] Juarez-Perez, E. J., Wuβler, M., Fabregat-Santiago, F., Lakus-Wollny, K., Mankel, E., Mayer, T., Jaegermann, W., and Mora-Sero, I. *The Journal of Physical Chemistry Letters* **5**(4), 680–685 feb (2014).

[106] Ke, W., Zhao, D., Cimaroli, A. J., Grice, C. R., Qin, P., Liu, Q., Xiong, L., Yan, Y., and Fang, G. *J. Mater. Chem. A* **3**(47), 24163–24168 (2015).

[107] Xiong, L., Qin, M., Yang, G., Guo, Y., Lei, H., Liu, Q., Ke, W., Tao, H., Qin, P., Li, S., Yu, H., and Fang, G. *J. Mater. Chem. A* **4**(21), 8374–8383 (2016).

[108] Gonzalez-Pedro, V., Juarez-Perez, E. J., Arsyad, W.-s., Barea, E. M., Fabregat-Santiago, F., Mora-Sero, I., and Bisquert, J. *Nano Letters* **14**(2), 888–893 feb (2014).

[109] Correa-Baena, J.-P., Turren-Cruz, S.-H., Tress, W., Hagfeldt, A., Aranda, C., Shooshtari, L., Bisquert, J., and Guerrero, A. *ACS Energy Letters* **2**(3), 681–688 mar (2017).

[110] Kessels, W. and Knoops, H. In *ALD Basics; Plasma and other energy-enhanced ALD techniques* (, Eindhoven, 2017).

[111] Langereis, E. *Plasma-assisted atomic layer deposition: an in situ diagnostic study.* PhD thesis, Eindhoven University of Technology, (2008).

[112] Turrión, M., Bisquert, J., and Salvador, P. *The Journal of Physical Chemistry B* **107**(35), 9397–9403 sep (2003).

[113] Xu, J., Huang, S., and Wang, Z. *Solid State Communications* **149**(13-14), 527–531 apr (2009).

[114] Cameron, P. J. and Peter, L. M. *J. Phys. Chem. B* **107**(51), 14394–14400 (2003).

[115] Banyamin, Z., Kelly, P., West, G., and Boardman, J. *Coatings* **4**(4), 732–746 oct (2014).